Shrinking Core Model and Experimental Study of the Hydrolysis Reaction in the Cu-Cl Cycle for Hydrogen Production

by

Huda M. Radwan

A Thesis Submitted in Partial Fulfillment
of the Requirements for the Degree of Master of Engineering

in

The Faculty of Engineering and Applied Science Mechanical Engineering

Memorial University of Newfoundland and Labrador

May 2024

Newfoundland and Labrador

Abstract

Renewable and more environmentally friendly energy carriers, such as hydrogen, are increasingly crucial in achieving net-zero goals. Hydrogen, recognized as an efficient energy carrier, is gaining prominence. However, existing methods of hydrogen production from fossil fuels lead to carbon dioxide emissions. Consequently, emission free processes like water splitting are more environmentally sustainable.

The copper-chlorine (Cu-Cl) cycle has promising potential as a thermochemical process for producing hydrogen through water-splitting, especially when combined with solar and nuclear energy technologies. One of the challenging aspects of the cycle is the heterogeneous hydrolysis reaction, where it is essential to ensure high conversion of the reaction with minimal steam consumption. Therefore, understanding the reaction and mechanisms through experimental analysis and reaction modelling is crucial. This thesis aims to comprehensively investigate the kinetics of the hydrolysis reaction, taking into account various methods of pre-processing the solid reactant with different particle sizes.

As this is a cyclical process, the solid reactant of the hydrolysis reaction is the product of the preceding electrolysis step. Consequently, the process to retrieve the material from the previous step and prepare for hydrolysis should be examined, along with its impact on the material's particle size and reaction kinetics. Three processes were analyzed in this thesis: drying, crushing, and crystallisation. Initially, the particle size and morphology were examined through the utilization of scanning electron microscopy (SEM). Subsequently, the material was introduced into a vertical semi-batch fixed bed reactor, and the reaction conversion was monitored over the reaction time interval up to 30 minutes. The analysis was repeated for temperatures ranging from 350 - 400°C

and for different steam-to-copper ratios. Furthermore, the time conversion data were analyzed using a shrinking core model (SCM) to identify the predominant step and its associated coefficient.

The study revealed that the morphology of $CuCl_2$ tends to exhibit a stick-like shape, approximating a cylindrical form. When $CuCl_2$ is retrieved from a water solution using HCl as an anti-solvent, it can generate particles and flakes within a wide range of sizes, ranging from 65 to 1300 μm. However, approximately 75% of the crystallised reactant had a 230 μm average particle size, while the dried material particles were 95 μm and the crushed had 27 μm.

The hydrolysis reaction was investigated for dried, crushed, and three different particle sizes of crystallised materials. All samples revealed that the rate of conversion increases with an increase in temperature. The dried sample achieved the lowest rate of conversion, while the crushed sample achieved the highest rate of conversion. The crystallised materials achieved a rate of conversion higher than the dried material and lower than the crushed samples. When comparing the three different particle sizes of the crystallised material (crystallised 230 μm, crystallised 615 μm, and crystallised 1100 μm), the rate of conversion increased as the particle size decreased.

A model was developed for spherical and cylindrical particle shape assumptions, with four equations for each shape, and the models were compared with experimental data. Experiments showed that the reaction control model with a cylindrical shape assumption exhibited the best fit for dried and crystallised 615 μm and crystallised 1100 μm materials. The crushed material and crystallised 95 μm samples indicated that gas film diffusion controls the conversion. Dried and crystallised 95 μm material with a reduced S/Cu ratio showed that gas film diffusion was the controlling step.

X-ray diffraction (XRD) was utilised to analyze the solid product following the reaction, with the desired product Cu_2OCl_2 being identified for temperatures between 370 - 400°C. In contrast, the reaction at 350°C resulted in the side product of CuCl. The activation energy was 32 to 54

kJ/mol, varying for each particle size based on the linearization of the controlling step coefficient with temperature.

Furthermore, the research emphasized the alterations in surface area and porosity resulting from modifications in solid processing, as well as the impact of crystallised particle size distribution on the conversion. All experiments were conducted at a S/Cu ratio of 10, while two experiments were conducted at 390°C and a S/Cu ratio of 5, resulting in low conversion rates. Specifically, the dried material of 95 μm achieved only 36% conversion, while the crystallised material of 230 μm had 50% conversion within 30 minutes. Ensuring a high conversion rate, while minimizing the steam consumption, during the hydrolysis reaction are important for improving the overall efficiency of the Cu-Cl cycle and therefore the overall rate of hydrogen production.

Acknowledgements

I would like to express my heartfelt gratitude to my esteemed supervisors, Dr. K. Pope, Dr. G. Naterer, and Dr. K.A. Hawboldt, for their unwavering guidance, encouragement, and invaluable advice throughout the course of this research. Their expertise and mentorship have been instrumental in shaping the direction and success of this thesis.

I would also like to extend my appreciation to the Natural Sciences and Engineering Research Council of Canada (NSERC) and Canadian Nuclear Laboratories (CNL) for their generous financial assistance. Their support has been pivotal in enabling the realization of this research endeavour.

Furthermore, I would like to acknowledge the technical support and collaboration of my colleagues, Dilum Perera and Samita Rimal. Their contributions have been invaluable in advancing the progress of this research. I would also like to acknowledge Dr. M.J. Katz and Etienne Guinand for their work in conducting the surface area and porosity analyses.

Table of Contents

List of Tables

List of Figures

Nomenclature

b, c, d, e	stoichiometric coefficients
A, B, C, D	components of the reaction
Ä	pre-exponential factors
C_{Ag}	concentration of gaseous reactant in bulk gas, kmol/m^3
C_{As}	concentration of gaseous reactant at the particle surface, kmol/m^3
C_{Ac}	concentration of gaseous reactant at the reaction surface, kmol/m^3
D_e	effective diffusion coefficient, m^2/s
E	activation energy, kJ/mol
F	particle size fraction
H	height of the solid particle, m
k_g	mass transfer coefficient, m/s
k"	chemical reaction rate constant, m/s
Ṁ	mass flow rate, kg/s
M_w	molecular weight
N	number of moles
Ṅ	molar flow rate, mole/s
$p_{\text{sat } H_2O}$	partial pressure, Pa
R	radius of the solid particle, m
R"	universal gas constant, kJ/mol·K
RH_H	relative humidity
r_c	radius of unreacted solid core, m
S/Cu	molar ratio of steam to solid $CuCl_2$

t	conversion time of solid particles, min
T	temperature, ℃
V_{Trap}	trap volume, L
V	particle volume, μm^3
$\dot{V}$	volumetric flow rate, SLPM
X_B	conversion of solid
$\bar{X}_B$	average conversion of solid
Y1, Y2	dimensionless parameter
ρ	density, kg/m^3
ρ_B	molar density of the solid, $kmol/m^3$

Subscripts

g	gas film diffusion
c	chemical reaction
d	product layer diffusion
H	humidifier
sp	spherical
cy	cylindrical

Chapter 1 Introduction

1.1 Background

Alternative and cleaner energy sources, including hydrogen, have become increasingly crucial for achieving net-zero carbon emission goals. Hydrogen is a promising clean energy carrier, however, hydrogen produced by fossil fuels typically produces carbon. Therefore, emission-free hydrogen production processes, such as water splitting, are considered more environmentally friendly depending on the process used to split the water [1].

Hydrogen is advantageous as an energy carrier because it can produce electricity through fuel cells or thermal energy through combustion, and it has the potential to be coupled with other chemicals for energy storage. The worldwide demand for hydrogen has been steadily increasing, reaching approximately 95 million tons in 2022 [2]. However, most hydrogen production currently relies on carbon-based fuels, with only a small portion produced from renewable sources. In order to fully harness the potential of hydrogen as a clean fuel, several challenges must be addressed. These challenges include the development of more environmentally friendly, cost-effective, and efficient production methods, such as electrochemical and thermochemical processes.

One potentially viable thermochemical cycle is the copper-chlorine (Cu-Cl) cycle, which functions at a comparatively lower temperature than other thermochemical cycles. This cycle has the capability to be combined with solar and nuclear energy sources, thereby enhancing its viability as an environmentally friendly and sustainable approach for hydrogen generation. The selection of design and unit operations for scaling up hydrogen production using the Cu-Cl cycle necessitates particular evaluation of individual capacities and energy demands [3, 4].

The Cu-Cl cycle is typically a four-step process: electrochemical reaction, drying, hydrolysis reaction, and thermolysis reaction. This work focuses on the hydrolysis reaction, where the copper

chloride is reacted with steam to form Cu_2OCl_2 and HCl as per Equation (1-1). The reaction occurs between 375ºC and 400ºC and is usually operated with excess steam. The steam-to-copper ratio is defined as the fraction of moles of steam to solid $CuCl_2$ and was reported to affect the reaction conversion significantly [1].

$$2CuCl_{2(s)} + H_2O_{(g)} \rightarrow Cu_2OCl_{2(s)} + 2HCl_{(g)} \quad (1\text{-}1)$$

Hydrolysis is a gas-solid reaction that can be modelled using uniform conversion (VM) or shrinking core models (SCM). The SCM limits the reaction zone to a thin layer that advances from the particle's outer surface, where gaseous reactant diffuses through a film surrounding the particle, then penetrates and diffuses through an ash layer to the unreacted core [5]. In the SCM, particle morphology and size are significant parameters. They can affect the overall reaction rate by shifting the rate-controlling step [5].

The Cu-Cl thermochemical cycle presents a promising approach for the generation of hydrogen. The spray drying step involves evaporating water with a drying medium. But this requires high heat transfer loads [6]. To overcome this, the steam can be utilised through heat recovery from the hydrolysis reactor. This method has the potential to improve energy efficiency. Crystallisation is another method for integrating hydrolysis into the cycle. Crystallisation allows for separating $CuCl_2$ from a saturated solution without additional equipment. It offers several advantages over spray drying in terms of energy requirements and engineering viability. One of the advantages is that crystallisation does not require heat extraction or drying air processing [7].

This thesis investigates different pre-processing techniques for solid $CuCl_2$ and studies the hydrolysis reaction experimentally under various operating conditions to understand the reaction kinetics better. Integrating experimental data and morphology analysis will enhance the accuracy of the reaction coefficients accordingly, enhancing the prediction of the SCM and leading to more

accurate predictions of the hydrolysis reaction kinetics. Ultimately, this research aims to develop more efficient and reliable models for hydrogen production using the Cu-Cl cycle.

1.2 Scope and Objectives

The heterogeneous hydrolysis reaction must maintain a high level of conversion in the reaction while minimizing steam consumption. It is important to understand the reaction rate and mechanisms through experimental analysis and reaction modelling. Creating a precise model for forecasting reaction kinetics holds significant importance. Additionally, the incorporation of the hydrolysis reaction into the cycle necessitates various approaches to the pre-processing of solid reactants. The impact of these procedures on the size of the solid reactant particles and their influence on the kinetics of the reaction and assumptions in modelling must be taken into account.

The aims of this research can be briefly outlined as follows.

1. Investigate different pre-processing techniques for solid $CuCl_2$, such as drying, crushing, and crystallisation. Examine the resultant distribution of particle sizes and their morphology structure through the utilization of scanning electron microscopy (SEM).
2. Study the hydrolysis reaction using a vertical semi-batch fixed bed reactor under different operating parameters, such as temperature and steam-to-copper ratio. This investigation should encompass different particle sizes obtained from the various pre-processing methods of $CuCl_2$. Generate time conversion data to gain insights into the reaction progress. Additionally, analyze the solid product using X-ray diffraction (XRD) to gain insight into any side products formed during the reaction.
3. Utilize the experimental data and morphology obtained in the previous steps to enhance the SCM. This enhancement should involve determining the gas film diffusion coefficient, diffusion through the product layer coefficient, and the reaction constant. The controlling

step should also be identified, and each particle size's activation energy should be determined.

By accomplishing these objectives, a deeper understanding of the hydrolysis reaction and its kinetics can be achieved. This research will contribute to developing more efficient and accurate models for predicting the reaction kinetics, ultimately advancing the field of hydrogen production.

1.3 Thesis Structure

This thesis comprises of six chapters. Chapter 2 provides a literature review on the Cu-Cl cycle, hydrolysis reaction, $CuCl_2$ crystallisation, and the SCM. Chapter 3 describes the methodology and experimental design, including the crystallisation process, particle size and morphology analysis, and the vertical semi-batch setup. The experimental conditions are also discussed. Chapter 4 includes deriving the shrinking core model (SCM) for gas film diffusion, gas diffusion through the product layer, and reaction control steps, considering both spherical and cylindrical particle shapes. An algorithm is developed to determine diffusion and reaction coefficients, and a final equation is presented to account for particle size distribution and its impact on the model. The following chapter provides an analysis of the results and further discussion, commencing with the examination of scanning electron microscopic data and particle size distribution. Subsequently, the conversion and shrinking core models are employed for each experiment to determine the governing step and associated coefficients. A thorough comparison among the experiments is undertaken to assess the impact of particle size and operational variables on the reaction and to investigate the activation energy, surface area, and porosity. Chapter 5 highlights the study's main findings, and appendices are attached, which include information on experimental errors and measurement uncertainties, in addition to the repeatability tests and time factor analysis.

1.4 Co-Authorship Statement

Huda M. Radwan is the thesis author and is responsible for the experimentation, modelling, and data analysis. The supervisors of this thesis, Dr. Greg F. Naterer, Dr. Kevin Pope and Dr. Kelly A. Hawboldt provided concept formulation, supervision, technical advice, analytical support, discussed the methods and results at all stages of the research, and assisted with editing of the thesis.

Chapter 2 Literature Survey

This chapter reviews thermochemical water-splitting cycles, primarily focusing on the Cu-Cl cycle. It provides a detailed account of previous studies on the hydrolysis reaction, highlighting the main challenges and key findings. Additionally, it discusses previous research on $CuCl_2$ crystallisation and selected advancements in implementing the shrinking core model. The chapter also explores the previous work in applying the SCM to the hydrolysis reaction.

2.1 Cu-Cl Cycle

Different thermochemical water splitting cycles were investigated previously, such as Magnesium Iodine that operates at 600 °C [8], Sulfur Iodine [9], Vanadium Chlorine [10], Cerium Chlorine [11], Iron Chlorine [12], and Hybrid Sulfur [13], which all occur at temperatures between 700 - 900°C. Prior research has examined a range of thermochemical methods for generating hydrogen from water, taking into account parameters such as thermal efficiency, simplicity, feasibility, and costs. Additionally, the effectiveness of hydrogen production utilizing nuclear power or solar energy as heat sources has been investigated [14, 15]. Because of the substantial energy demand of the preceding cycles, the Cu-Cl cycle, which operates around 550°C [16], is a promising cycle with relatively high overall conversion, low maintenance and material costs, and availability of chemicals, making it potentially suitable for integration with renewable or waste energy [17, 18].

The cycle can be linked with a variety of heat sources, such as solar energy and reactors [19, 20]. This adaptability allows for the use of different energy sources for hydrogen production. By integrating with these heat sources, the Cu-Cl cycle can optimize the utilization of high-temperature heat and further improve energy efficiency. The Cu-Cl cycle can be designed using established processes in industry, making it easier to implement and scale up for large-scale hydrogen

production. This compatibility with existing processes reduces barriers to adoption and accelerates the deployment of the cycle [21].

Waste heat can be effectively harnessed in the cycle to enhance energy efficiency and decrease costs. There are several approaches to utilizing waste heat in the Cu-Cl cycle. One approach involves transferring waste heat through a pipeline from a power plant's moderator vessel, where the waste heat is generated, to a nearby thermochemical hydrogen plant [22, 23]. The waste heat, often at a temperature of approximately 75°C, can be transferred via a fluid and then utilised as a drying medium in a spray dryer to produce $CuCl_{2(s)}$ in the Cu-Cl cycle. This direct utilization of waste heat improves the energy efficiency of the cycle.

Another method involves further upgrading the waste heat using heat pumps [24, 25]. Chemical heat pumps can release heat in exothermic reactors at higher temperatures. Vapour compression heat pumps, such as a CuCl vapour compression heat pump, can also be employed to upgrade the waste heat. These heat pumps can achieve high coefficients of performance, thereby enhancing the efficiency of the cycle.

Additionally, heat losses from a high-temperature heat source, such as a Generation IV nuclear reactor like the super-critical water reactor, can heat water or steam in the hydrogen production loop [26]. Heat exchangers can be utilised for this purpose [27, 28]. This integration enables the co-generation of electricity and hydrogen, maximizing the utilization of the high-temperature heat from the nuclear power plant.

The Cu-Cl cycle offers a promising solution for hydrogen production due to its compatibility with various potential heat sources. Utilizing waste heat in the cycle can enhance energy efficiency and reduce costs. Direct utilization, heat pump upgrading, and integration with high-temperature sources can improve overall efficiency. The Cu-Cl cycle is becoming a viable option for hydrogen production as demand for clean hydrogen rises.

The Cu-Cl cycle includes a sequence of chemical reactions such as hydrolysis and physical processes such as drying, which eventually transform water into oxygen and hydrogen. These reactions occur through the use of intermediate copper chloride compounds. Previous studies have presented different cycle variations depending on the number of reactions involved. Many factors should be considered when comparing different cycles, such as the reaction kinetics and yield, energy consumption, and solids processing within the cycle [29].

Past studies presented different cycle steps. Ferrandon et al. [30] studied the cycle as electrolysis, hydrolysis, and decomposition steps, while Farsi et al. [31] identified four reaction steps and presented a two-step demonstration [16]. Daggupati et al. [32] studied a 5-step cycle. Two main perspectives were used to compare these cycles: the first combined the cycle's exergy, energy, and yield effectiveness [29], and the second compared the cycles through a life cycle assessment. The 4-step cycle offers advantages in terms of reaction kinetics and reduced complexity while also minimizing environmental impacts [29, 33, 34]. Converting the $CuCl_2$ from aqueous to solid is encountered in both the 4-step and 5-step cycles. This can be accomplished using different unit operations. Equations from (2-1) to (2-4) present the steps of the cycle.

1. Electrochemical step (hydrogen production) at 25°C:

$$2CuCl_{(aq)} + 2HCl_{(aq)} \rightarrow 2CuCl_{2(aq)} + H_{2(g)} \quad (2\text{-}1)$$

2. Drying step at approximately 150°C:

$$2CuCl_{2(aq)} \rightarrow 2CuCl_{2(s)} \quad (2\text{-}2)$$

3. Hydrolysis step at 400°C:

$$2CuCl_{2(s)} + H_2O_{(g)} \rightarrow Cu_2OCl_{2(s)} + 2HCl_{(g)} \quad (2\text{-}3)$$

4. Decomposition step at 550°C:

$$Cu_2OCl_{2(s)} \rightarrow 2CuCl_{(l)} + {}^{1}/_{2}\, O_{2(g)} \quad (2\text{-}4)$$

The hydrolysis step faces challenges that must be overcome to improve solid conversion while reducing overall steam requirements [1]. Additionally, there is a need to decrease the capital cost of the process and minimize energy consumption in the solid drying process of aqueous $CuCl_2$. Another challenge is separating the HCl / steam product, which requires an energy-intensive azeotropic distillation process [35]. Furthermore, handling solids between processes and working with corrosive fluids presents unique challenges regarding material selection, corrosion resistance, and system design [10].

To address these challenges, ongoing research is underway to create materials that are resistant to corrosion for the working fluids and to resolve the challenges related to managing solids. These efforts aim to enhance the efficiency and cost-effectiveness of the hydrolysis step, ultimately improving the system's overall performance [36 - 39].

Integrating the hydrolysis step has challenges of side reactions and the formation of undesired by-products. These by-products, such as Cl_2 gas and the decomposition of desired solid products, hinder the efficiency of the process and the overall yield. Previous investigations have identified several potential side reactions within the hydrolysis reactor and have provided data on the decomposition of $CuCl_2$.

Earlier studies have identified significant side reactions in the hydrolysis stage. One notable side reaction involves the decomposition of $CuCl_2$ and Cu_2OCl_2. Experimental work has reported this side reaction occurs at around 400°C [40, 41]. Alternatively, some researchers have recommended using an inert gas in conjunction with the steam feed to mitigate the formation of side products [40]. Other side reactions, such as the reduction and vaporization of copper compounds, have also been documented [43, 44]. Equations from (2-5) to (2-9) illustrate the side reactions associated with the hydrolysis reaction.

$$CuCl_2 \rightarrow CuCl + Cl_2 \quad (2\text{-}5)$$

$$Cu_2OCl_2 \rightarrow CuO + CuCl_2 \quad (2\text{-}6)$$

$$CuO + Cl_2 \rightarrow CuCl_2 + 0.5O_2 \quad (2\text{-}7)$$

$$Cl_{2(s)} + H_2O_{(g)} \rightarrow 2HCl_{(g)} + 0.5O_{2(g)} \quad (2\text{-}8)$$

$$CuCl_2 + CuCl_{(s)} \rightarrow CuCl_2/CuCl_{(l)} \quad (2\text{-}9)$$

Hydrolysis has been studied for various reactors, such as fluidized beds, packed beds, and spray and falling particle reactors, operating as batch or semi-batch. Studies on semi-batch fixed beds are the earliest models. The conceptual process design and sensitivity studies provided a method to identify the most critical operating parameters. The commercial copper chloride dihydrate $CuCl_2 \cdot 2H_2O$ was dried and crushed using a ball mill and then sieved into three sizes: a) 250 - 300 μm, b) 150 - 250 μm, and c) Ball milled (undetermined smaller size) [43]. These results were based on the side product (CuCl) formation. In general, smaller particle sizes and higher steam-to-copper ratios achieve better conversion and reduce the by-product (CuCl) due to mass transfer enhancement [43].

A thermogravimetric analyzer (TGA) was used to study the reaction. The TGA operates as a small-scale semi-batch fixed bed reactor. The impact of temperature, particle size, and reaction time on the conversion and side reaction was studied [35]. The particle size was reduced using a ball mill from 46 - 47 nm to study three size ranges: a) 25 - 27 nm, b) 20 - 22 nm, and c) 15 - 17 nm. The particles were reported to have a flat surface with sharp corners forming cuboid particles for the 46 - 47 nm commercial $CuCl_2 \cdot 2H_2O$. In contrast, the ball-milled particle morphology was described as regular-shaped cubes. Particles of size 20 - 22 nm achieved the best results, with a yield of approximately 95% compared to a 55% yield for 46 - 47 nm particles [35].

In the fluidized bed reactor study, the particle had a mean average size of 265 μm. Operating parameters were optimized, and particle conversions were achieved using excess steam [44]. The

physical reaction resistances during the initial 30 min reduced the reaction rate by 40% and was attributed to increased film diffusion resistance [44]. In a study by Thomas et al. (2020) [40], the impact of temperature, reaction time, and steam mole fraction on reaction rate was studied [40]. The reactant $CuCl_2$, with an average particle size of 350 μm, was mixed with glass beads in a fluidized bed reactor. Operating conditions that achieved the best conversion were 300 - 325°C with a 0.5 steam mole fraction and a residence time of 20 - 40 min [40].

Spray reactors have been studied where $CuCl_2$ is in the form of a slurry and atomized and sprayed into steam [30]. Maintaining uniform temperature, optimum operating pressure, and controlling the droplet resident time are critical aspects for efficient contact and reaction [30]. The $CuCl_2$ water droplets (25 mm) were introduced to the reactor by an ultrasonic nozzle or pneumatic nebulizer. The ultrasonic nozzle achieved a higher product yield in counter-current flow than the nebulizer. A 95% yield was achieved using a 24 steam-to-copper molar ratio [30]. This impacts the feasibility of using this type of reactor in the process since a high conversion with less ratio was achieved in other studies, which requires further investigation and optimization to become feasible.

Daggupati et al. [45] used VM and SCM to study $CuCl_2$ hydrolysis in reactive spray drying (a combination of drying and hydrolysis). This reaction involves drying and reaction stages in one process. The electrolysis step produces an aqueous solution, which is then dispersed into liquid droplets using a hot medium, leading to immediate drying and a reaction. The model encompasses gaseous film diffusion, penetration of reactants through a product layer, and gaseous diffusion of the product back to the exterior [45]. The analysis showed that a reduction of particle size reduces diffusion resistance. By varying the excess steam pressure and adding an inert gas at 375ºC, a complete conversion of $CuCl_2$ can be achieved. A proper reactor type was proposed based on the controlling step and conversion with time data as per Table 2-1 [45].

Table 2-1: Reactor Selection Based on Daggupati et al. [45] Model

Particle Size	<40 µm	200 µm
Total Conversion Time (Reaction Controlling)	22 s	60 s
Total Conversion Time (Diffusion Controlling)	10 min	10 min
Proper Reactor Type	Reactive Spray Drying	Fluidized Bed

Similar modelling was conducted for a free-falling reactor. Where an average particle size of 200 µm falls freely from the reactor top to interact with the reflux steam, natural convection draws steam from the cold side of the reactor, allowing sufficient residence time for the reactant [31]. A model was developed in another study to predict the hydrodynamic behaviour and conversion of $CuCl_2$ particles and steam using the VM and SCM [46]. The effect of superficial velocity and bed inventory (mass of $CuCl_2$) on conversion was presented. The solid particle conversion increased with superficial velocity and a higher bed inventory [46]. $CuCl_2$ particles are produced as an aqueous solution in the electrolysis step of the cycle. Table 2-2 presents the primary conversion and yield for various reactor types and operational parameters.

Table 2-2: Past Literature Conversion Summary

Reactor Type	Temperature Range °C	Particle Size (μm)	Reaction Time (min)	Reactant Processing	Conversion or Yield
Semi Batch Fixed-Bed	360 - 400	0.015-0.047	15 - 120	Dried and ball-milled	Yield: 48 - 97% $gCu_2OCl_2/gCuCl_2$ [35]
	300- 375	350	10 - 180	Mixed with glass beads	Yield: 60 -76% $gCu_2OCl_2/gCuCl_2$ [40]
Spry Reactor	400	6 - 23	2	Crystallisation, spray drying and ball milled	Yield ($gCu_2OCl_2/gCuCl_2$) at 0.5 bar: 75% @ 10:1 ratio 40% @ 5:1 ratio [37]
	300 - 450	150 - 250	20 - 60		Conversion: 0.96% [47] Yield: 3 – 12% $gCuCl/gCuCl_2$

2.2 Crystallisation

Crystallisation is the precipitation of the $CuCl_2$ from the saturated solution by cooling. The decrease in temperature reduces the solubility of the $CuCl_2$ particles, which initiates the crystallisation process [50, 51]. Crystallisation offers several advantages as a method for recovering solids from solution. Firstly, it is a low-energy process that requires minimal material and resources, making it cost-effective. It is a relatively simple technique that can be easily implemented. Crystallisation also allows for the extraction of solids with high purity, as the crystals formed are typically free from impurities. However, there are also some disadvantages to crystallisation. One drawback is the remaining residual in the solution, which can lead to waste or additional processing steps. The amount of crystallised material can also vary with the solution's initial concentration. The cooling rate can affect the yield and size of the crystals formed, requiring careful control and optimisation. Despite these limitations, crystallisation remains a preferred method in the Cu-Cl cycle to process the $CuCl_2$ before introducing it into the hydrolysis reactor [6, 50, 52, 53]. It is preferable when comparing crystallisation to other processes that recover solids from solutions, such as spray drying. Crystallisation is a more energy-efficient and cost-effective method, as spray drying involves the evaporation of the solvent from a solution using an anti-solvent such as hydrogen chloride (HCl) which is energy-intensive [1, 54]. In contrast, crystallisation takes advantage of the solubility change in the solvent as it cools, forming crystals [6].

A recent study focused on the crystallisation of $CuCl_2$ using HCl as an anti-solvent. The study added an HCl concentration of (3 - 9 M) to the saturated $CuCl_2$/Water mixture and employed analytical techniques such as X-ray diffraction (XRD) and thermogravimetric analysis (TGA) to analyse the composition and properties of the recovered solids. TGA provided information about the thermochemical properties of the solids. The melting temperature was found to be 462°C, and

the vaporization was 600°C. These techniques provided insight into the nature and characteristics of the crystals [7].

By understanding the challenges and solutions associated with this process, the optimisation of the cycle can be improved to increase the efficiency of hydrogen production. Based on the previous studies, further investigation is necessary to fully comprehend the impact of particle size and morphology of the crystallised particles on the hydrolysis reaction rate and extent.

2.3 Shrinking Core Model (SCM)

Fluid-particle reactions are essential in various industrial processes, such as combustion, gasification, and catalysis. It is crucial to understand the underlying reaction mechanisms to optimize the efficiency and performance of these processes. The shrinking core model (SCM), presented by Levenspiel [5], is widely used for describing fluid-particle reactions. This model provides valuable insight into the reaction dynamics and the formation of different types of products [5]. According to the model, the reaction occurs solely on the particle's surface. As the reaction progresses, the unreacted core of the particle shrinks and moves towards the centre. The model describes five sequential steps in the reaction process, each presenting a resistance to the conversion of the solid.

Figure 2-1 shows a concise overview of these stages. The first step is diffusion of the gaseous reactant through the film surrounding the particle. This film acts as a barrier, and the diffusion rate determines reactant availability for the subsequent steps. Once the gaseous reactant diffuses through the film, it penetrates and diffuses through the product layer. The reaction between the fluid and the solid particle forms the product layer. This step is crucial as it determines the rate at which the reactant reaches the reaction surface [5].

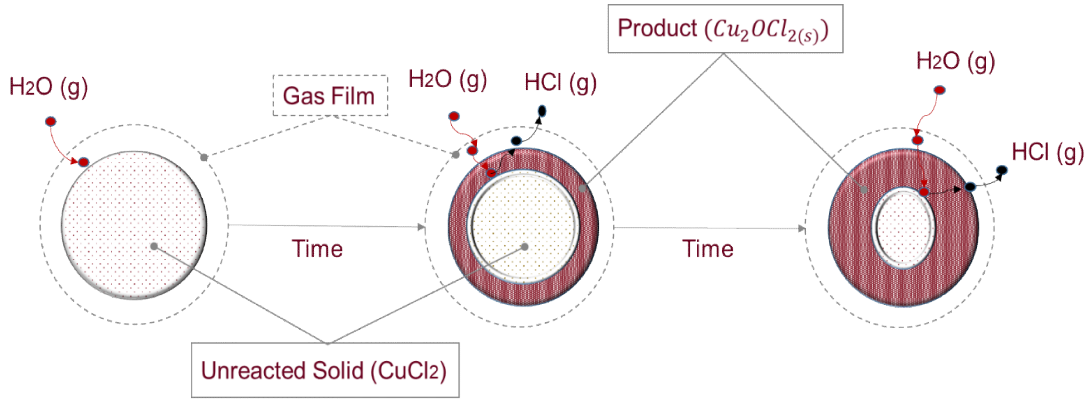

Figure 2-1: Shrinking core model steps

The third step involves the reaction of the gaseous reactant with the solid at the reaction surface. This reaction leads to the formation of new substances and the conversion of the solid material. After the reaction, the gaseous products need to diffuse through the product layer, and the gas film to return to the bulk gas [5]. Fluid-particle reactions can result in the formation of different types of products. These include fluid products that remain in the fluid phase and solid products with unique properties. In some instances, both fluid and solid products are formed. The type of product depends on factors such as the nature of the reactants, reaction conditions, and the specific reaction being considered [5].

While the SCM provides valuable insight into fluid-particle reactions, it has certain limitations. Firstly, it assumes that the reaction occurs along a sharp interface between the product layer and the unreacted solid, whereas in reality, the reaction may be more diffuse. In this case, it can be expressed using the shrinking core and continuous reaction models. Secondly, the high heat release rate can affect the model's accuracy for fast reactions and needs to be considered in practical applications. The shrinking core model may not accurately represent gas-solid systems with slow reactions and very porous solids due to the diverse pore structure commonly found in porous solids. This structural diversity affects the transport of reactants within the solid phase and the availability of reactive sites, challenging the assumptions of the shrinking core model. Gas-solid reactions with

slow kinetics may involve complex reaction pathways, such as multiple intermediate steps or side reactions. The shrinking core model simplifies the reaction mechanism, overlooking potential complexities in the actual reaction sequence, resulting in discrepancies between model predictions and experimental outcomes. In such cases, the continuous reaction model may be more appropriate, which considers the reaction to occur throughout the entire particle. Lastly, the SCM does not apply to situations where solid conversion occurs solely due to heat flow, without contact with the gas. These cases require different models to describe the reaction dynamics more accurately [5, 40].

The SCM is based on several assumptions that simplify the fluid-particle reactions. These assumptions include the reaction taking place at the particle's outer surface and progressing inward, shrinkage of the unreacted core during the reaction, the stationary nature of the product layer formed by the reaction, and the constant particle size throughout the reaction [5, 40]. By considering the sequential steps of the reaction process and the resistance presented by each step, this model provides insight into the dynamics of the reaction. However, it is essential to be aware of the limitations and assumptions of the model to ensure its accurate application in practical scenarios [5, 55].

One of the primary and early applications of the SCM is the combustion of carbonaceous materials [5]. This model describes the fluid-solid reaction in various fields and applications, such as the combustion of pure carbon particles. Other potential uses include the non-catalytic liquid-solid heterogeneous reaction between acid and minerals [55], the redox reaction of the oxygen carrier (OC) particles during chemical looping (CL) processes [57, 58], the dissolution of Ukpor clay in nitric acid solution [58], the conversion of gibbsite to alumina [59], the fluorination of uranium dioxide [60], the formation kinetics of carbon dioxide (CO2) and methane (CH_4) hydrates [60], the hydration kinetics of aluminium-particle-water reaction [62], the diffusion limit of the

aqueous system Cu-$Fe^{(0)}$/NO_3^-[63], and the investigation of the dissolution in concentrated alkaline solutions [64].

The model proposed by Levenspiel [5] has several simplifying assumptions. More comprehensive models with different assumptions can be found in the literature. Shen and Smith [54] presented a model for the combined resistance of gas diffusion, solid diffusion, and reaction for spherical particles under both isothermal and non-isothermal conditions, expressed in terms of dimensionless parameters for equilibrium reaction. Additionally, Liu et al. [56] developed another model for SCM, accounting for non-linear and non-isothermal effects. Homma et al. [60] investigated a heterogeneous reaction model representing gas-solid reactions with two-step reactions, considering the formation and consumption of a solid intermediate and accounting for the shrinkage of the unreacted core and the solid particle. Li et al. [55] examined a model for shrinking particle clusters with fractal surface properties.

Haseli et al. [65] conducted an investigation into the transport phenomena related to the reaction in a fluidized bed. The study used both VM and the SCM models. In a similar study, Farsi et al. [31] employed the SCM to forecast the film diffusion and the product layer diffusion for a free falling particle reactor operating based on the natural convection process. The SCM results indicated that the reaction is product layer diffusion and reaction control for $CuCl_2$ particles of 200 μm.

The hydrolysis reaction is primarily influenced by chemical reaction and diffusion through the product layer. Decreasing the particle size can mitigate the diffusion resistance. Daggupati et al. [45] conducted an assessment and performed parametric optimization related to the S/Cu ratio, flow rate, reaction duration, temperature, and particle size for fixed bed hydrolysis. The models were utilised to propose a potential pathway for the diffusion-controlled hydrolysis of $CuCl_2$ and to determine the kinetic parameters, including the rate constant and activation energy.

Table 2-3 presents an overview of primary data from previous studies on coefficients, reaction rates, and activation energies. These data encompass a variety of reactor types and operational parameters, offering valuable insights into the hydrolysis reaction. Variations in controlling steps reported in different studies may be attributed to differences in particle size, reactor design, operating conditions affecting contact time and efficiency between gas and particle surfaces, and assumptions used to develop models in each study. Notably, the shape factor and material morphology were not considered in the SCM. Therefore, generating reaction coefficients from experimental data covering a wide range of data is necessary to achieve accurate predictions using the model.

This study will utilize experimental data and SCM to gain a deeper understanding of reaction kinetics and controlling steps, encompassing various operational parameters and raw material processing, including crystallised raw materials.

Table 2-3: Past Literature Reported Coefficients and Activation Energy for Hydrolysis Reaction

Reference	Coefficient / Activation Energy	Conditions
Ferrandon et al. [47]	Mass transfer coefficient = 8.33 x10^{-5} (m/s) Effective diffusion coefficient = 2.03 x10^{-9} (m^2/s) Rate constant = 0.00011 (m/s)	150 - 250 µm 365 - 400ºC
Daggupati et al. [66]	Rate constant = 2.2 (mmol/m^2.s) The rate constant for first-rate reaction = 0.1 (mmol/s)	150 - 250 µm 375ºC
Thomas et al. [40]	Effective diffusion coefficient = 4.6 × 10^{-9} (m^2/s) Frequency factor = 2.4 × 104 (h−1) Activation Energy = 44.8 (kJ/mol)	300 - 375ºC
Pope et al. [67] Lewis et al. [43] Singh et al. [35]	Activation Energy = 41 (kJ/mol) Activation Energy = 42 (kJ/mol) Activation Energy = 106 - 93 (kJ/mol)	265 µm, 375ºC 350°C 0.015 - 0.047 µm, 360 - 400 ºC

Chapter 3 Experimental Procedure

This chapter presents an overview of the experimental design and mathematical modelling of the hydrolysis reaction. The initial section outlines the crystallisation process and particle size and morphology analysis. The subsequent section offers a comprehensive explanation of the vertical semi-batch setup, operation, and the associated analysis procedure. The chapter also presents a discussion of the selection of experimental conditions.

3.1 Morphology and Agglomeration

The particle size and morphology of the material are significant factors in the shrinking core model (SCM), as the particle size might affect the conversion, reaction rate, and controlling step. The particle size of $CuCl_2$ can be modified using manual crushing using a pestle and mortar, ball milling, crystallisation, or spray drying. This study used manual crushing and crystallisation. Pestle and mortar were used to crush $CuCl_2 \cdot 2H_2O$. Another sample was dried at 90 - 110°C and then crushed.

As for crystallisation, $CuCl_2 \cdot 2H_2O$ particles were dissolved in distilled water to form a saturated solution, and then HCl with an assay of 36.5% - 38.0% was added to create a solution with a molarity concentration of 6 molars. The solution flask was heated on a hotplate until it reached 60°C. A sample of 10 mL was taken immediately after adding the HCl and dried in the oven at 110°C for further analysis. The solution was cooled at room temperature. The final step was the solution filtration to separate the crystals. A sample of 10 mL of the final solution was also stored for analysis. A sieve analysis was performed by meshing the sample through three stainless steel meshes of 1000, 400, and 74 μm. The average particle size allowed through mesh 1000 and 400 was 914 and 381 μm, respectively. For mesh 74, the wave style is plain Dutch, where the

average particle size allowed through the mesh is 40 μm, and the largest particle size allowed is 58 - 63 μm.

The dry sieve analysis technique is essential for establishing the distribution of particle sizes within a given material. It involves calculating the total mass of the sample by calculating the mass retained on each sieve. The cumulative mass retained is the sum retained on a specific sieve and all the sieves above it. To calculate the mass passing through each sieve, subtract the mass retained on that sieve from the mass retained on the previous sieve. The cumulative mass passing through is the sum of the mass passing through a particular sieve and all the sieves above it. To determine the percentage passing and retained on each sieve, divide the mass passing or retained on a particular sieve by the total mass of the sample and multiply by 100. This calculation provides valuable insights into the distribution of particle sizes in the sample [68].

A particle size distribution curve is used to visually represent the distribution of particle sizes. The y-axis of the graph denotes the percentage of particles that pass through a sieve, while the x-axis represents the size of the sieve. This curve provides a graphical depiction of the distribution of particle sizes. The coefficient of uniformity (C_f) is employed to characterize the particle size distribution, indicating the uniformity or heterogeneity of the material. A higher C_f value suggests a broader range of particle sizes, while a lower C_f value indicates a more uniform size distribution. Here, C_f is calculated by dividing D60 over D10, where D60 refers to the particle size at which 60% of the material is finer and 40%, while D10 represents the particle size at which 10% of the material is finer in the particle size distribution analysis. Meanwhile, the coefficient of cumulative (Cc) is a measure of the fine particle content in a material. It represents the cumulative percentage of particles smaller than a specific size. Then Cc is calculated by Equation (3-1) [69].

$$\mathrm{Cc} = \frac{(D30)^2}{D60 \times D10} \tag{3-1}$$

This parameter offers valuable information regarding the distribution of particle sizes and signifies the percentage of small particles present in the substance. The coefficient of uniformity (C_f) and coefficient of cumulative (Cc) are interconnected parameters that offer a comprehensive understanding of the particle size distribution in a material. The C_f and Cc values provide information about the range and distribution of particle sizes [67 - 70]. The process of evaluating the outcomes of the sieve analysis involves the examination of the curve representing the distribution of particle sizes, which aids in understanding the characteristics. Given the potential impact of particle size on reaction rates and kinetics, it is crucial to identify the predominant particle sizes following crystallisation. Furthermore, the sieving process was employed as a separation method to obtain samples of varying sizes.

The SEM, which produces images of a sample by scanning the surface with a focused beam of electrons, provided information about the morphology of the samples after different processes. It also indicated an estimation of the particle size that can be achieved. Using the same test for the same sample, the energy-dispersive X-ray spectroscopy evolving from the interaction of electrons with the sample produced characteristic X-ray information for the elements in the sample. This information was used as a comparative analysis to ensure the processes (Crushing, drying and crystallisation) did not change the material elements.

Moreover, the surface area and porosity were assessed utilizing a micropolitics TriStar II Plus instrument. The BET (brunauer-emmett-teller) surface area and the BJH (barrett-joyner-halenda) adsorption average pore width were determined. The BET and BJH are interconnected physical properties that pertain to the surface characteristics and pore structure of materials, albeit their relationship with particle size is more indirect. The BET surface area quantifies the total surface area available for adsorption and reaction per unit mass of material. It is determined by the specific

surface area of the material, representing the surface accessible to the surrounding environment. Higher surface areas typically indicate more active sites for reactions or adsorption processes.

On the other hand, the BJH is a parameter that represents the average size of the pores within the material obtained from the desorption branch of an adsorption isotherm. It signifies the pore size distribution within the material. A smaller average pore width suggests finer or smaller pores within the material structure. The relationship between BET and BJH can offer insights into a material's porosity and surface characteristics. Materials with larger surface areas may possess a complex network of smaller pores, leading to a higher pore volume and, in some cases, smaller average pore widths. However, this relationship is not universally applicable, as various materials can have different pore structures that do not always conform to this pattern.

Regarding particle size, there is no direct correlation between BET or BJH and particle size. Particle size refers to the physical dimensions of individual particles, whereas surface area and pore width are properties related to the material's internal structure. However, smaller particles may sometimes exhibit higher surface areas due to their increased surface-to-volume ratio [69, 70].

3.2 Vertical Semi-Batch Setup

The experimental setup in Figure 3-1, Figure 3-2 and Figure 3-3 comprises essential components such as a nitrogen source, humidifier, heaters, reactor, trap, and fume extraction unit. The nitrogen gas cylinder has a single-stage regulator to monitor cylinder pressure and inline mass flow controllers for precise flow control. The flow is directed to the humidifier through a 1/2-inch pipeline, with pressure and temperature monitored using a pressure transmitter and J-type thermocouple, respectively. A pressure safety valve and check valve are installed in line before the humidifier to prevent backflow. A three-way valve creates a bypass system, allowing gas flow within the setup without passing through the humidifier. This bypass system is utilised for system heating before the start of the reaction, aiding in reaching a steady-state condition and reducing the

humidity to zero within the system. It is also used to perform a leak test before each experiment. When the desired reactor temperature is reached, steam flow is introduced by redirecting the nitrogen gas flow from the bypass toward the humidifier pipes.

The humidifier consists of pipes immersed in a water bath heated to 80°C, with the pipes half-filled with deionized water to facilitate the formation of water vapour. As the nitrogen flows through the pipes, it carries water vapour. The mixture of water vapour and nitrogen is then directed to a 400°C preheater throughout pipes covered by a heat tape with an adjustable thermostat to increase the flow temperature and prevent condensation. The temperature and humidity of the flow after the heat tape and before the preheater are monitored using an omega HX200 humidity transmitter.

The next step involves the preheater, which utilizes full-cylinder ceramic radiant heaters surrounding the pipeline, controlled by a PID controller linked to a k-type thermocouple placed between the heater's inner surface and the pipe's outer surface. The controller sends a signal to a solid-state relay connected to the heater. A pressure relief and check valve are employed after the preheater for safety and to prevent backflow. All preceding steps prepare the steam/nitrogen flow before entering the reactor.

The reactor depicted in Figure 3-4 is constructed from a 1-inch diameter and 16-inch length 316 stainless steel pipe. Positioned midway along the pipe is a double plain Dutch weave 50/250 mesh of Hastelloy C-276, which retains solid particles. Surrounding the pipe is a full cylinder of ceramic radiant heaters. The design incorporates 1-inch vestibules at both ends to minimize heat loss from the heater. The temperature within the reactor is monitored using inline K-type thermocouples, positioned 10 cm away from the mesh and immersed in the reactor flow using protection tube with a closed end. The thermocouple located at the top side of the reactor is connected to a PID controller, which sends a signal to a solid-state relay connected to the heater.

The effluent leaving the reactor is a combination of steam, nitrogen, and HCl, directed to a trap consisting of a cylindrical column of water and sodium hydroxide mixture. In this trap, the HCl reacts with sodium hydroxide to form sodium chloride. Finally, a fume absorber unit, comprising a dust pre-filter M5, HEPA H13 filter, and active carbon filter, is positioned above the trap for safety precautions.

During the reaction, a 2-milliliter sample is extracted from the trap every minute, with 500 microliters being utilised for analysis using a pipette with a relative bios of 0.004. This sample is then subjected to chloride concentration analysis using a chloride analyzer with a ± 3 mg/l accuracy [72]. The analyzer employs coulometric titration as a quantitative method, wherein a constant current is applied between electrodes to the reagent, producing silver ions and resulting in a change in the solution's conductivity, which is detected by a sensing electrode [73]. The concentration of chloride obtained from the analysis is equivalent to hydrochloric acid. Consequently, the moles of hydrochloric acid ($\dot{N}_{HCl,out}$) can be determined using Equation (3-2) in which the mass flow rate of hydrochloric acid is denoted as $\dot{M}_{Hcl}$ and the trap volume is denoted as$\mathrm{V_{Trap}}$. The molecular weight can be represented as Mw. This correlation can be established with the stoichiometry outlined in Equation (4-1) to calculate the moles of reacted solid. This information can subsequently be utilized to determine the conversion rate.

$$\dot{N}_{HCl,out} = \frac{\left(\dot{M}_{Hcl}\right)\left(\mathrm{V_{Trap}}\right)}{\mathrm{Mw}} \tag{3-2}$$

Another experimental parameter must also be established, the gas reactant's molar concentration. This involves calculating the fraction of steam in the nitrogen flow by measuring the temperature ($\mathrm{T_H}$) and relative humidity (RH_H) after the humidifier. The molar flow rate of nitrogen ($\dot{N}_{N_2}$) is then calculated using Equation (3-3), and the steam molar flow rate ($\dot{N}_{H_2O,in}$) is determined using Equation (3-4), where the density of nitrogen is denoted as ρ_{N_2} and the density

of steam and ρ_{H_2O}, while molar flow rate of nitrogen is represented as $\dot{M}_{N_2}$, and molar flow rate of steam is represented as $\dot{M}_{H_2O}$ and $\dot{V}_{N_2}$ is the nitrogen volumetric flow rate.

$$\dot{N}_{N_2} = \frac{\rho_{N_2} \times \dot{V}_{N_2}}{\dot{M}_{N_2}} \tag{3-3}$$

$$\dot{N}_{H_2O,in} = \frac{\rho_{H_2O} \times \dot{V}_{N_2}}{\dot{M}_{H_2O}} \tag{3-4}$$

The density of steam can be determined through the application of Equation (3-5), while the partial pressure can be computed using Equation (3-6), as indicated by Ref. [74].

$$\rho_{H_2O} = 0.0022 \times \frac{\frac{p_{\text{sat }H_2O}}{100} \times RH_H}{\mathrm{T_H}} \tag{3-5}$$

$$p_{\text{sat }H_2O} = \frac{\exp\left(77.345 + 0.0057 \times (\mathrm{T_H}) - \frac{7235}{\mathrm{T_H}}\right)}{\mathrm{T_H^{8.2}}} \tag{3-6}$$

3.3 Experimental Parameter Selection

The heterogeneous hydrolysis reaction of the Cu-Cl cycle presents a significant challenge. In order to optimize steam consumption and conversion rate, it is essential to understand the reaction rate and mechanism well. This necessitates experimental studies, reaction modelling, and consideration of solid reactant pre-processing methods. This thesis will investigate pre-processing techniques, analyze particle size distribution and morphology, study the hydrolysis reaction under different parameters, generate conversion data, analyze the solid product, use the shrinking model prediction, and determine the controlling step and activation energy. The operational parameters and sample processing methods were selected based on these objectives.

Crystallisation has been identified as a promising method for processing the reactant $CuCl_2$ before introducing it into the hydrolysis reactor. This process was chosen to investigate its impact on the reaction progress and kinetics and was compared with the drying process. Additionally, the

selection of different particle sizes was made to assess their influence on reaction yield and kinetics and determine the controlling step of the shrinking core model. To achieve a variety of particle sizes, the dried material was crushed, and different portions of the crystallised material were separated during sieving. Experimental parameters and sample selection were based on the particle size variety obtained from the scanning electron microscope (SEM) analysis, as illustrated in Figure 3-5.

Furthermore, to obtain sufficient data on the reaction coefficients as a function of temperature, the reaction should be conducted at least at three different temperatures. Based on previous studies in the literature, the temperature range that maximizes conversion and minimizes side products is reported to lie between 370°C and 400°C [35, 37, 47, 65]. Some studies have also reported reactions between 300°C and 400°C [40, 43, 47]. Consequently, the experiment was initially conducted between 350°C and 390°C. After obtaining preliminary results where the product was not detected at 350°C, the subsequent experiments were conducted at 370°C, 390°C, and 400°C for each selected particle size to obtain a comprehensive dataset.

The steam-to-copper ratio is a critical factor for this reaction as it impacts steam consumption and the cost of the process. A ratio of 10 was selected to ensure high conversion for most of the experiments. Subsequently, a ratio of 5 was chosen to compare two experiments. While the time factor was not directly investigated within the scope of this research, a few preliminary experiments were conducted at different time intervals to assist in selecting the reaction duration for the experiments. A fixed duration of 30 minutes was established for all the experiments for accurate comparisons, except for the smallest particle size, which achieved the highest conversion in approximately 15 - 16 minutes. Consequently, the experiments investigating the time factor were only analyzed for conversion results and briefly included in the appendices.

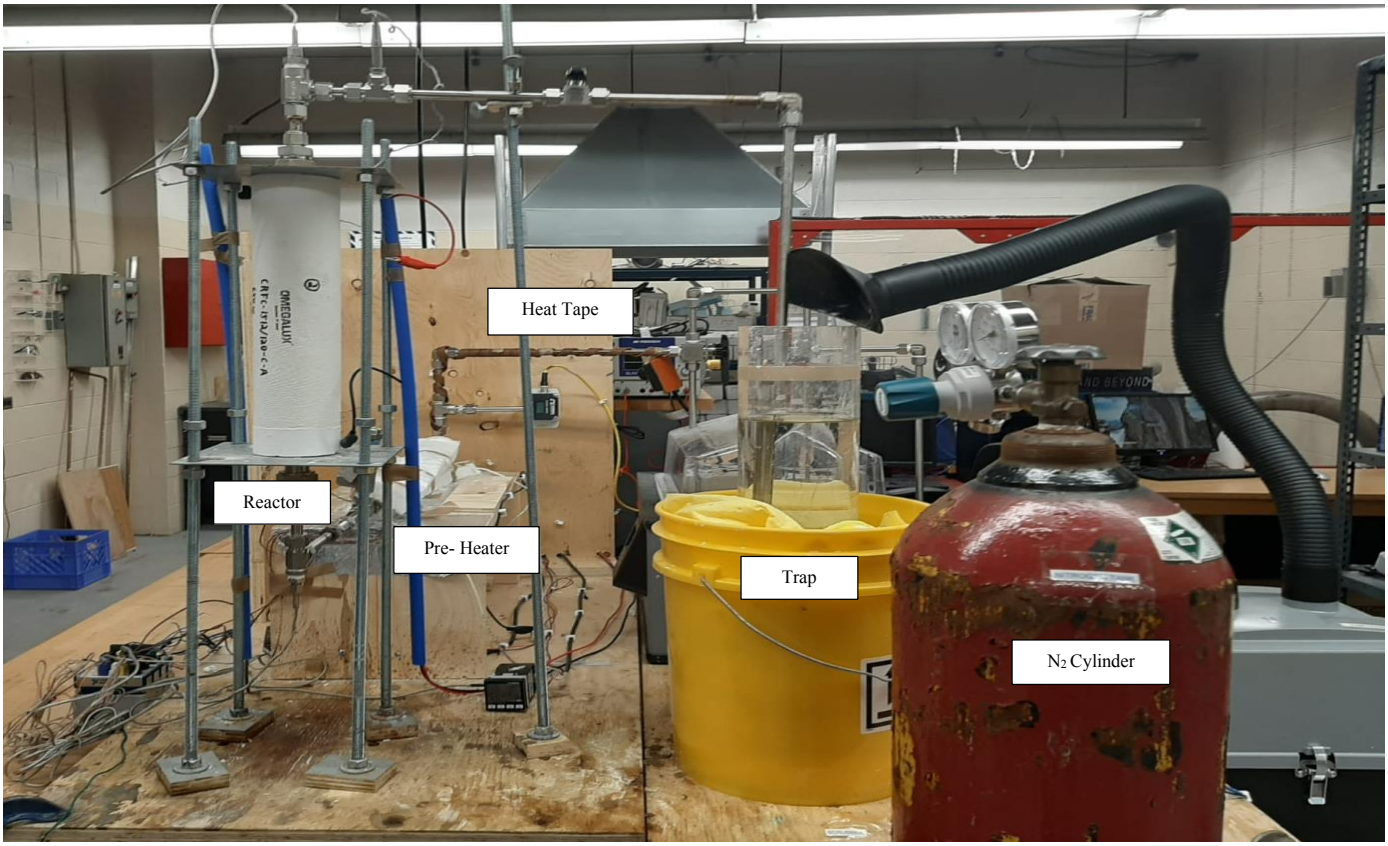

Figure 3-1: Experiment setup, front view

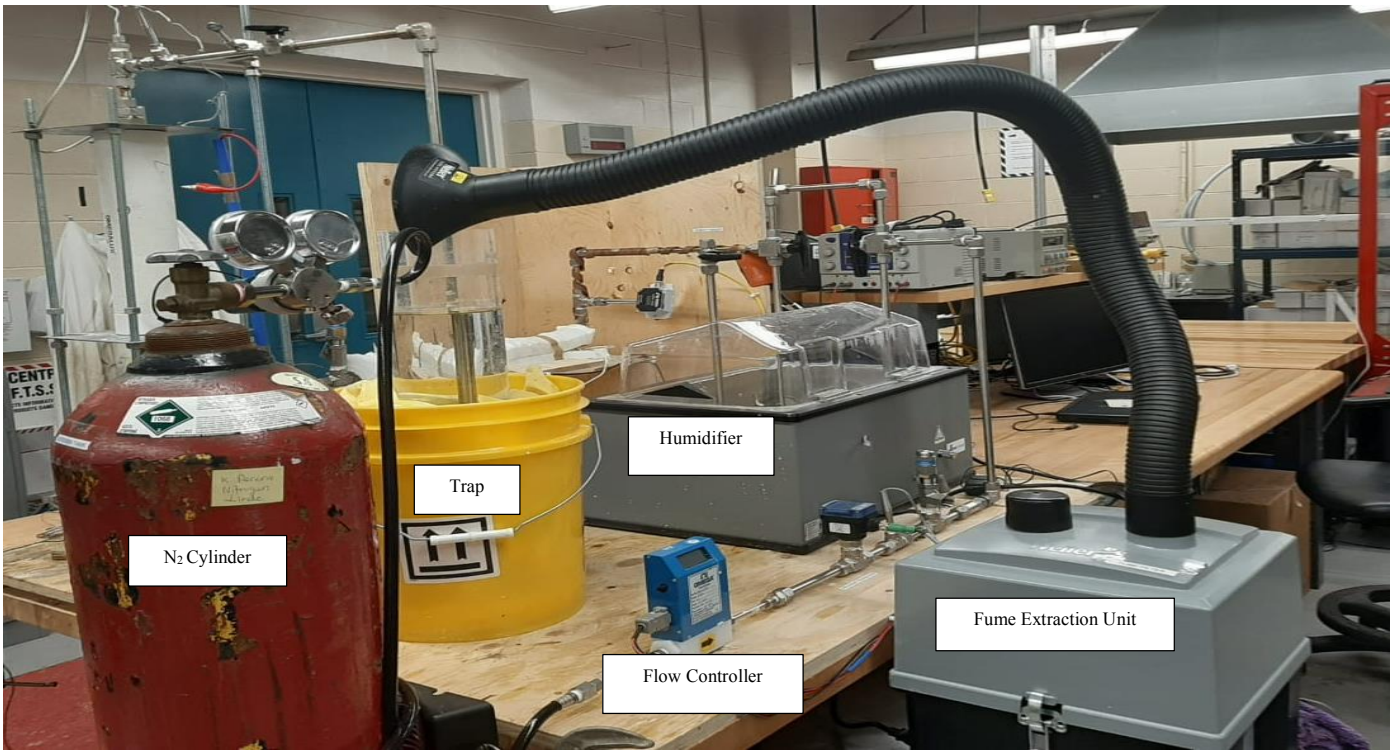

Figure 3-2: Experiment setup, side view

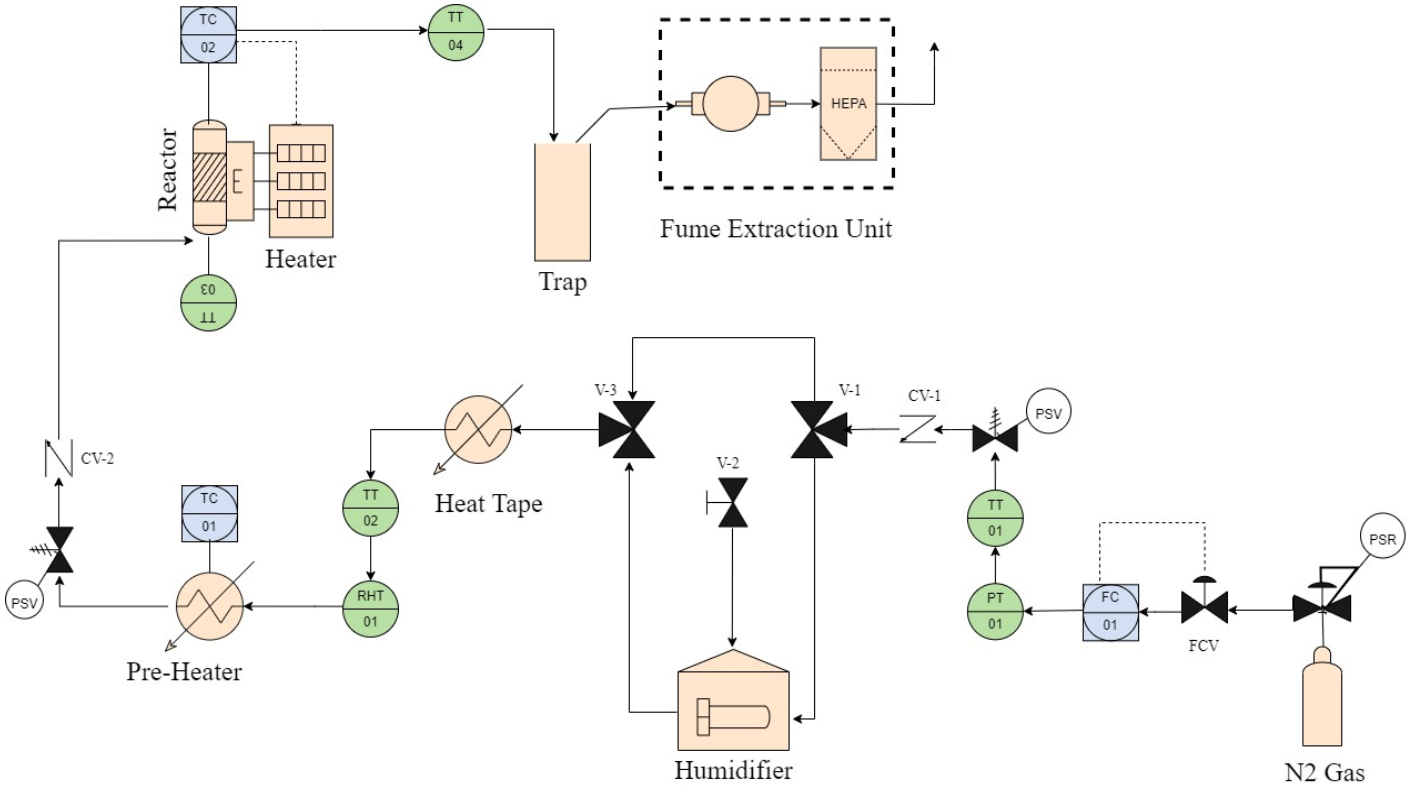

Figure 3-3: Experimental piping and instrumentation diagram

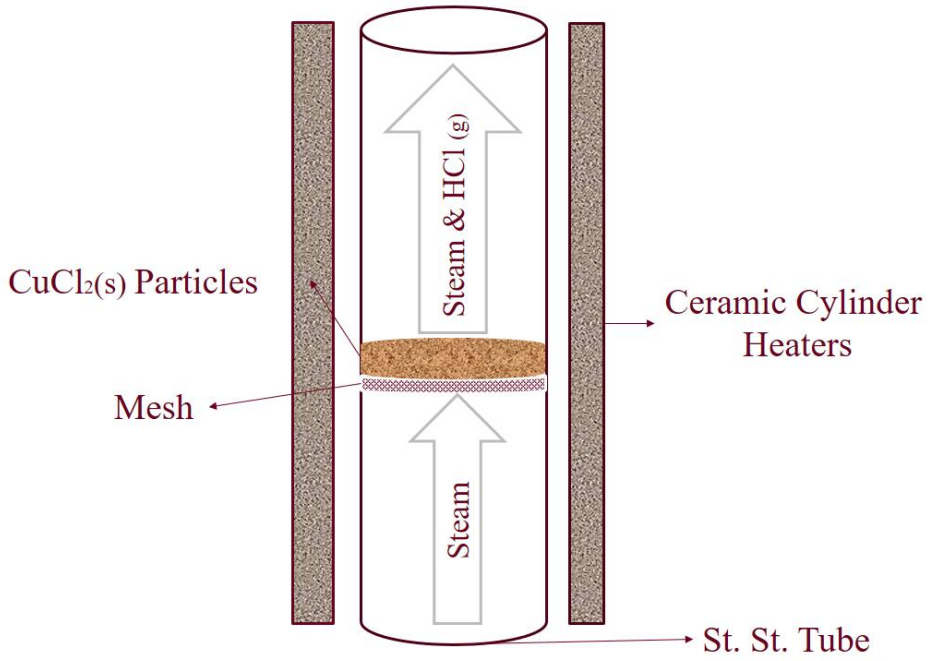

Figure 3-4: Vertical semi-batch reactor

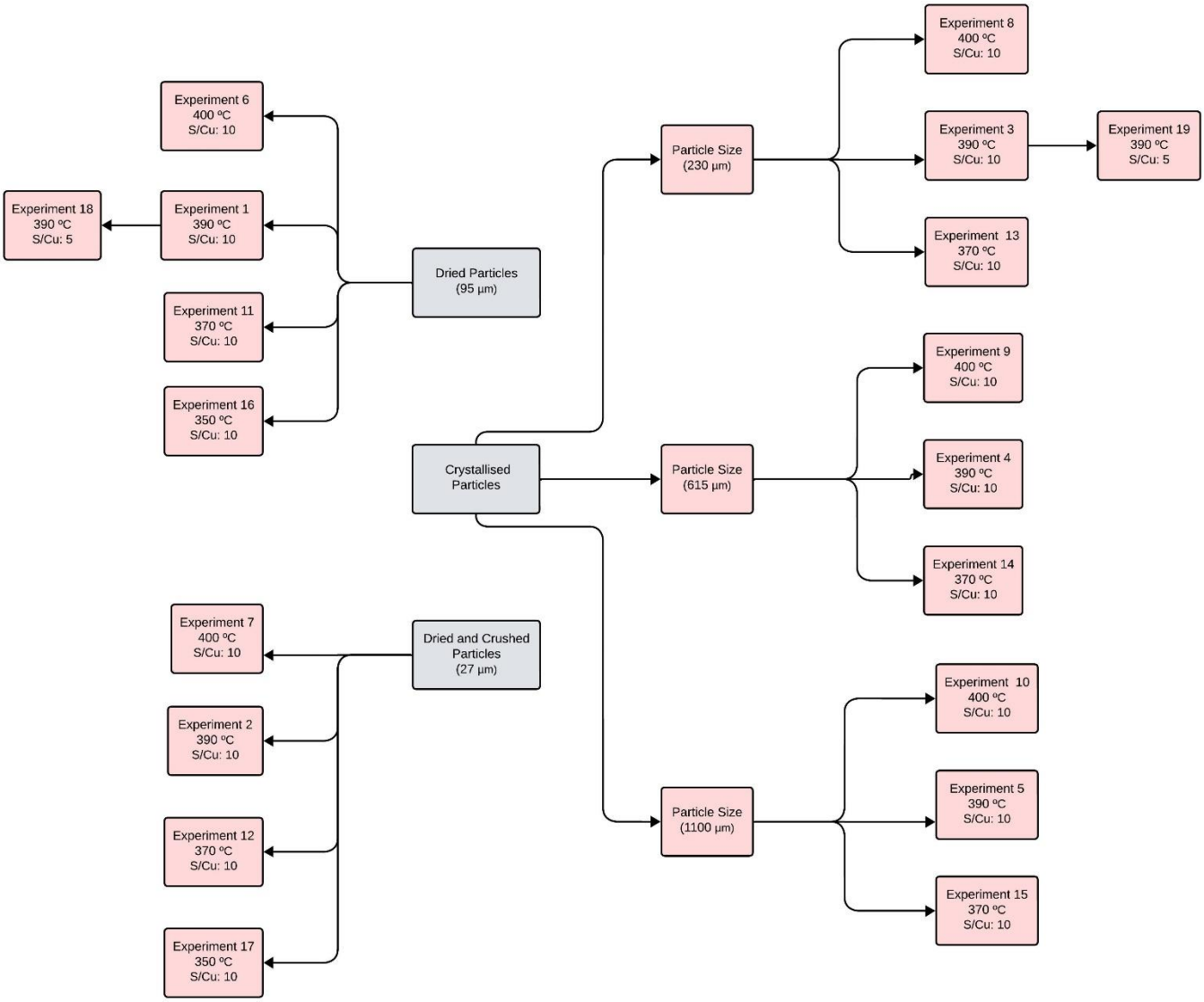

Figure 3-5: Experimental selection

Chapter 4 Shrinking Core Model of Hydrolysis Reaction

This chapter develops a shrinking core model for each resistance step while assuming spherical and cylindrical particle shapes. Assumptions and steps in the model are outlined to predict reaction kinetics and identify limiting steps. These models will then be fitted and compared with experimental data to assess their accuracy in predicting reaction behaviour. Ultimately, the goal is to elucidate the conversion as a function of time and the coefficients associated with each resistance step, which contribute to understanding the overall reaction mechanism and determining the limiting step in the process.

The shrinking core model assumes that the reaction takes place solely on the particle's surface, with the unreacted core being separated from the product layer and gradually moving towards the centre as the reaction advances. Levenspiel [5] outlined five successive steps during the reaction, each presenting a barrier to the solid conversion. Depending on the specific system, some or all of these barriers may be present, and the highest barrier or combination of barriers dictates the particle conversion rate [5]. The particle's geometry significantly influences the derivation of the model equations.

4.1 Gas Film Diffusion Control

In the context of a first-order reaction with stoichiometry as described in Equation (4-1), the diffusion of gaseous reactant A through the film surrounding the particle to the surface of the solid B can be mathematically represented by Equation (4-2). In this equation, C_{Ag} denotes the gas concentration in the bulk phase, which is assumed to remain constant throughout the reaction. At the same time, C_{As} represents the concentration at the surface, where all gaseous reactants are assumed to be reacted. Also, k_g represents the mass transfer coefficient between the fluid and the

particle [5]. As for the solid geometry, S_{ex} is the surface area of the solid particle and R is the solid particle radius.

$$aA_{(g)} + bB_{(s)} \rightarrow cC_{(s)} + dD_{(g)} \tag{4-1}$$

$$-\frac{1}{S_{ex}}\frac{dN_B}{dt} = -\frac{1}{4\pi R^2}\frac{dN_B}{dt} = -\frac{b}{4\pi R^2}\frac{dN_A}{dt} = bk_g\left(C_{Ag} - C_{As}\right) = bk_g C_{Ag} = constant \tag{4-2}$$

The quantity of substance B contained within a particle in Equation (4-3) corresponds to the molar concentration of B within the solid, denoted as ρ_B, multiplied by the volume of the particle, V. This relationship can be rearranged to represent the alteration in the radius of the reaction surface, as indicated in Equation (4-4). Upon substituting Equation (4-4) into Equation (4-2) and subsequently integrating, the duration required for the conversion process under gas film diffusion control can be determined using Equation (4-5).

$$N_B = \rho_B V = \left(\frac{moles\ B}{m^3 solid}\right)(m^3 solid) \tag{4-3}$$

$$-dN_B = -b\ dN_A = -\rho_B dV = -\rho_B d\left(\frac{4}{3}\pi r_c^3\right) = -4\pi\rho_B r_c^2 dr_c \tag{4-4}$$

$$t_f = \frac{\rho_B R}{3bk_g C_{Ag}}\left[1 - \left(\frac{r_c}{R}\right)^3\right] \tag{4-5}$$

The initial radius of the particle denoted as R, and the radius of the unreacted core, denoted as r_c, are used to define the conversion expression in Equation (4-6). By combining the constants as shown in Equation (4-7) to represent the time at complete conversion (τ_f) and substituting into Equation (4-5), the resulting expression is presented in Equation (4-8). Utilizing the same model under the assumption of a cylindrical particle shape will yield an identical conversion expression as in Equation (4-8). The time at complete conversion is represented in Equation (4-9).

$$1 - X_B = \left(\frac{volum\ of\ the\ unreacted\ core}{total\ volume\ of\ particle}\right) = \frac{\frac{4}{3}\pi r_c^3}{\frac{4}{3}\pi R^3} = \left(\frac{r_c}{R}\right)^3 \tag{4-6}$$

$$\tau_{f,sp} = \frac{\rho_B R}{3bk_g C_{Ag}} \tag{4-7}$$

$$\frac{t_f}{\tau_f} = 1 - \left(\frac{r_c}{R}\right)^3 = X_B \tag{4-8}$$

$$\tau_{f,cy} = \frac{\rho_B R}{2bk_g C_{Ag}} \tag{4-9}$$

4.2 Product Layer Diffusion Control

The movement of particles through the product's layer to the reaction's surface can be described by assuming that the reaction rate at any given moment is determined by the rate of diffusion to the surface of the reaction, as indicated in Equation (4-10). This is connected to Fick's law for equimolar counter diffusion in Equation (4-11). After integration and substitution, the time required for conversion can be expressed as shown in Equation (4-12). Subsequently, τ_d is represented in Equation (4-13), where D_e stands for the effective diffusion coefficient of the gaseous reactant in the product layer. Equations (4-12) and (4-13) are formulated based on the assumption of a spherical particle shape, while Equations (4-14) and (4-15) apply to a cylindrical shape [5].

$$-\frac{1}{S_{ex}}\frac{dN_B}{dt} = -\frac{1}{4\pi R^2}\frac{dN_B}{dt} = -\frac{b}{4\pi R^2}\frac{dN_A}{dt} = bk_g\left(C_{Ag} - C_{As}\right) = bk_g C_{Ag} = constant \tag{4-10}$$

$$-\frac{dN_A}{dt} = 4\pi r^2 D_e \frac{dC_A}{dr} = constant \tag{4-11}$$

$$\frac{t_{d,sp}}{\tau_{d,sp}} = [1 - 3(1 - X_B)^{\frac{2}{3}} + 2(1 - X_B)] \tag{4-12}$$

$$\tau_{d,sp} = \frac{\rho_B R^2}{6bD_e C_{Ag}} \tag{4-13}$$

$$\frac{t_{d,cy}}{\tau_{d,cy}} = [X_B + (1 - X_B)\ln(1 - X_B)] \tag{4-14}$$

$$\tau_{d,cy} = \frac{\rho_B R^2}{4bD_e C_{Ag}} \tag{4-15}$$

4.3 Chemical Reaction Control

The resistance of a chemical reaction, in which the rate is directly related to the surface area of the unreacted core, can be mathematically represented for a pseudo-first-order reaction using the mole balance Equation (4-16). This process involves incorporating the equation for spherical particles and replacing (r_c/R) with the conversion Equation (4-17), where τ_c is defined in Equation (4-18) and k" represents the first-order rate constant for the surface reaction. Equation (4-19) assumes cylindrical particles, with the value of τ_c remaining consistent with that in Equation (4-18) [5].

$$-\frac{1}{4\pi r_c^2}\frac{dN_A}{dt} = -\frac{b}{4\pi r_c^2}\frac{dN_A}{dt} = bk''C_{Ag} \tag{4-16}$$

$$\frac{t_{c,sp}}{\tau_c} = 1-(1-X_B)^{\frac{1}{3}} \tag{4-17}$$

$$\tau_c = \frac{\rho_B R}{bk''C_{Ag}} \tag{4-18}$$

$$\frac{t_{c,cy}}{\tau_c} = 1-(1-X_B)^{\frac{1}{2}} \tag{4-19}$$

4.4 Combined Resistance

4.4.1 Cylindrical Particle Shape

The model equations were derived in the preceding sections, assuming that a single step is controlling. However, in this section, the focus is on considering the three controlling step. At any given moment, both the gas reactant and the perimeter of the unreacted core is undergoing inward movement. It is assumed that the boundary of the solid ($r = r_c$) remains stationary concerning the diffusion of A through the product, and that there is equal molar counter diffusion of the gaseous reactant and product. Under the assumption of isothermal and steady-state behaviour, the independent treatment of A diffusion through the product layer can be observed in conjunction with the non-shrinking core. The mass balance equation for B, in combination with the diffusion rate for equal-molar counter diffusion and constant diffusivity, can be formulated as follows [61].

$$\frac{d}{dr}\left(r^2\frac{dC_A}{dr}\right)=0 \tag{4-20}$$

The process of establishing the boundary conditions for the assumption of a cylindrical shape as outlined in Equation (4-21), visually represented in Figure 4-1, is pivotal in the derivation of Equation (4-22). This development is facilitated by the clear definition of key variables: r signifies the radius at any time instance, R denotes the radius of the particle's surface, r_c represents the radius at the reaction surface, C_A denotes the concentration of the gaseous reactant at any radial position, C_{Ac} specifies the concentration of the gaseous reactant at the reaction surface, C_{As} indicates the concentration of the gaseous reactant at the particle surface, and C_{Ag} stands for the concentration of the gaseous reactant in the bulk gas.

$$r=r_c, C_A=C_{A_c}, r=R, C_A=C_{A_s} \tag{4-21}$$

$$\frac{C_A-C_{A_c}}{C_{A_s}-C_{A_c}}=\frac{\frac{\ln r}{lnr_c}-1}{\frac{\ln R}{lnr_c}-1} \tag{4-22}$$

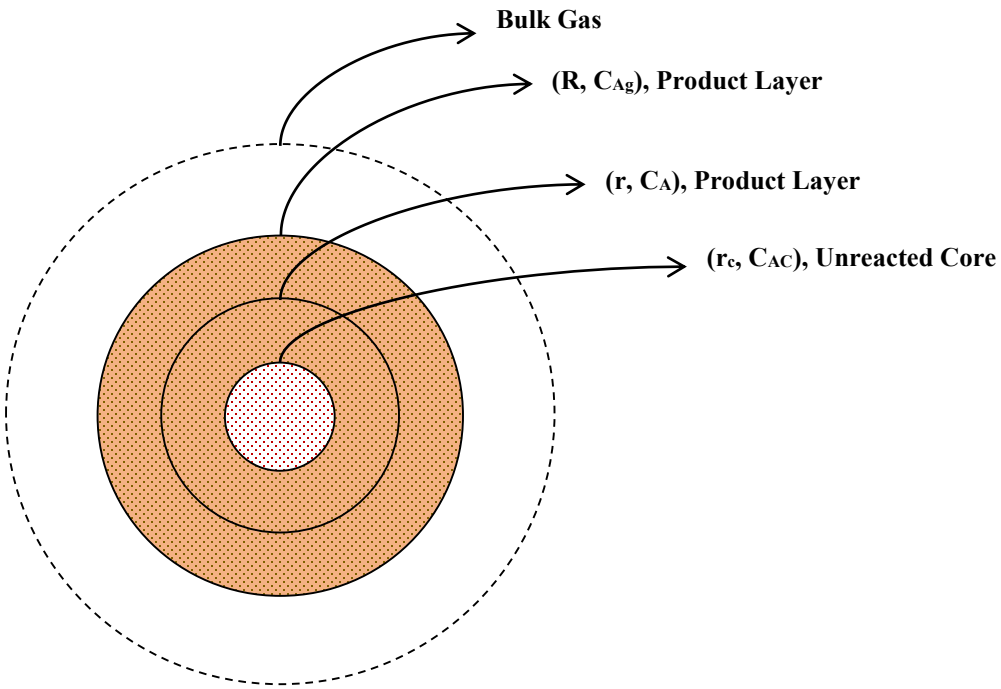

Figure 4-1: SCM boundary condition

The production rate of A can be characterized by the rate of diffusion across the gas film or the product layer, as well as the rate of reaction at the interface. These associations can be mathematically represented by the following three equations:

$$\frac{dN_A}{dt} = -2\pi \mathrm{R} \mathrm{H} k_g \left(C_{Ag} - C_{A_s}\right) \tag{4-23}$$

$$\frac{dN_A}{dt} = -2\pi r_c H D_e \left(\frac{dC_A}{dr}\right)_{r=r_c} \tag{4-24}$$

$$\frac{dN_A}{dt} = -2\pi r_c H \mathrm{k}'' C_{A_c} \tag{4-25}$$

The process of differentiating Equation (4-22), as outlined in Equation (4-26), and subsequently substituting into Equation (4-27), which represents the combination of Equations (4-24) and (4-25), results in Equation (4-28).

$$\frac{dC_A}{dr} = \frac{(C_{A_s} - C_{A_c})}{(\mathrm{ln}R - lnr_c) r_c} \tag{4-26}$$

$$C_{A_s} - C_{A_c} = \frac{\mathrm{k}'' C_{A_c} (\mathrm{lnR} - \mathrm{ln} r_c) r_c}{D_e} \tag{4-27}$$

$$C_{A_s} = C_{A_g} - \frac{r_c \, \mathrm{k}'' C_{A_c}}{\mathrm{R} k_g} \tag{4-28}$$

Equations (4-23) and (4-25) provide the expression for C_{As} in relation to C_{Ac} and C_{Ag}. Substituting this expression for C_{Ag} into Equation (4-9) results in Equation (4-29).

$$C_{A_c} = \frac{C_{A_g}/\mathrm{k}''}{\frac{r_c}{\mathrm{R} k_g} + \frac{(lnR - \mathrm{ln} r_c) r_c}{\mathcal{D}_e} + \frac{1}{k''}} \tag{4-29}$$

The next step involves establishing a relationship between the decrease in the core size and the rate of the surface reaction, and consequently, with C_{Ac}. By considering the stoichiometry of Equation (4-1) and the cylindrical particle's geometry, it is possible to determine the rate at which B is produced.

$$\frac{dN_B}{dt} = b\frac{dN_A}{dt} = \rho_B 2\pi H r_c \frac{dr_c}{dt} \tag{4-30}$$

Combining this with Equation (4-25) results in Equation (4-31). Upon integration, multiplication by D_e/R^2, and rearrangement, Equation (4-32) is obtained.

$$-\frac{dr_c}{dt} = \frac{bC_{A_g}/\rho_B}{\frac{r_c}{Rk_g} + \frac{(lnR - \ln r_c)r_c}{\mathcal{D}_e} + \frac{1}{k''}} \tag{4-31}$$

$$\frac{bC_A D_e}{\rho_B R^2}t = \left[\frac{D_e}{2k_g R} + \frac{1}{4} + \frac{D_e}{k''R}\right] - \left[\frac{D_e(1-X)}{2k_g R} + \left(\frac{D_e(1-X)^{\frac{1}{2}}}{k''R} - \frac{(1-X)\ln(1-X)}{4}\right) + \frac{(1-X)}{4}\right] \tag{4-32}$$

If the resistance ratios are determined by Equation (4-33), Equation (4-32) can be expressed as shown in Equation (4-34).

$$Y_1 = \frac{D_e}{k_g R} = \frac{\text{diffusion resistance in gas film}}{\text{diffusion resistance in product layer}}, and$$
$$Y_2 = \frac{k''R}{D_e} = \frac{\text{diffusion resistance in product layer}}{\text{reaction resistance at the interface}} \tag{4-33}$$

$$\frac{bC_A D_e}{\rho_B R^2}t = \left[\frac{Y_1}{2} + \frac{1}{4} + \frac{1}{Y_2}\right] - \left[\frac{Y_1(1-X)}{2} + \left(\frac{(1-X)^{\frac{1}{2}}}{Y_2} - \frac{(1-X)\ln(1-X)}{4}\right) + \frac{(1-X)}{4}\right] \tag{4-34}$$

4.4.2 Spherical Particle Shape

Repeating the same assumptions and equations for a spherical particle shape:

$$r = r_c, C_A = C_{A_c}, r = R, C_A = C_{A_s} \tag{4-35}$$

$$\frac{C_A - C_{A_c}}{C_{A_s} - C_{A_c}} = \frac{1 - r_c/r}{1 - r_c/R} \tag{4-36}$$

The A formation rate can be described by three equations, which can be derived from either the diffusion rate or the reaction rate. These equations are applicable to spherical shapes, and the resulting equation for the concentration of A, denoted as C_{Ac}, is presented in Equation (4-40).

$$\frac{dN_A}{dt} = -4\pi R^2 k_g\left(C_{Ag} - C_{A_s}\right) \tag{4-37}$$

$$\frac{dN_A}{dt} = -4\pi r_c^2 D_e \left(\frac{dC_A}{dr}\right)_{r=r_c} \tag{4-38}$$

$$\frac{dN_A}{dt} = -4\pi r_c^2 \mathrm{k}'' C_{A_c} \tag{4-39}$$

$$C_{A_c} = \frac{C_{A_g}/\mathrm{k}''}{\frac{r_c^2}{R^2 k_g} + \frac{(1-R)r_c}{R\mathcal{D}_e} + \frac{1}{k''}} \tag{4-40}$$

The correlation between the reduction model outlined in Equation (4-41) and the C_{Ac} expression, when integrated with Equation (4-39), yields Equation (4-42).

$$\frac{dN_B}{dt} = b\frac{dN_A}{dt} = \rho_B 4\pi r_c^2 \frac{dr_c}{dt} \tag{4-41}$$

$$-\frac{dr_c}{dt} = \frac{bC_{A_g}/\rho_{\mathrm{B}}}{\frac{r_c^2}{R^2 k_g} + \frac{(1-R)r_c}{R\mathcal{D}_e} + \frac{1}{k''}} \tag{4-42}$$

After performing integration, multiplying by D_e/R^2, and rearranging, Equation (4-43) is obtained. When the resistance ratios are defined according to Equation (4-44), Equation (4-43) can be expressed as Equation (4-45).

$$\frac{bC_{\mathrm{A}}D_{\mathrm{e}}}{\rho_{\mathrm{B}}R^2}t = \left[\frac{D_e}{3k_g\mathrm{R}} + \frac{1}{6} + \frac{D_e}{\mathrm{k''}}\right] - \left[\frac{D_e(1-X)}{3k_g\mathrm{R}} + \left(\frac{(1-X)^{\frac{2}{3}}}{2} - \frac{1-X}{3}\right) + \frac{D_e(1-X)^{\frac{1}{3}}}{\mathrm{k''}}\right] \tag{4-43}$$

$$Y_1 = \frac{D_e}{k_g \mathrm{R}} = \frac{\text{diffusion resistance in gas film}}{\text{diffusion resistance in product layer}}, and$$

$$Y_2 = \frac{\mathrm{k''}}{D_e} = \frac{\text{diffusion resistance in product layer}}{\text{reaction resistance at the interface}} \quad (4\text{-}44)$$

$$\frac{bC_{\mathrm{A}}D_{\mathrm{e}}}{\rho_{\mathrm{B}}R^2}t = \left[\frac{Y_1}{3} + \frac{1}{6} + \frac{1}{Y_2}\right] - \left[\frac{Y_1(1-X)}{3} + \left(\frac{(1-X)^{\frac{2}{3}}}{2} - \frac{1-X}{3}\right) + \frac{(1-X)^{\frac{1}{3}}}{Y_2}\right] \quad (4\text{-}45)$$

4.5 Coefficient Determination

The samples collected from the trap at one-minute intervals were analyzed for every experiment to determine the chloride concentration. The conversion of the solid particle at each data point was then calculated based on the chloride concentration. These datasets were utilised to derive the diffusion coefficient, reaction, and gas film diffusion constant from the equations in Sections 4.1, 4.2, and 4.3, assuming a single controlling step and generating a single coefficient from each equation.

In contrast, the combined resistance equations in Section 4.4, where the three resistances are combined into one equation and three coefficients exist, employed a different approach, as depicted in Figure 4-2, to generate the coefficients. Initially, the coefficients were generated for each single controlling step using the corresponding equation for each step, assuming spherical and cylindrical shapes in Sections 4.1, 4.2, and 4.3. Subsequently, the ratios Y1 and Y2 were computed and substituted in Equations (4-34) or (4-45) to calculate the new diffusion coefficient, representing the three controlling steps combined sequentially. The new diffusion coefficient was then used with the Y1 and Y2 ratios to calculate the new reaction and gas constant. The average of each constant over the entire reaction time was assessed and utilised in Equations (4-32) and (4-43) to express the final model. The coefficients were generated for each controlling step assumption and used in

their corresponding equations to plot the time versus conversion model. The resulting trends were compared with the experimental data to determine which model best represented the reaction.

4.6 Particle Size Distribution and Activation Energy

Drawing from the experimental data and the kinetics influencing the dominant resistance, it is possible to ascertain the conversion $X_B(R_i)$ for particles of varying sizes R_i and particle size fraction F. Consequently, the mean conversion $\bar{X}_B$ of the solids discharged from the reactor can be computed by effectively consolidating the contributions to conversion from all particle sizes in accordance with Equation (4-46) [5].

$$1 - \bar{X}_B = \sum [1 - X_B(R_i)] \frac{F(R_i)}{F} \tag{4-46}$$

The experimental data yield values for k", k_g, and D_e at each temperature. As the temperature varies, a correlation can be generated by linearization the Arrhenius equation when taking the natural logarithm and plotting 1/T versus lnk", $\ln k_g$, and $\ln D_e$. Furthermore, the coefficients as a temperature-dependent function can be determined for each particle size based on the controlling step for that specific particle size. The main equations are presented from Equations (4-47) to Equations (4-49), where the pre-exponential factors are $\ddot{A}_c$, $\ddot{A}_d$, and $\ddot{A}_g$, along with the apparent activation energies E_c, E_d, and E_g, while the symbol R" denotes the universal gas constant [51].

$$k" = \ddot{A}_C \exp\left(\frac{E_c}{R" T}\right) \tag{4-47}$$

$$D_e = \ddot{A}_d \exp\left(\frac{E_d}{R"T}\right) \tag{4-48}$$

$$k_g = \ddot{A}_g \exp\left(\frac{-E_g}{R"T}\right) \tag{4-49}$$

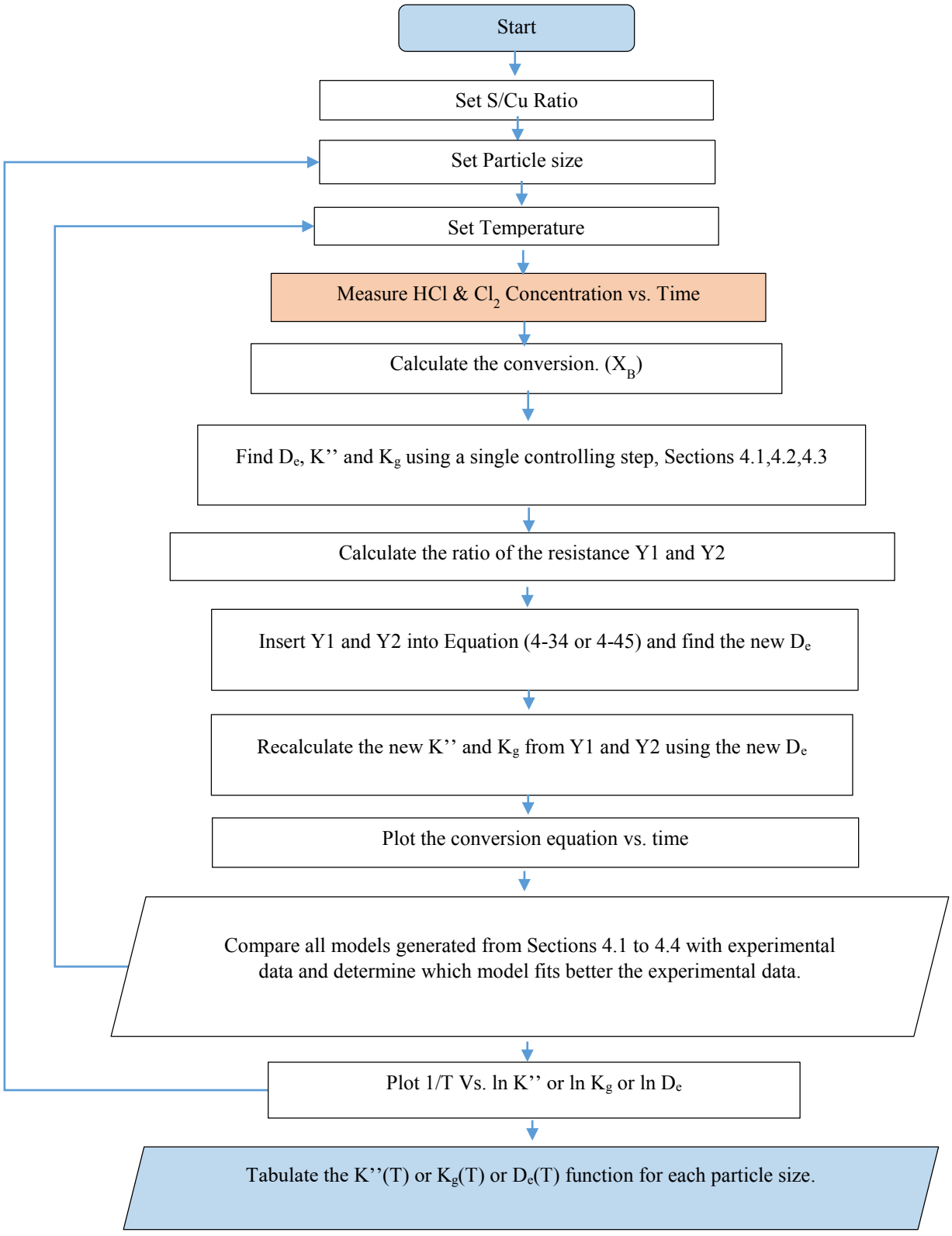

Figure 4-2: Summary of methodology used to analyze the SCM for the hydrolysis reaction

Chapter 5 Results and Discussion

This chapter presents two main sections with their main findings and discussion. The first section delineates the morphology and particle size analysis for various reactant pre-processing methods and the sieving analysis after crystallisation. The subsequent section investigates the hydrolysis reaction experimental data and the shrinking core model (SCM) as applied to the reaction.

5.1 Particle Size Analysis

SEM was used to investigate the morphology of the commercial $CuCl_2.2H_2O$ at a 500 μm imaging scale and under 1.2 x 10^{-4} chamber pressure. The crystals have a monodisperse size distribution stick shape, which can be approximated as cylindrical particles. No flakes or spherical particles were noticed. The cylindrical shape particles were between 200 - 650 μm in length and 70 - 200 μm in diameter (Figure 5-1). After the material was dried, it retained its original morphology and length, with a slight decrease in radius within the range of 35 - 180 μm (Figure 5-2). Additional processing experiments were carried out, including crushing the material without prior drying (Figure 5-3), crushing it while wet, followed by drying (Figure 5-4). The material maintained its stick-shaped particle morphology in both cases and exhibited the same dimensions as the dried particles. The material imaging after drying and crushing indicated non-uniform shapes and sizes. The imaging detector was changed from the everhart-thornley detector (ETD) to a circular backscatter detector (CBS) to get more representative imaging. Figure 5-5, Figure 5-6 and Figure 5-7 present the same spot micro-imaging at different scales, where the larger particles in Figure 5-5 maintained a cylindrical or cuboid shape with a length range of 30 - 150 μm and diameter of 20 - 70 μm. For particles with a size less than 30 μm, the shape becomes spherical and is more pronounced for particles less than 10 μm (Figure 5-7).

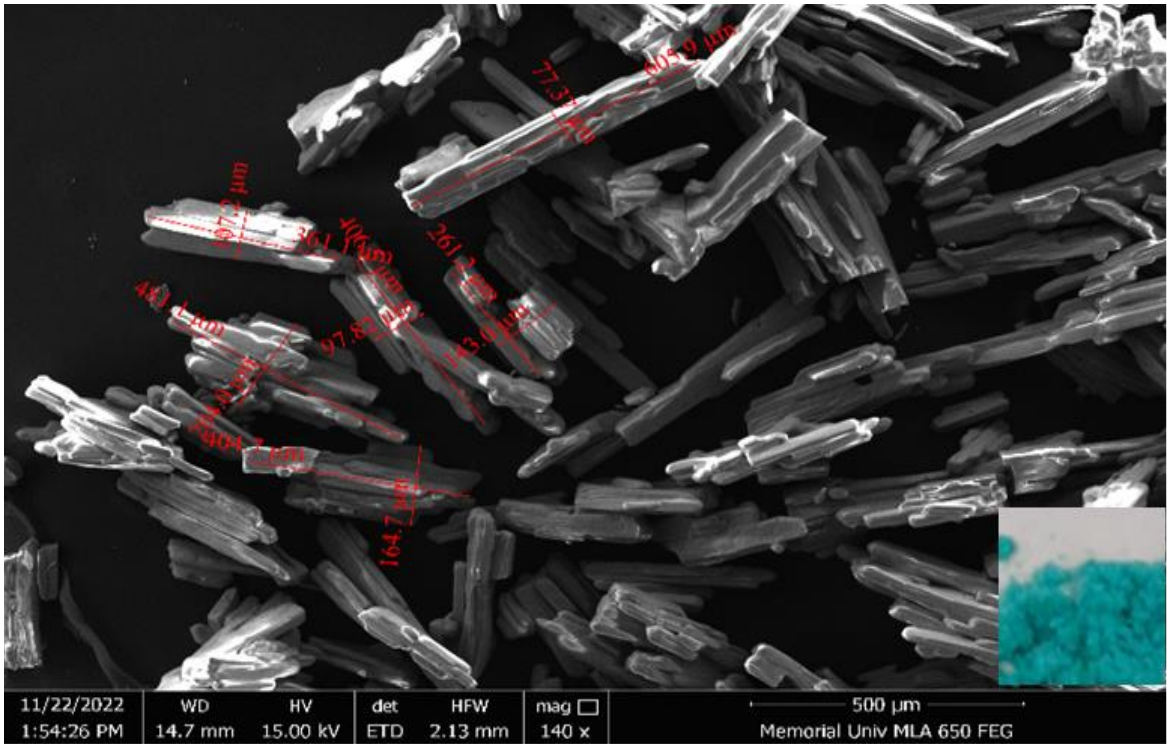

Figure 5-1: Microimaging of commercial $CuCl_2 \cdot 2H_2O$

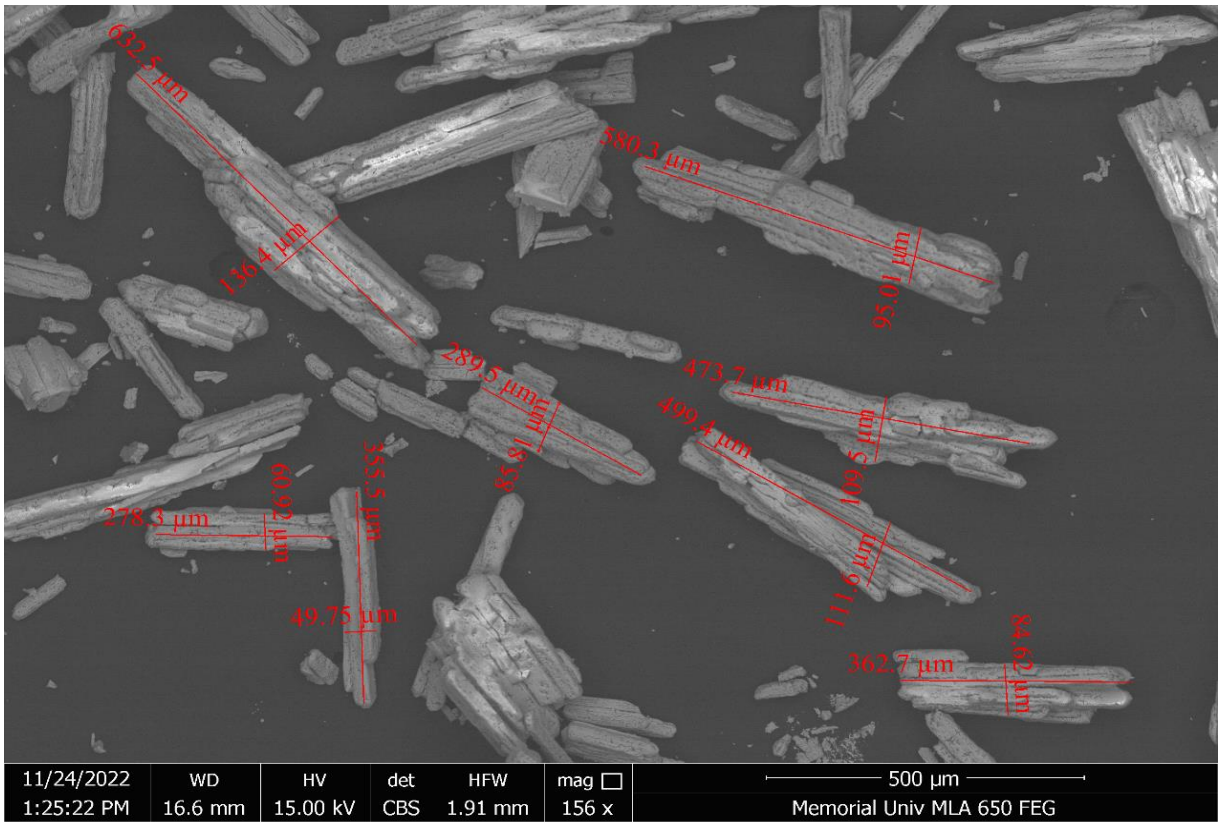

Figure 5-2: Microimaging of dried $CuCl_2$

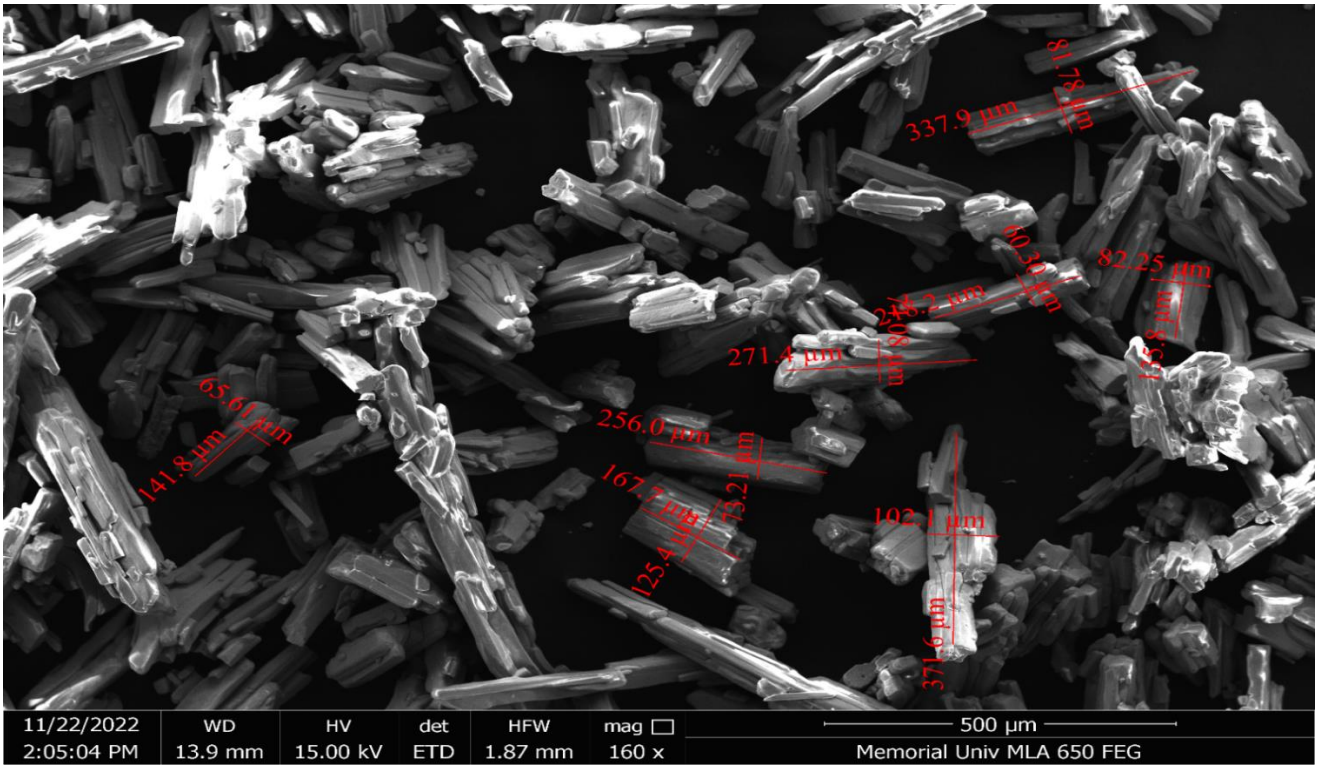

Figure 5-3: Microimaging of crushed $CuCl_2 \cdot 2H_2O$

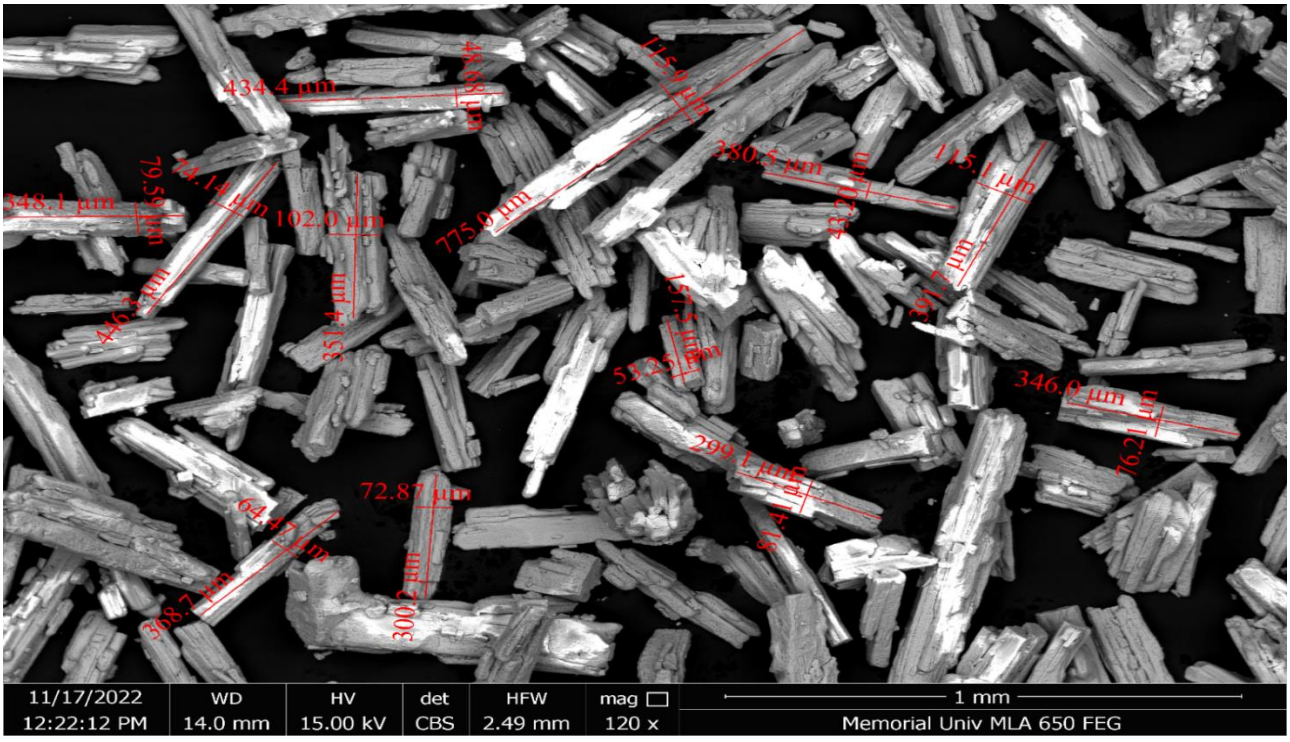

Figure 5-4: Microimaging of crushed $CuCl_2 \cdot 2H_2O$ then dried

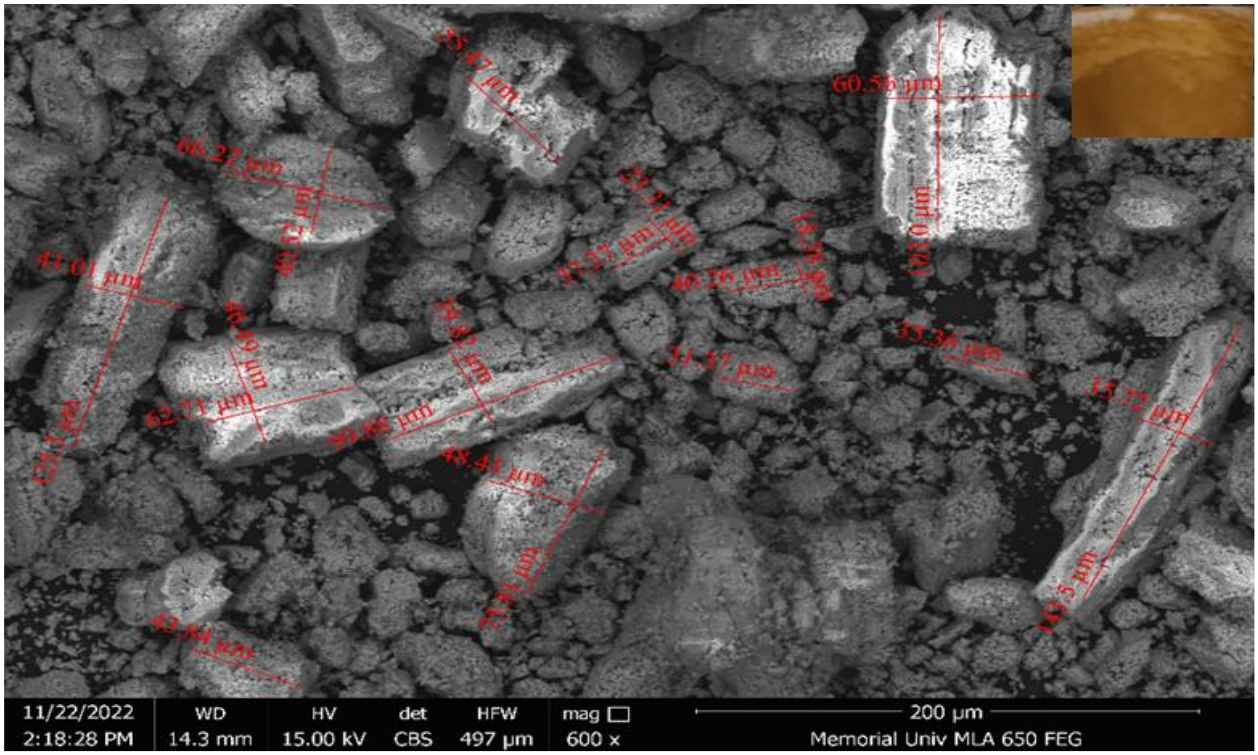

Figure 5-5: Microimaging of $CuCl_2$ after drying and crushing at 200 µm imaging scale

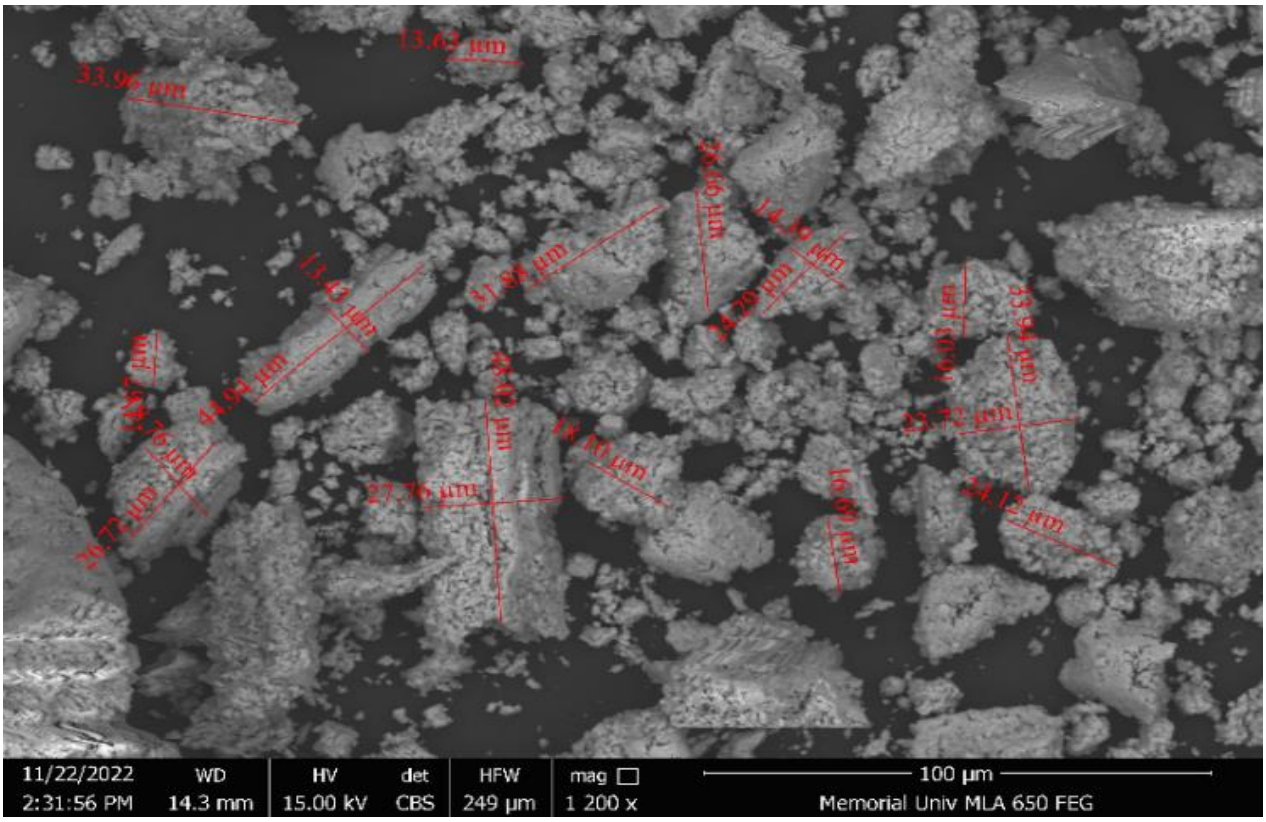

Figure 5-6: Microimaging of $CuCl_2$ after drying and crushing at 100 µm imaging scale

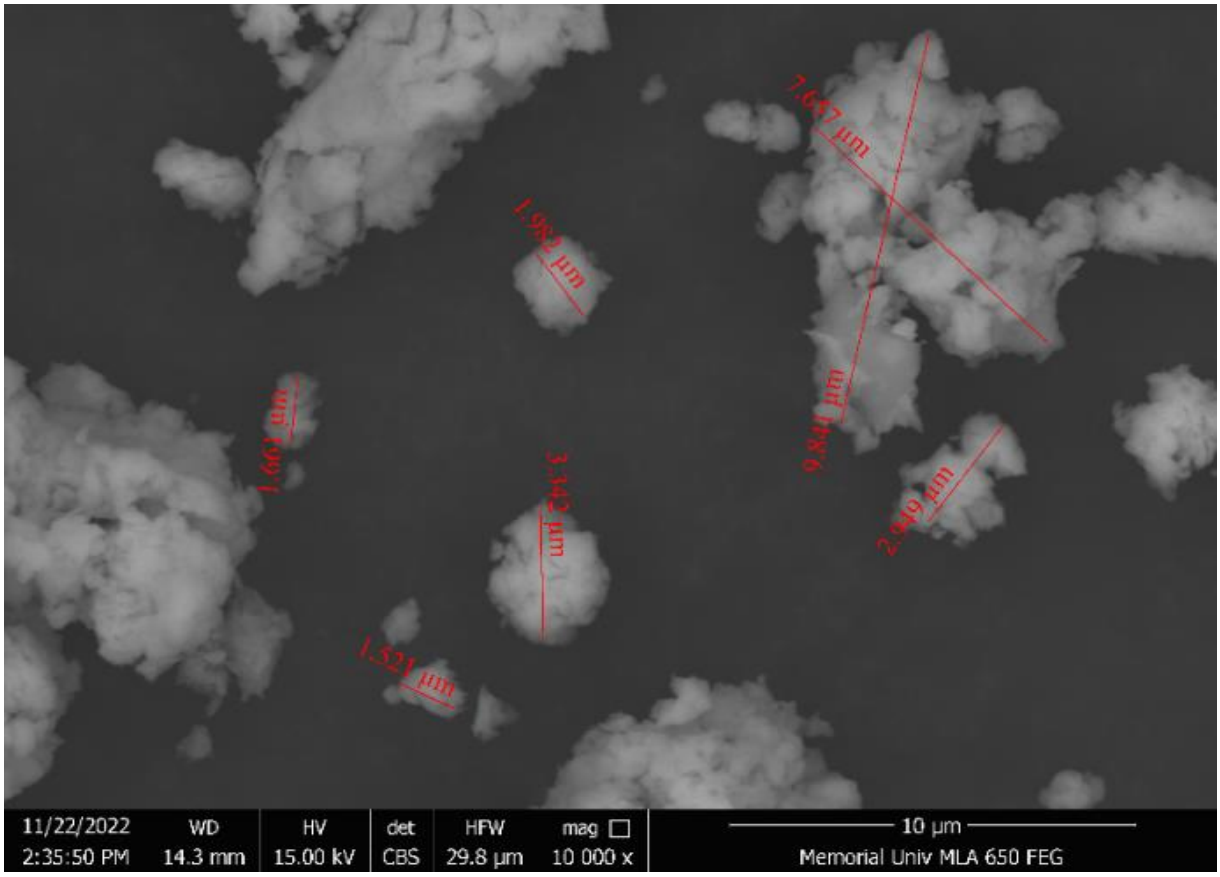

Figure 5-7: Microimaging of $CuCl_2$ after drying and crushing at 10 µm imaging scale

The crystallisation process was investigated, and a sample from the solution was extracted and dried in an oven . Under SEM scanning, the particle shape can be approximated as a cylinder or cuboid. The presence of agglomerated particles forming irregular flakes with non-uniform sizes was observed. The largest size was 1.3 mm, and the smaller flakes were less than 60 µm in size. Figure 5-8 and Figure 5-9 present an image for large and small flakes, respectively. The sample was sieved using three meshes without any further crushing. Figure 5-10, Figure 5-11 and Figure 5-12 present the imaging for particles that passed through mesh 1000, 400, and 74 µm, respectively. Despite the irregular flake and cylindrical shape, the sieving range complies with the mesh size, as shown in Table 5-1. It can be observed that crystallisation generates a larger particle diameter than the original commercial samples.

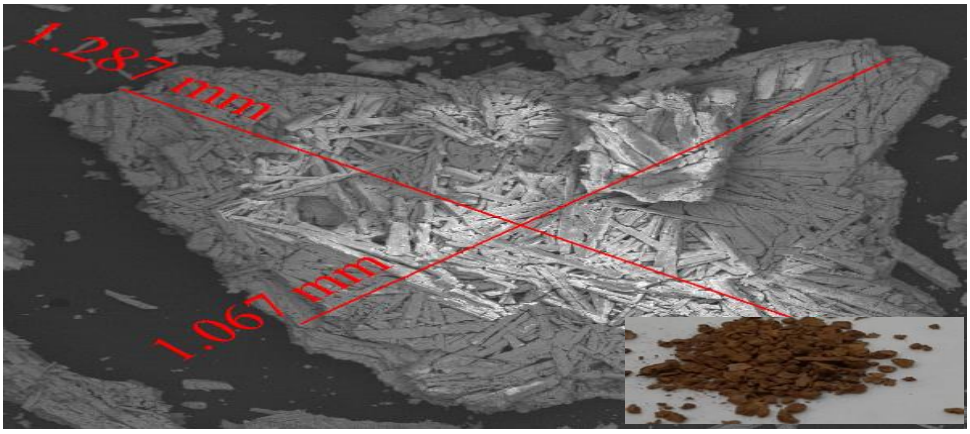

Figure 5-8: Microimaging of $CuCl_2$ large flake after crystallisation

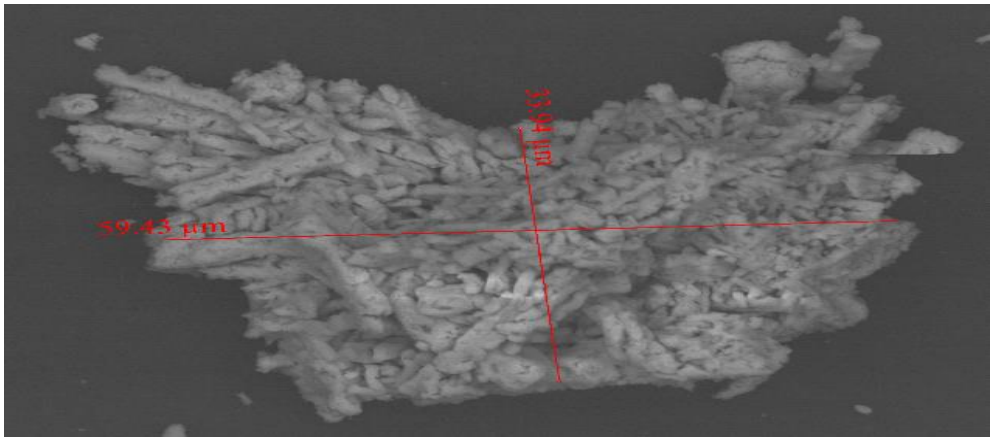

Figure 5-9: Microimaging of $CuCl_2$ small flake after crystallisation

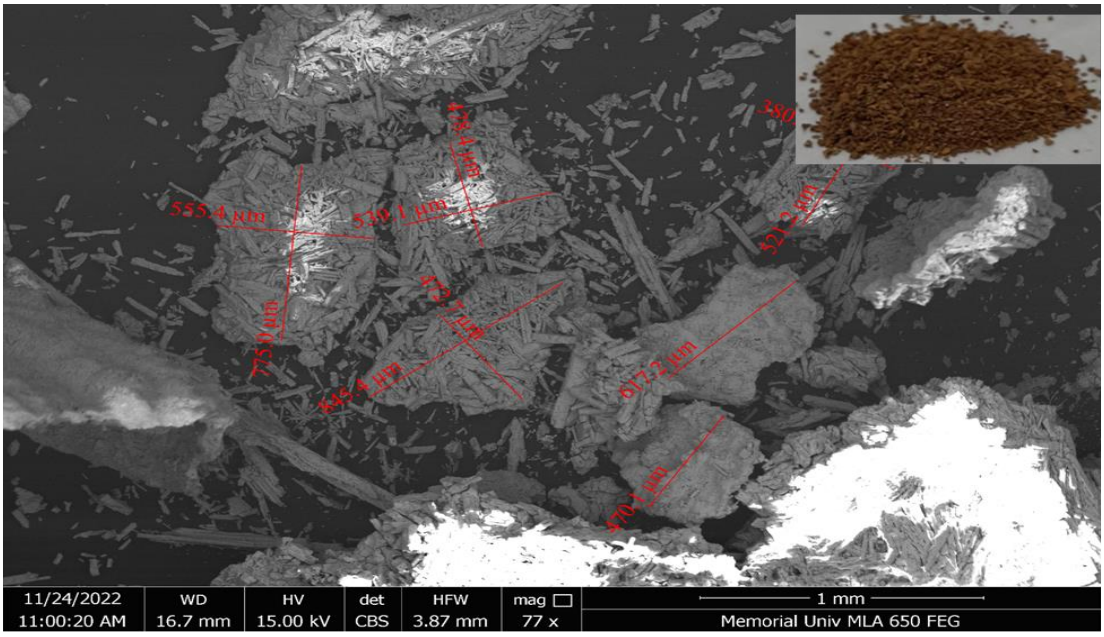

Figure 5-10: Microimaging of $CuCl_2$ after crystallisation at mesh 400 µm

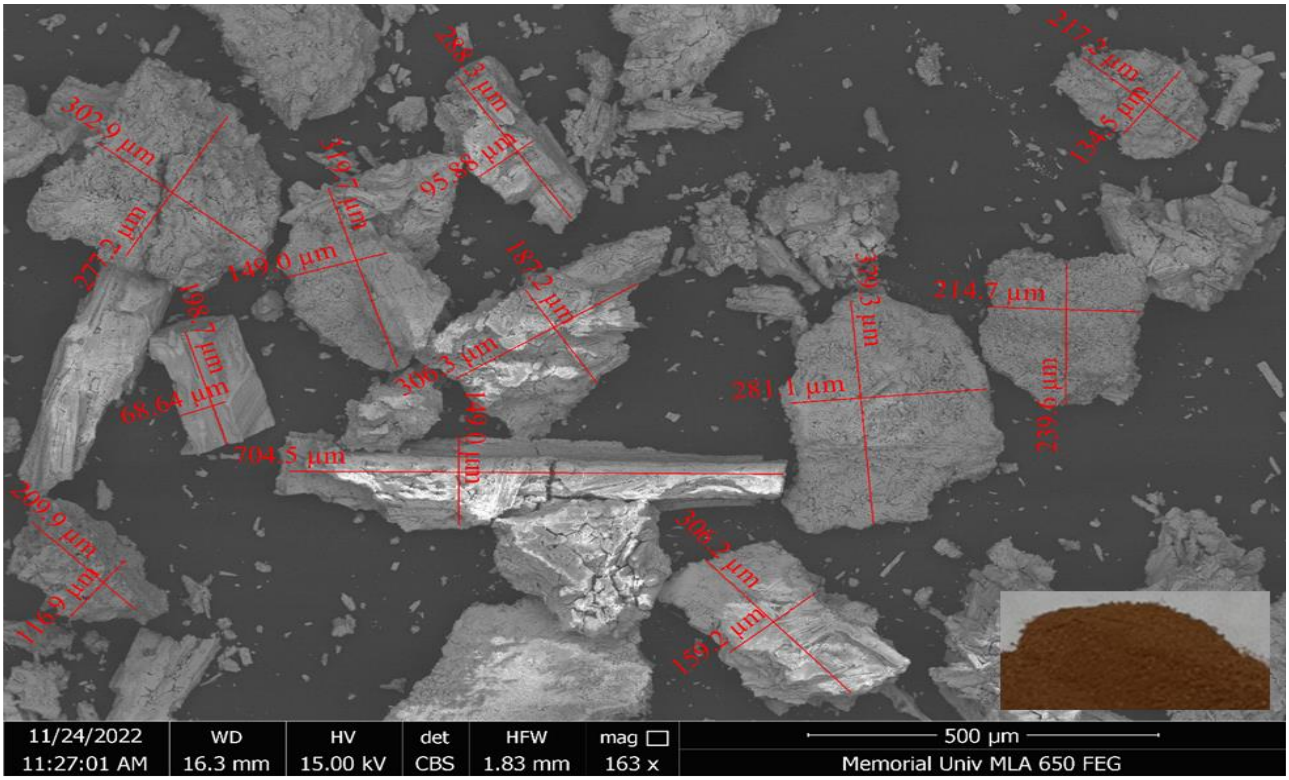

Figure 5-11: Microimaging of $CuCl_2$ after crystallisation at mesh 74 µm

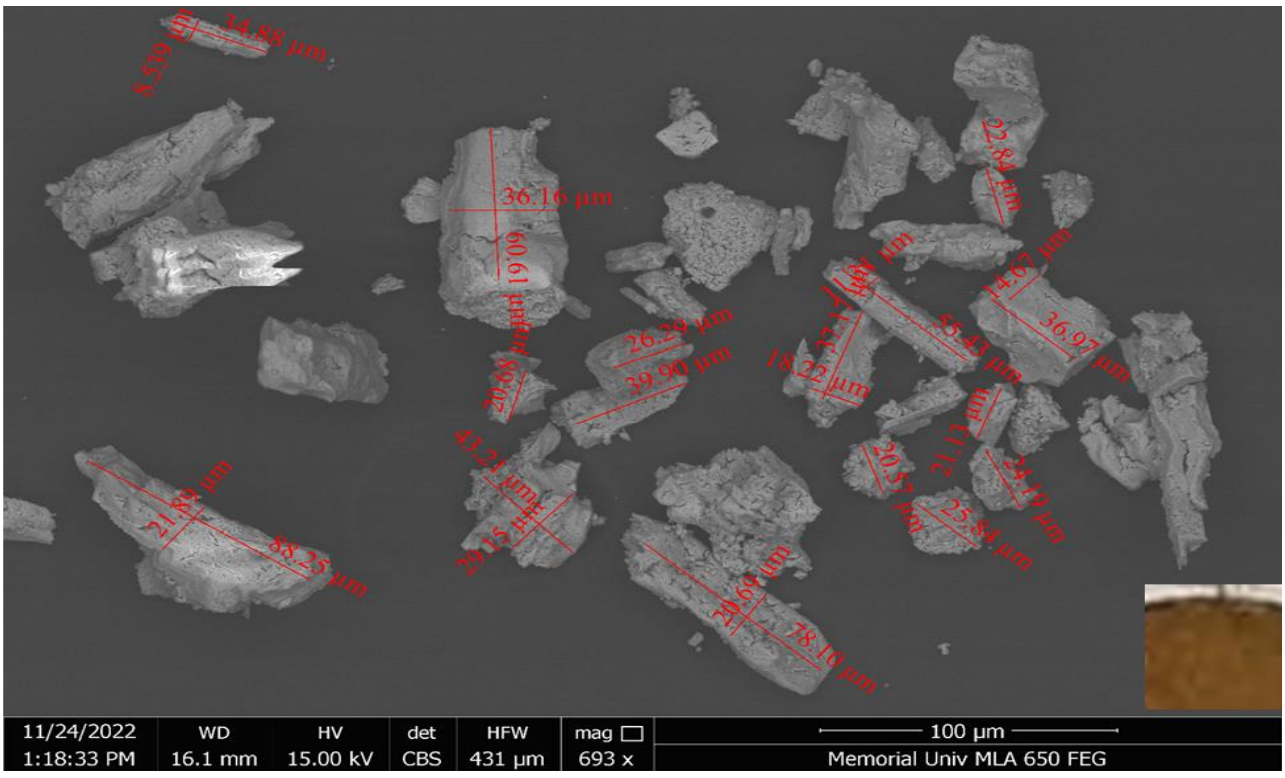

Figure 5-12: Microimaging of $CuCl_2$ after crystallisation, passed mesh 74 µm

Table 5-1: Sample Processing and Particle Size

Samples	Mesh Nominal Size Range (µm)	Particle Diameter Range from SEM (µm)	Average Particle Diameter (µm)
$CuCl_2 \cdot 2H_2O$	-	70 - 200	135
Dried	-	35 - 180	95
Dried and Crushed	-	1 - 60	27
Crystallised, Mesh 1000 Micron	More than 914	1000 - 1300	1100
Crystallised, Mesh 1000 - 400 Micron	914 - 381	850 - 380	615
Crystallised, Mesh 400 - 74* Micron	381 - 40	380 - 65	230
Passed 74*	Less than 40*	Less than 60	-

*For mesh 74, the largest particle size is in the range of 58 - 63 µm.

The dry sieve analysis method was used to determine the particle size distribution of the crystallised sample. Table 5-2 presents the mass of the sample on each sieve, the cumulative mass, and the percentage passing and retained on each sieve. Approximately 75% of the crystallised sample had an average particle diameter of 230 µm. The particle size plays a critical role in the rate of conversion and as such the total conversion of the sample will be influenced by the mass fraction of different particle sizes produced during crystallisation. The reported values represent the averages derived from multiple crystallisation samples. Figure 5-13 shows that the coefficient of uniformity (C_f) is 1.9, below 4. Similarly, the coefficient of cumulative (Cc) is 0.94, indicating a low value and suggesting that the sample is uniformly graded [67 - 70].

Table 5-2: Sieve Analysis

Mesh Number (µm)	Average Particle Diameter (µm)	Weight Retained (g)	Percentage Retained	Cumulative Percentage Retained	Percentage Finer
Mesh 1000	1100	0.584	7%	7%	93%
Mesh 400	615	1.15	15%	22%	78%
Mesh 74	230	5.95	75%	96%	4%
Pan	-	0.28	4%	100%	0%

The EDXMA analysis was used to compare the X-ray element spectrum of the samples. Figure 5-15 and Figure 5-16 present the samples after crushing and crystallisation, respectively. They are compared with Figure 5-14, which presents the $CuCl_2 \cdot 2H2O$ sample before processing. The EDXMA analysis indicated that the sample after crystallisation includes Cu and Cl elements only, which means no oxidation occurred during crystallisation. This analysis does not give information regarding the compound within the sample. Accordingly, the XRD pattern of the dried and crystallised materials were compared in Figure 5-17, revealing a similar pattern before and after crystallisation, except for the absence of the plain 001 and 111 peaks. This can be due to the change in the crystal structure, as a new crystal structure lacks certain planes or arrangements that previously contributed to a specific peak in the XRD pattern, or due to different crystallographic orientations. Crystallisation might cause the material to reorient its crystal planes in a way that the diffraction peaks previously detected are no longer in alignment with the X-ray beam. This misalignment can result in the disappearance or weakening of peaks [74 - 76].

$CuCl_2$ is generated as an aqueous solution from the electrochemical step. The selection of the material processing step between the two steps should be considered based on its feasibility within the cycle. This considers the largest particle or flake size achieved, which might affect material conversion or require more reaction time. The SCM relies on the shape and the particle size. The rate controlling step can change if the particle size becomes too large (mass transfer controlled) or too small (surface reaction controlled). It is also essential to observe material processing on the performance of the reaction, which was conducted during this study and presented hereafter to comprehensively compare the reaction kinetics for materials with different pre-processing and operation conditions.

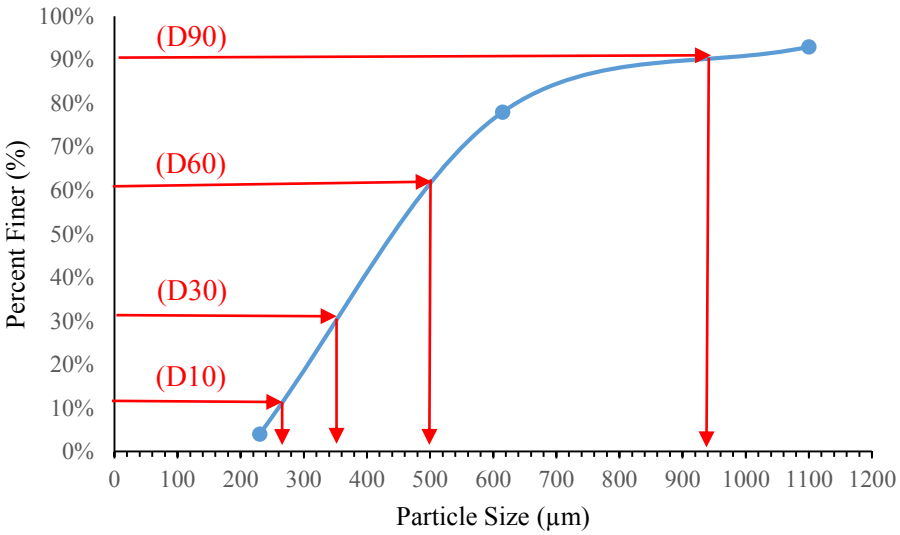

Figure 5-13: Particle size distribution curve

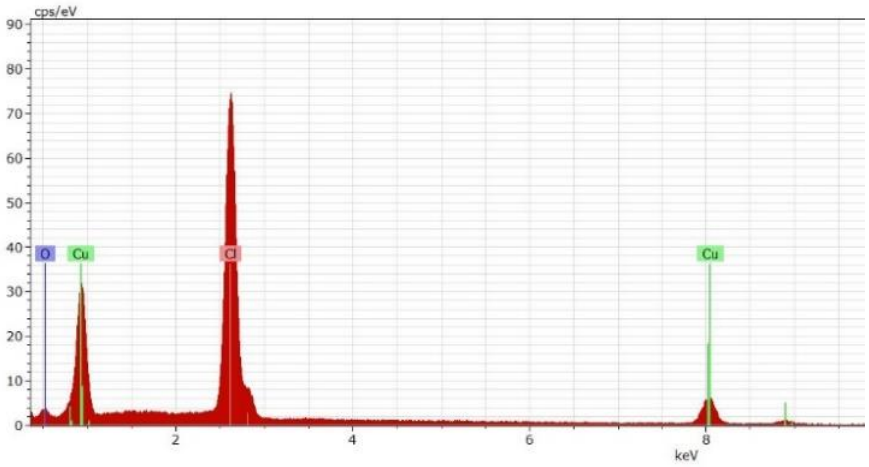

Figure 5-14: Element X-ray spectrum for commercial $CuCl_2 \cdot 2H2O$

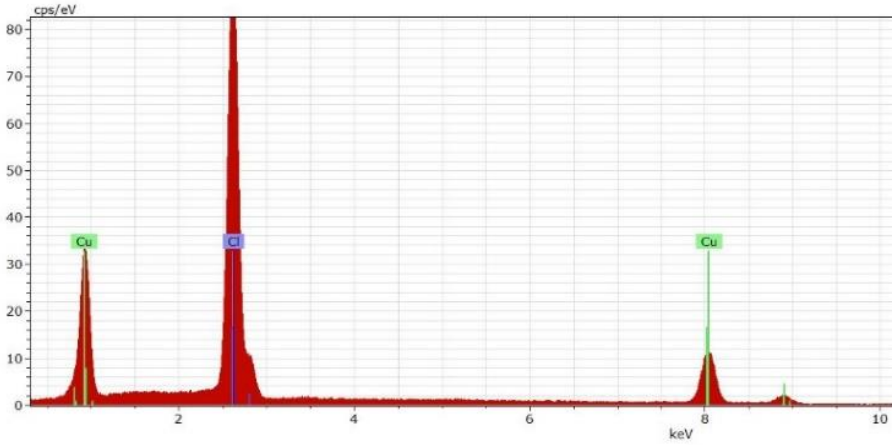

Figure 5-15: Element X-ray spectrum for crushed $CuCl_2$

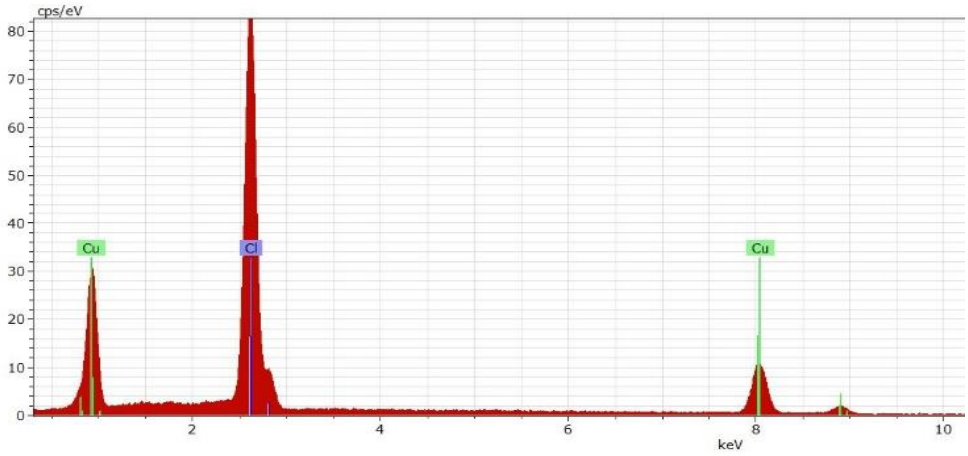

Figure 5-16: Element X-ray spectrum for $CuCl_2$ after crystallisation

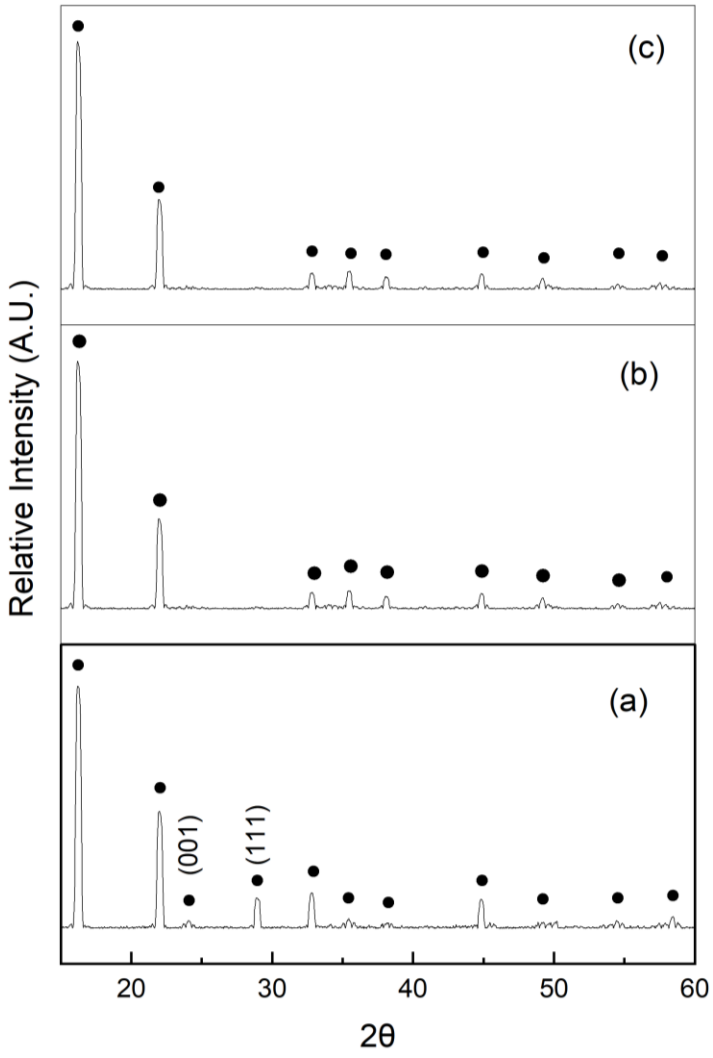

Figure 5-17: XRD Pattern, (a) Dried $CuCl_2$, (b) Crystallised $CuCl_2$, (c) Repeatable experiment of crystallised $CuCl_2$

5.2 Reaction Conversion and XRD Results

Table 5-3 shows the operational parameters and corresponding outcomes for each experiment, encompassing particle conversion and solid production as determined by X-ray diffraction (XRD). The experiments were carried out at S/Cu ratios of 10 and 5, with a steam fraction of approximately 0.3 in N_2 flow. In the temperature range of 370 - 400°C, the crushed material demonstrated the highest conversion, achieving 98% after 15 minutes at 400°C. Under identical temperature conditions, the crystallised material exhibited conversions ranging from 90% to 99% within 25 to 30 minutes, with the specific conversion dependent on the particle size of the material. Despite all crystallised samples undergoing a 30-minute reaction, titration analysis revealed that the material with a particle size of 230 μm achieved the highest conversion after 25 minutes. Conversely, the dried material achieved a 71% conversion after 30 minutes. These results show in addition to temperature and S/Cu ratio, the reaction rate is influenced by the pre-processing of the reactant material (drying, crushing, and crystallisation). These parameters are discussed and presented in detail in the following sections. However, before presenting these sections, the analysis of the solid product is presented to verify the product resulting from the hydrolysis reaction.

The X-ray diffraction (XRD) patterns for experiments other than 3, 7, and 8 in Table 5-3 revealed the presence of Cu_2Ocl_2, $CuCl_2$, and CuCl. However, experiments 3, 7, and 8 exhibited peaks of Cu_2OCl_2 and CuCl without $CuCl_2$, possibly due to the high conversion achieved within the product sample, which all comply with the expected results of the hydrolysis reaction. As for experiments 16 and 17, which were conducted at a temperature of 350°C, the XRD pattern (Figure 5-19) contained only $CuCl_2$ and CuCl peaks and none of the product (Cu_2OCl_2). This could indicate reaction of Equation (2-5) is dominating. Consequently, the experiments cannot be used in the rate analysis but they can be used to describe the decomposition reaction of $CuCl_2$.

While powder XRD diffraction can identify peaks and the presence of materials within a sample, the intensity of the peaks does not necessarily indicate the quantity of the material present. The conversion was found using the analysis method mentioned in Section 3.2; the conversion indicates the amount of $CuCl_2$ converted to the desired product Cu_2OCl_2 and the side product CuCl. However, the methods used in this study do not allow for determining the product's exact yield or the percentage of the by-product. Ferrandon et al. [47] reported a 5% formation of CuCl at 375ºC and an S/Cu ratio of 10 after 30 min of the hydrolysis reaction output. Accordingly, in this study, the quantity of by-product CuCl is assumed to be 5% of the total converted quantity.

The free Gibbs energy was analysed using HSC Chemistry software to study the equilibrium of the hydrolysis reaction. Figure 5-18 presents the hydrolysis reaction's theoretical equilibrium yields, including all possible products and by-products, resulting in a closed system with an infinite reaction time (Refer to the appendices A6 for more details). This does not indicate that the listed by-products will be present in the sample, as they might require more time. However, this information can be used to compare XRD peaks with the expected products or by-products. Figure 5-20 to Figure *5-22* presents the XRD patterns for samples taken from the reactant $CuCl_2$ and for samples taken from the reaction product.

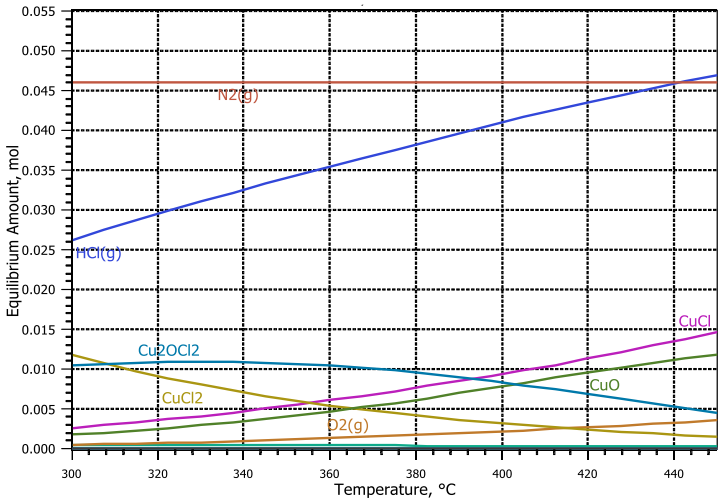

Figure 5-18: Equilibrium yields of hydrolysis reaction based on gibbs free energy calculation

Table 5-3: Experimental Parameters and Results

Experiment No.	Sample Description	Temperature °C	Particle Size (µm)	Time (min)	S/CU	Conversion (%)
1	Dried	390	95	30	10	71%[2]
2	Dried and Crushed	390	27	15	10	94%[2]
3	Crystallised	390	230	25[1]	10	97%[3]
4	Crystallised	390	615	30	10	92%[2]
5	Crystallised	390	1100	30	10	85%[2]
6	Dried	400	95	30	10	89%[2]
7	Dried and Crushed	400	27	15	10	98%[3]
8	Crystallised	400	230	25[1]	10	99%[3]
9	Crystallised	400	615	30	10	95%[2]
10	Crystallised	400	1100	30	10	90%[2]
11	Dried	370	95	30	10	69%[2]
12	Dried and Crushed	370	27	15	10	86%[2]
13	Crystallised	370	230	25[1]	10	90%[2]
14	Crystallised	370	615	30	10	85%[2]
15	Crystallised	370	1100	30	10	76%[2]
16	Dried	350	95	30	10	65%[4]
17	Dried and Crushed	350	27	15	10	77%[4]
18	Dried	390	95	30	5	36%[2]
19	Crystallised	390	230	30	5	50%[2]

[1]The reaction was conducted for 30 min, but the maximum conversion was achieved at the tabulated time.
[2]XRD Peaks: Cu_2OCl_2, $CuCl_2$, CuCl,
[3]XRD Peaks: Cu_2OCl_2, CuCl,
[4]XRD Peaks: $CuCl_2$, CuCl

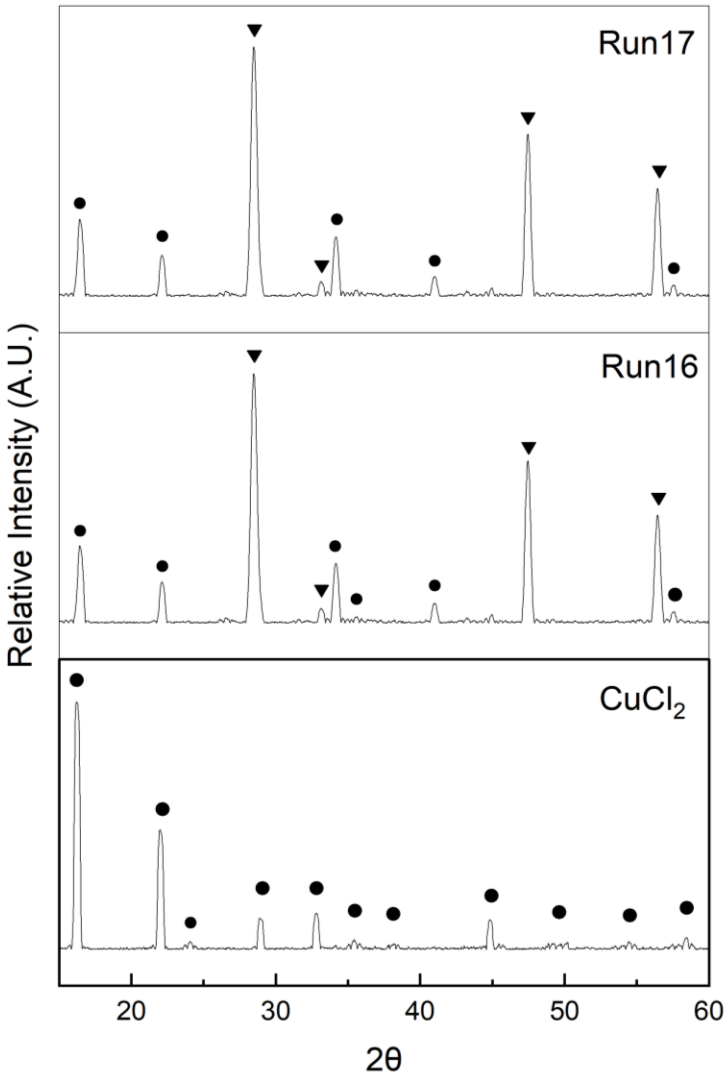

Figure 5-19: XRD pattern for hydrolysis product, (●)$CuCl_2$, (▼)CuCl

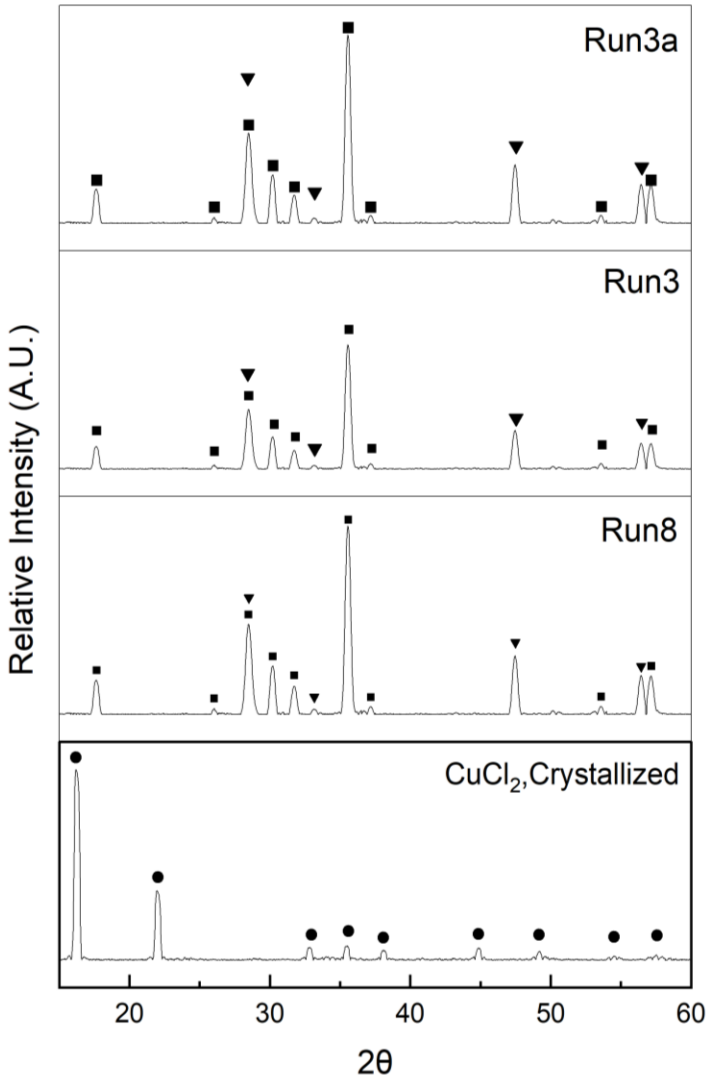

Figure 5-20: XRD pattern for hydrolysis product, (●)$CuCl_2$, (▼)CuCl, (■)Cu_2OCl_2

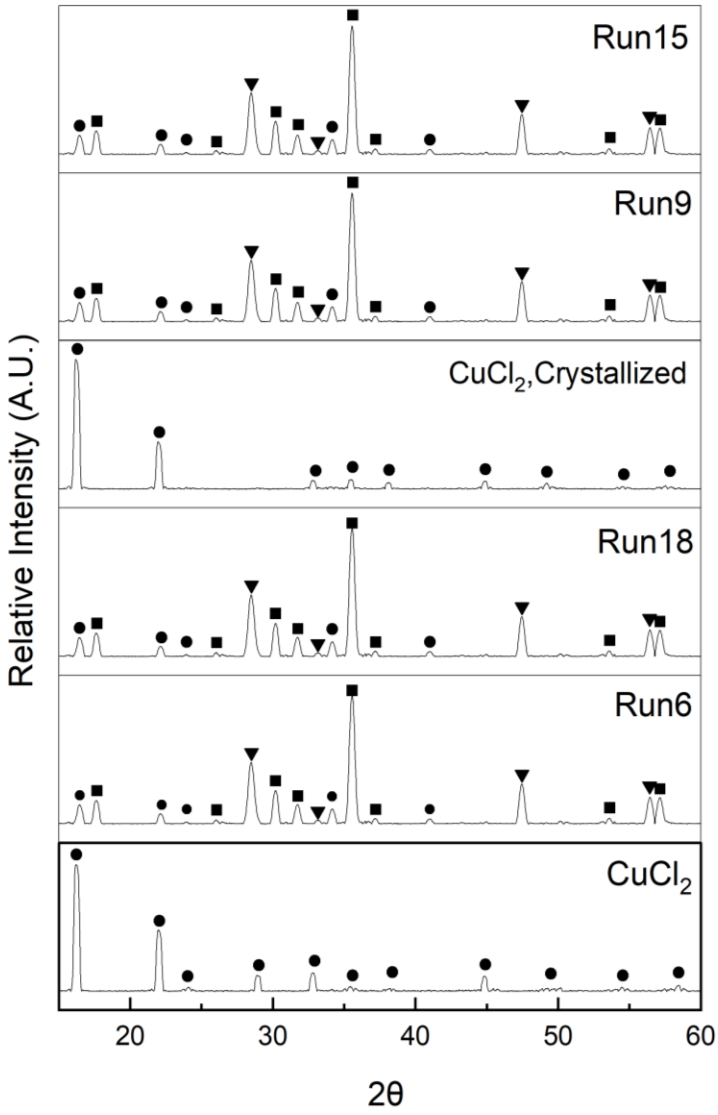

Figure 5-21: XRD pattern for hydrolysis product, (●)$CuCl_2$, (▼)CuCl, (■)Cu_2OCl_2

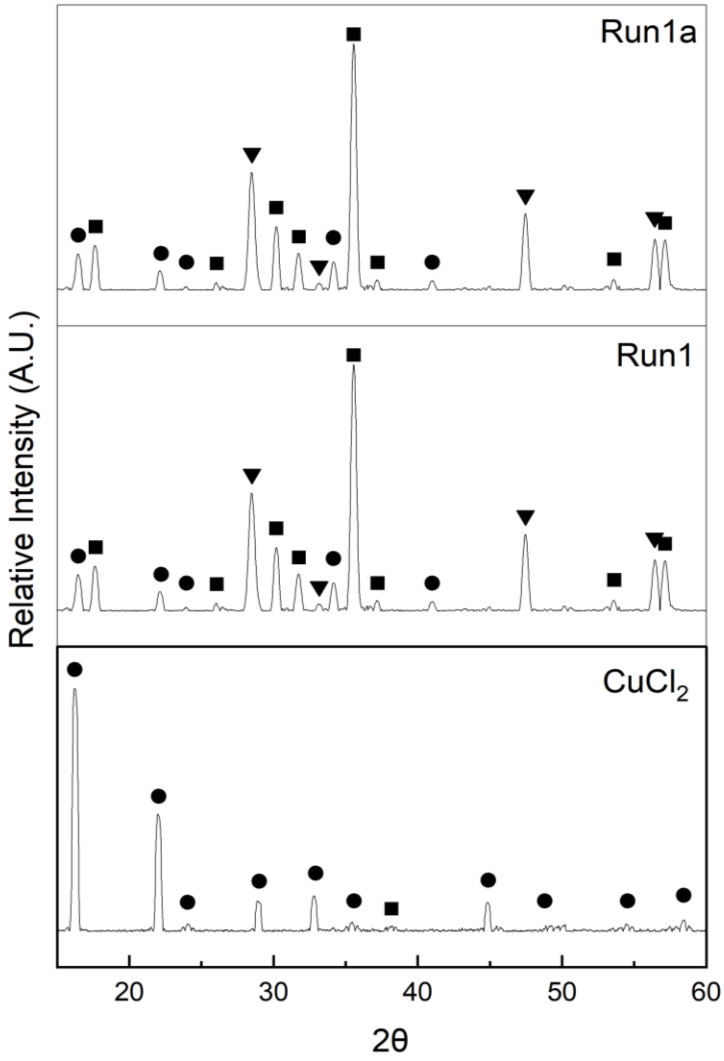

Figure 5-22: XRD pattern for hydrolysis product, (●)$CuCl_2$, (▼)CuCl, (■)Cu_2OCl_2

5.2.1 Temperature Effect

Taking into account the sensitivity of the reaction rate to temperature, as well as the heat requirement for the hydrolysis reaction and its impact on cost and cycle performance, a study was conducted on dried, crushed samples and three different particle sizes for the crystallised $CuCl_2$ as a function of temperature. The samples were reacted with steam at three different temperatures: 370°C, 390°C, and 400°C. Figure 5-23 presents the conversion rate achieved at each temperature for each sample. Conversion increases with an increase in temperature for all samples. The dried

material (95 μm) displayed the least conversions, recording 69% at 370°C, 71% at 390°C, and peaking at 89% at 400°C. In contrast, finer particle sizes such as the crushed material (27 μm) exhibited comparatively higher conversion rates, registering 86% at 370°C, escalating to 94% at 390°C, and reaching a notable 98% at 400°C. Remarkably, the crystallised material (230 μm) achieved percentages of 90%, 97%, and 99% at 370°C, 390°C, and 400°C, respectively. Similarly, larger particle sizes of crystallised material (615 μm and 1100 μm) showed conversions, recording 85% and 76% at 370°C, 92% and 85% at 390°C, reaching its highest conversion of 95% and 90% at 400°C, respectively.

Conversion as a function of time for each temperature and sample type are presented in Figure 5-24. In the case of the dried samples, the rate of conversion was slightly higher at 390°C compared to 370°C, and much higher at 400°C compared to 390°C. For the crushed sample, the rate of conversion increased only slightly with increasing temperature. The crystallised material (230 μm) did not show much differences in rate for the first 5 min, but after 5 min the 400ºC experiment showed a higher rate of conversion compared to 390°C and 370°C. A similar observation was noticed for the crystallised material of 615 μm, except that the difference between the rates at 390°C and 400°C was insignificant. For the crystallised material of 1100 μm, the rate of conversion increased as the temperature increased.

Determining the optimal operating temperature is crucial for any process. Based on the results of this study, operating at 370°C is insufficient due to the lower conversion rate. To sustain a continuous cycle with a high conversion rate, operating at 390°C or 400°C is preferable. Furthermore, careful consideration of side reactions is essential when selecting the operating temperature.

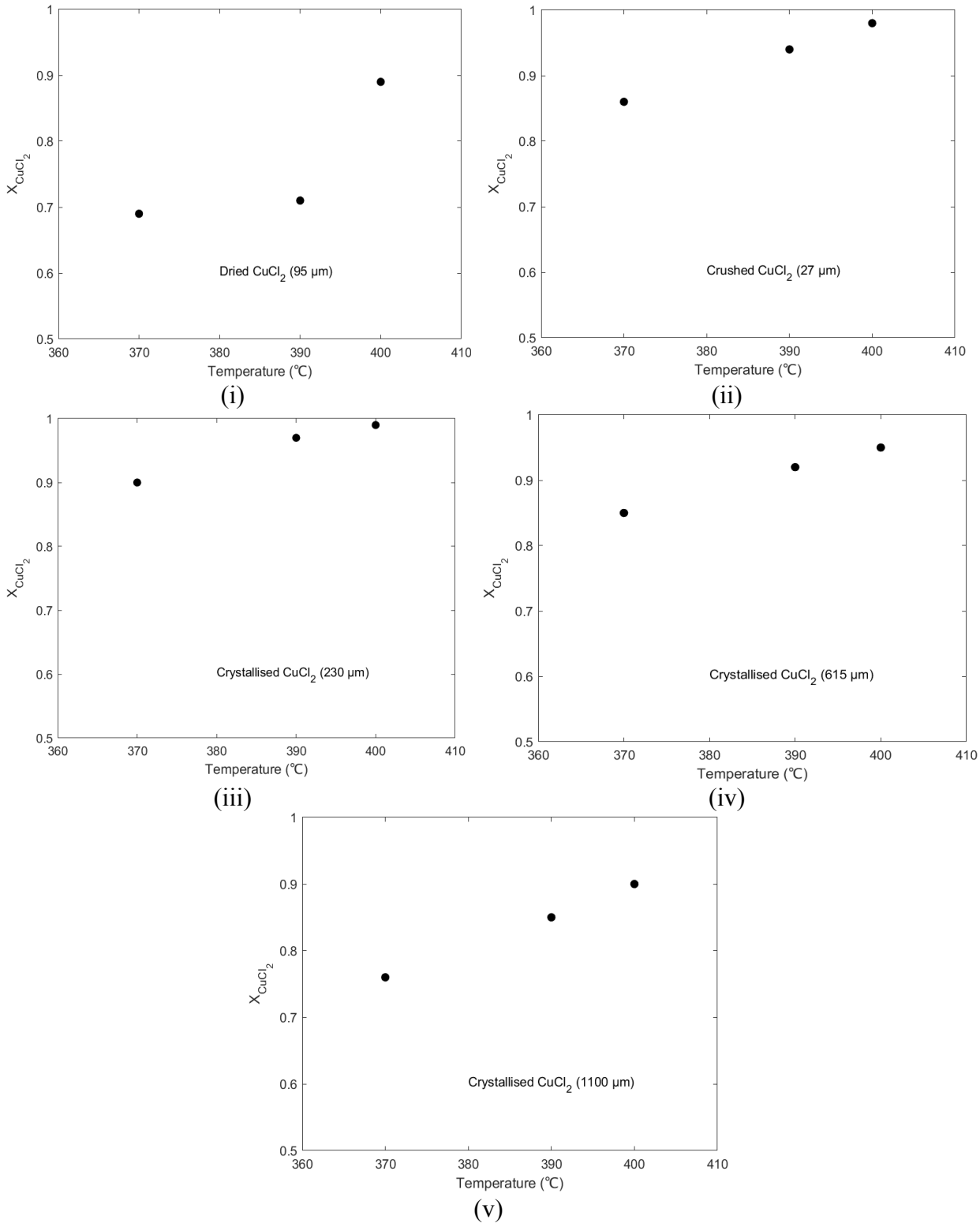

Figure 5-23: Hydrolysis reaction conversion at different temperatures and 10 S/Cu ratio. (i) Dried CuCl2 (95 µm), (ii) Crushed CuCl2 (27 µm), (iii) Crystallised CuCl2 (230 µm), (iv) Crystallised CuCl2 (615 µm), (v) Crystallised CuCl2 (1100 µm)

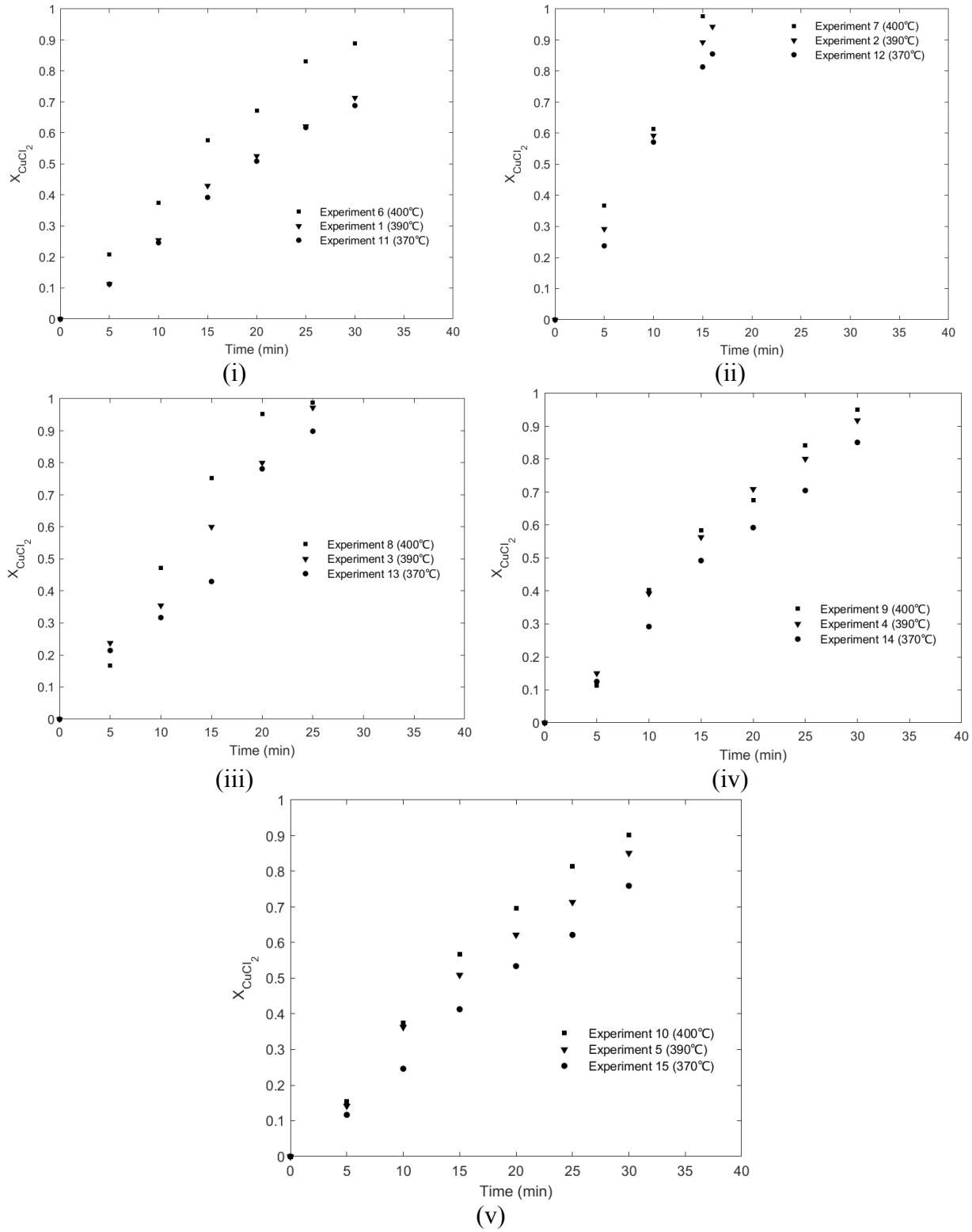

Figure 5-24: Time vs. conversion at different temperatures and 10 S/Cu ratio. (i) Dried $CuCl_2$ (95 µm), (ii) Crushed $CuCl_2$ (27 µm), (iii) Crystallised $CuCl_2$ (230 µm), (iv) Crystallised $CuCl_2$ (615 µm), (v) Crystallised $CuCl_2$ (1100 µm)

5.2.2 Particle Size Effect

Experimental data at 390°C is presented in Figure 5-25 to demonstrate the impact of particle size on the conversion. The conversion as a function of time was plotted for each of the five starting materials of $CuCl_2$ (dried 95 µm, crushed 27 µm, crystallised 230 µm, crystallised 615 µm, and crystallised 1100 µm). The dried sample showed the lowest rate of conversion, while the crushed sample showed the highest. The crystallised materials conversion rate was higher than the dried material and lower than the crushed samples. When comparing the three different particle sizes of the crystallised material (crystallised 230 µm, crystallised 615 µm, and crystallised 1100 µm), the rate of conversion increased as the particle size decreased. However, as noted above, the dried sample (95 um) showed a lower overall rate than the larger crystallised samples. The results show that particle size is not the only factor affecting the conversion, and the particle structure morphology generated due to particle crystallisation affect conversion, suggesting further investigation of the activation energies resulting from the crystallisation processes of the reactant $CuCl_2$. A detailed analysis of the activation energies will be presented in Section 5.3.4.

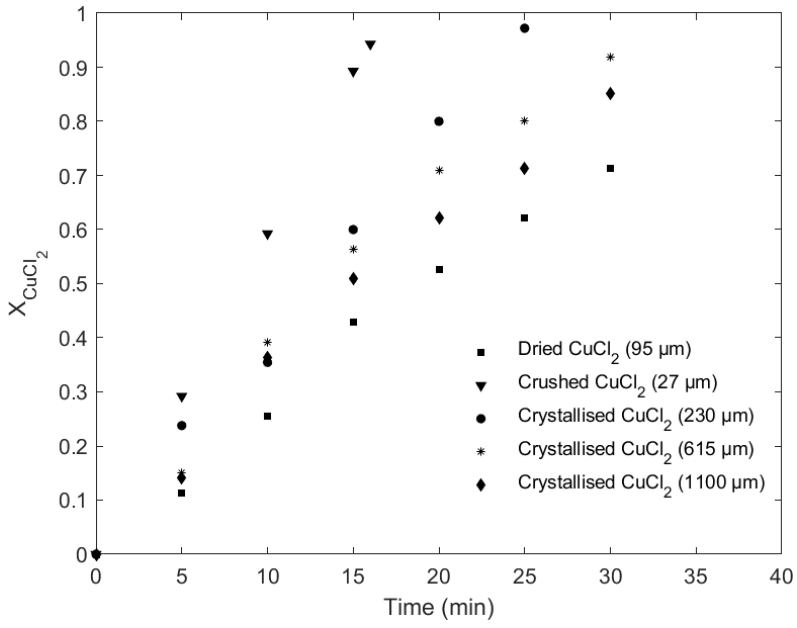

Figure 5-25: Time vs. conversion for different particle sizes at 390°C and 10 S/Cu ratio

5.2.3 Steam to Copper Ratio Effect

The last two Experiments (18 and 19) in Figure 5-26, were conducted at 390°C and a S/Cu ratio of 5 instead of 10. Both experiments resulted in low conversion rates, with the dried material of 95 µm achieving only 36% conversion, while the crystallised material of 230 µm completed 50% conversion in the same time period. In Figure 5-27, Experiments 1 and 18 are compared to show the impact of S/Cu ratio at the same temperature. The reaction rate was higher for the ratio of 10 (Experiment 1) compared to 5 (Experiment 18). The same trend was observed for the crystallised material (Figure 5-28). Ideally, operating at a lower S/Cu ratio is preferred to reduce steam consumption and consequently lower the cost of the process. However, the results indicated a very poor conversion rate at a lower ratio, suggesting the essential need to compromise the cost in order to achieve the required conversion.

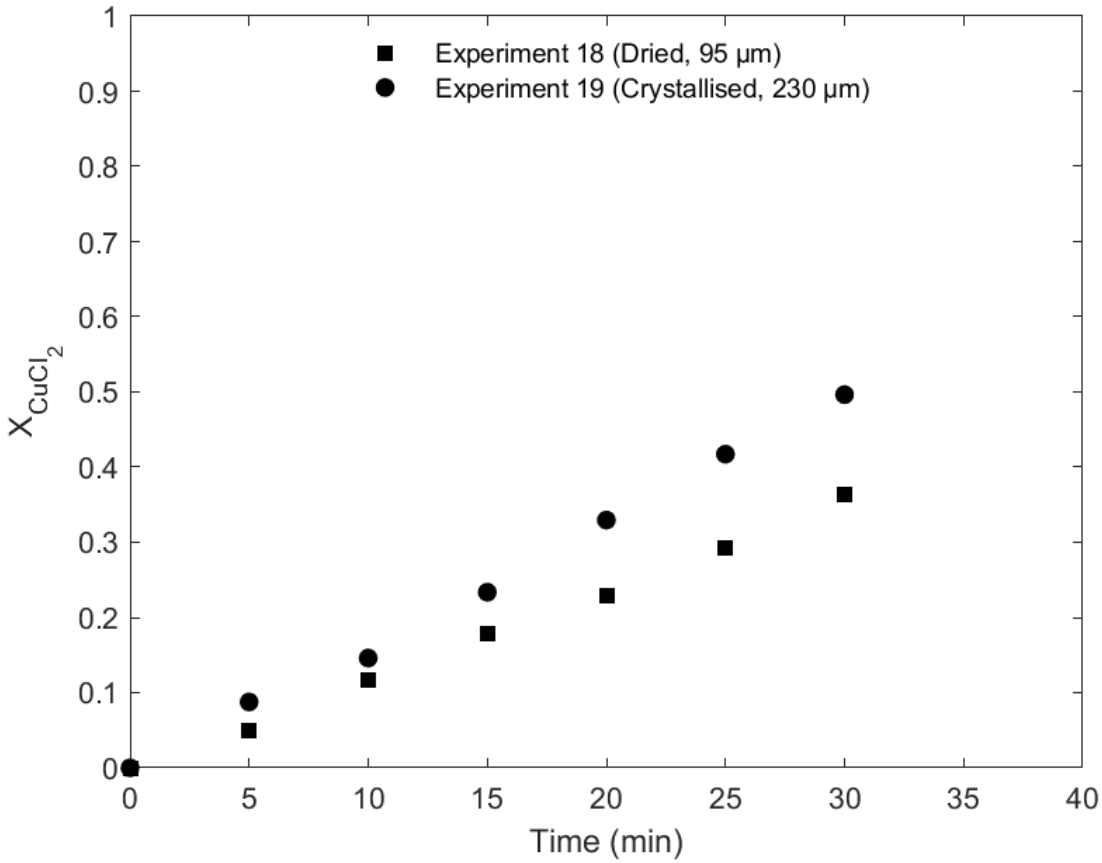

Figure 5-26: Experimental results for hydrolysis reaction at 390°C and 5 S/Cu ratio

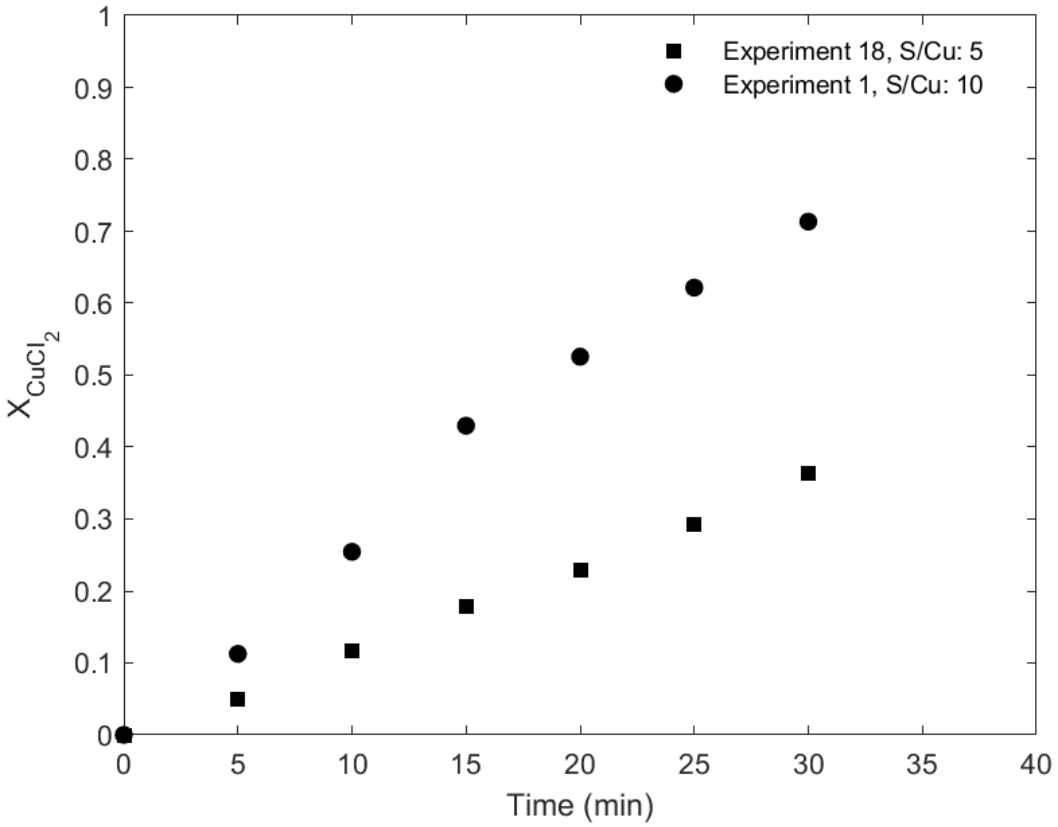

Figure 5-27: Hydrolysis reaction experimental results for dried $CuCl_2$ (95 µm) at 390°C

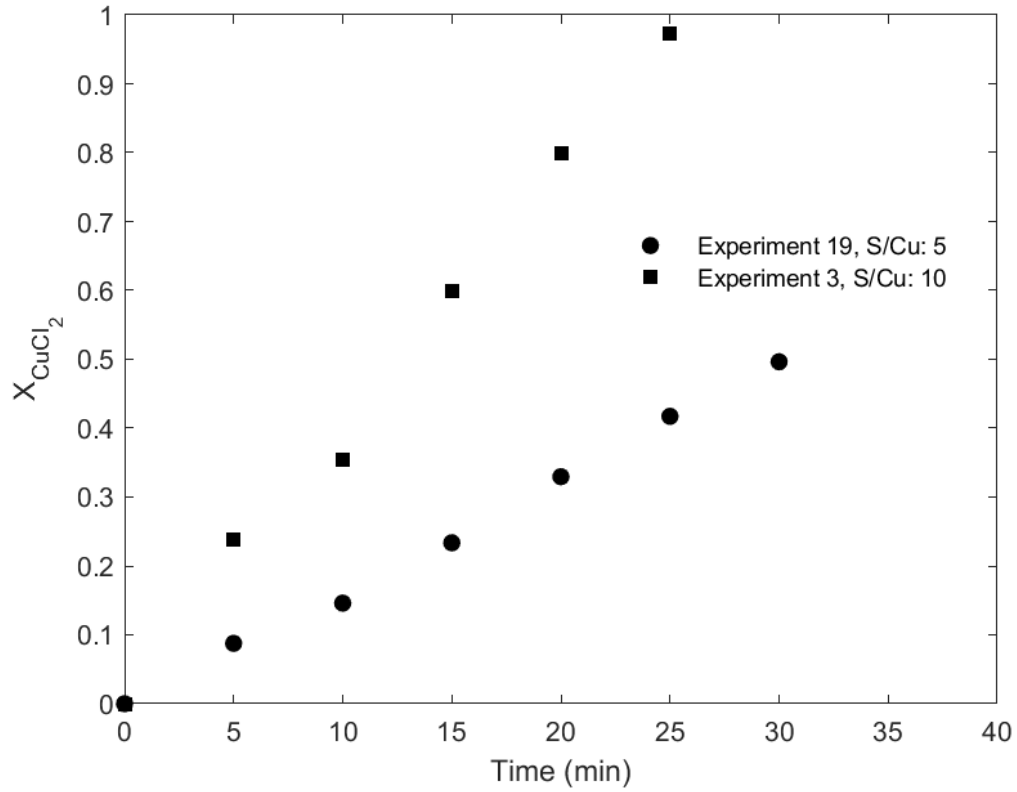

Figure 5-28: Hydrolysis reaction experimental results for crystallised $CuCl_2$ (230 µm) at 390°C

5.3 SCM Results

The SCM models were developed using data from the 19 experiments (see Figure 3-5). The SCM is a function of the particle shape, size and rate controlling step. The controlling step (surface reaction, product layer diffusion, gas film diffusion, and combined resistance) are determined by comparing the models with experimental data. The following section presents the activation energy and surface area analysis results to explain the reaction behaviour coherently. Finally, the last section integrates the particle size distribution to provide a more comprehensive prediction of the conversion process.

5.3.1 Shape Factor and Controlling Step Determination

The models were developed based on the assumption of spherical or cylindrical particle shapes. Models for single rate control (reaction, gas film diffusion, or layer diffusion) and multi-rate control (all three controlling mechanisms) for each shape were also developed in Chapter 4. A complete summary of the gas film diffusion constants, product layer diffusion coefficients and reaction constants are presented in Table A-4, and detailed figures that present all the models for both particle shape assumptions are included in the appendices. The models were compared with experimental data and the coefficient of determination (R-squared) was computed to aid in assessing the fit quality and determining the predominant controlling step. The “best” model fits for each experiment are outlined Table 5-4.

Experiments were conducted at different temperatures, employing various particle sizes and subjecting the reactant material to different processing methods (drying, crushing, and crystallisation). The results consistently indicated that, in all experiments, the cylindrical shape yielded better predictions than the spherical one. It was also observed that the diffusion control model did not effectively predict the data throughout the entire period, and the multi-rate control model underpredicted conversion. Additionally, the gas film control model demonstrated a very

similar gas film constant for both shapes. This similarity arises from the equations generated for each shape (refer to Equations (4-7), (4-8) and (4-9). Therefore, for gas film diffusion, the shape of the particle was found to have no significant effect.

Experiment 1, conducted using dried material with 95 μm at 390°C, are presented in Figure 5-29, where a comparative analysis of six models against experimental data are shown in the figure, two models assume a spherical shape (reaction control and gas film diffusion), while four models assume a cylindrical shape (reaction control, gas film diffusion, product layer diffusion, and multi-rate control). The reaction control model exhibits the most precise fit, attaining a coefficient of determination value of 0.9954. Additionally, the consideration of the last point of the reaction conversion was instrumental in determining the controlling step. The reaction control and gas film control curves for both shapes are indistinguishable until conversion exceeds ~50%. Beyond that point, the curves diverge and reaction control using a cylindrical shape shows the best fit to the data. Similar observations were made for Experiments 4 and 5 for crystallised samples with particle sizes of 615 and 1100 μm. The comparison between the different models and the experiment data is plotted in Figure 5-32 and Figure 5-33, including the error bars associated with the conversion values. The coefficient of determination (R-squared) to compare the gas film control model and the reaction control model is presented in Table 5-4.

Figure 5-30 presents the data for the crushed samples with an average particle size of 27 μm reacted in Experiment 2 at 390°C. The shape of the particle is not a factor of up to 60% conversion, with little difference between rates below 60% conversion. After 60%, the gas film appears to control. The crushed smaller particle showed 94% in 15 minutes compared to 71% in 30 minutes for the non-crushed sample (Experiment 1). There is no real difference between gas film, reaction rate, and combined curves below 60%. The rate controlling step only becomes apparent above 60% where gas film controls. This is likely due to reduced reactant concentration in gas phase (steam)

combined with reacted material increasing diffusion resistance. The experiment was conducted at 30 minutes and yielded a similar conversion, concluding that this is the maximum conversion with time for this particle size and operational condition, as detailed in the appendices.

The gas film diffusion model shows the best fit for Experiment 3 data (Figure 5-31), which represents crystallised material with a particle size of 230 μm. Considering the high rate of conversion, as discussed in the previous section, this indicates that this crystallised sample with this particle size has a faster conversion rate compared to crystallised material of other particle sizes. This leaves the gas film diffusion as the slowest step in the reaction and, therefore, the controlling step. Experiments 6 to 10 (Figure 5-34 to Figure 5-38) were conducted at 400°C (in duplicate). A similar controlling step was observed to the experiments conducted at 390°C. In Experiment 8, the experimental data achieved a conversion of 99% after 25 minutes. The gas film diffusion model predicted a 99% conversion after 20 minutes, while the reaction control model predicted a conversion of 99% after 30 minutes. Consequently, the controlling step was determined by selecting the model with the highest coefficient of determination. Experiments 11 to 15 were conducted at 370°C, as shown from Figure 5-39 to Figure 5-43, the controlling step(s) followed similar trends as experiments at 390°C, albeit with lower conversion rates.

Experiments 16 and 17 (Figure 5-44 and Figure 5-45) were carried out for dried and crushed samples at 350°C. Although the conversion of the reaction can be expressed using the SCM and the experimental data fit the surface reaction control with the cylindrical assumption, an analysis of the solid product using XRD for these two experiments (Figure 5-19) revealed that the solid only contained $CuCl_2$ and CuCl, with no product formation of Cu_2OCl_2. This indicates that the undesired reaction, Equation (2-5), dominates the desired reaction (Equation (1-1)).

Experiment 18 was conducted for the dried sample with a 95 μm particle size at a temperature of 390°C, with a S/Cu ratio of 5 instead of 10, to observe the reaction conversion rate with a reduced

steam quantity, as depicted in Figure 5-46. The ratio was reduced by decreasing the gas flow, resulting in a lower rate of conversion. The controlling step is gas film diffusion. This indicates that the driving force is lower, so the gas film diffusion plays a more significant role in the conversion rate. Similar observations were noticed in Experiment 19 (Figure 5-47), conducted for crystallised material with a 230 μm particle size at 390°C, with an S/Cu ratio of 5.

Table 5-4: The Coefficient of Determination for the SCM

Experiment No.	R^2 for Gas Film Diffusion Control	R^2 for Reaction Control	Controlling Step
Experiment 1	0.9886	**0.9954**	Reaction
Experiment 2	**0.9999**	0.9888	Gas Film Diffusion
Experiment 3	**0.9818**	0.9707	Gas Film Diffusion
Experiment 4	0.9798	**0.9953**	Reaction
Experiment 5	0.9838	**0.995**	Reaction
Experiment 6	0.9787	**0.9971**	Reaction
Experiment 7	**0.9944**	0.9806	Gas Film Diffusion
Experiment 8	**0.9784**	0.9147	Gas Film Diffusion
Experiment 9	0.9643	**0.9885**	Reaction
Experiment 10	0.97994	**0.9965**	Reaction
Experiment 11	0.9926	**0.9970**	Reaction
Experiment 12	**0.9963**	0.9902	Gas Film Diffusion
Experiment 13	**0.9553**	0.9469	Gas Film Diffusion
Experiment 14	0.9905	**0.9922**	Reaction
Experiment 15	0.9934	**0.9957**	Reaction
Experiment 16	0.9908	**0.9979**	Reaction
Experiment 17	0.9565	**0.9714**	Reaction
Experiment 18	**0.9983**	0.9963	Gas Film Diffusion
Experiment 19	**0.9973**	0.9926	Gas Film Diffusion

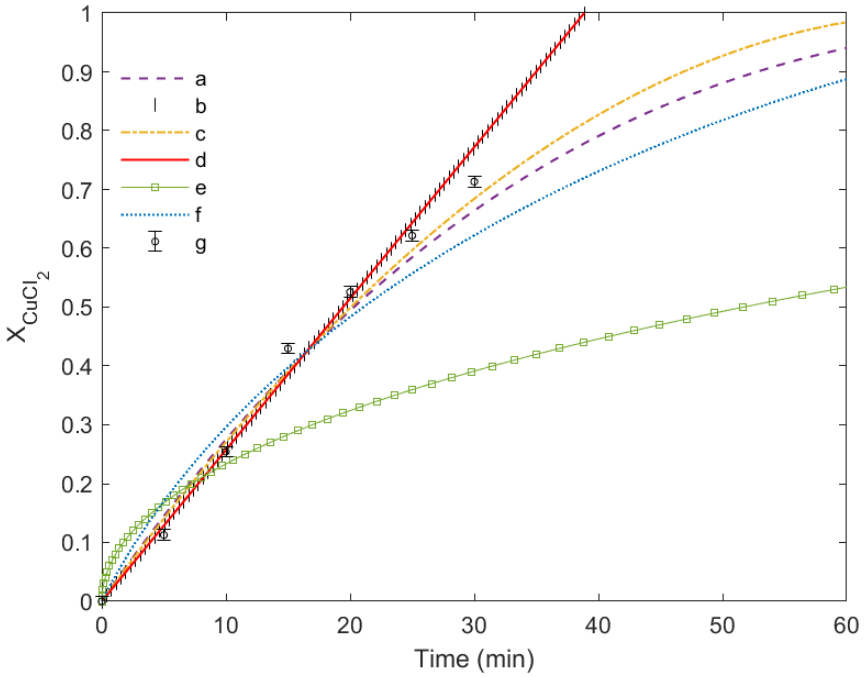

Figure 5-29: Dried $CuCl_2$ conversion with time for Experiment 1 at 390°C and 95 µm particle size, (a) Reaction control-spherical, (b) Gas film diffusion-spherical, (c) Reaction control-cylindrical, (d) Gas film diffusion-cylindrical, (e) Product layer diffusion-cylindrical, (f) Combined control-cylindrical, and (g) Experimental data

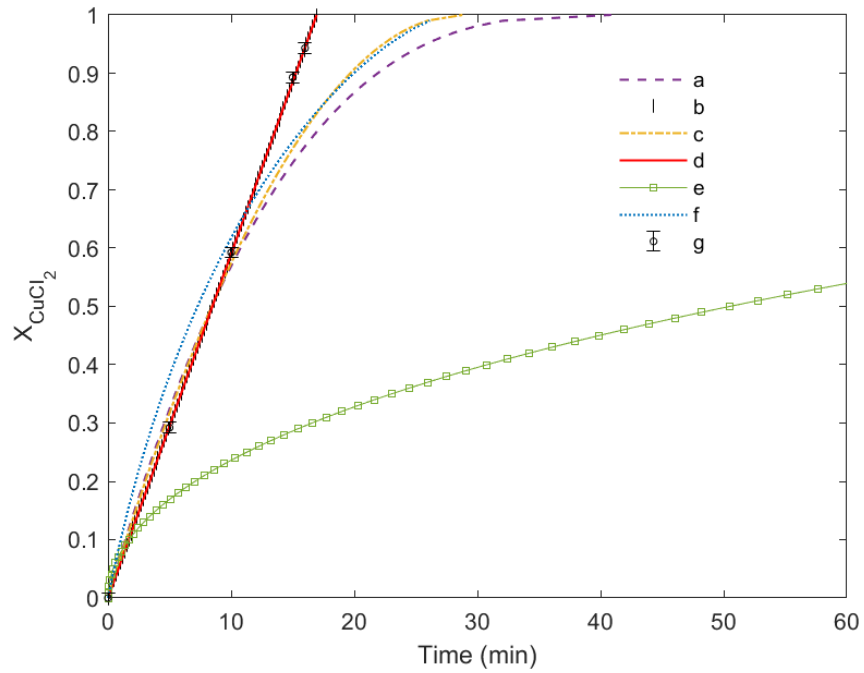

Figure 5-30: Crushed $CuCl_2$ conversion with time for Experiment 2 at 390°C and 27 µm particle size, (a) Reaction control-spherical, (b) Gas film diffusion-spherical, (c) Reaction control-cylindrical, (d) Gas film diffusion-cylindrical, (e) Product layer diffusion-cylindrical, (f) Combined control-cylindrical, and (g) Experimental data

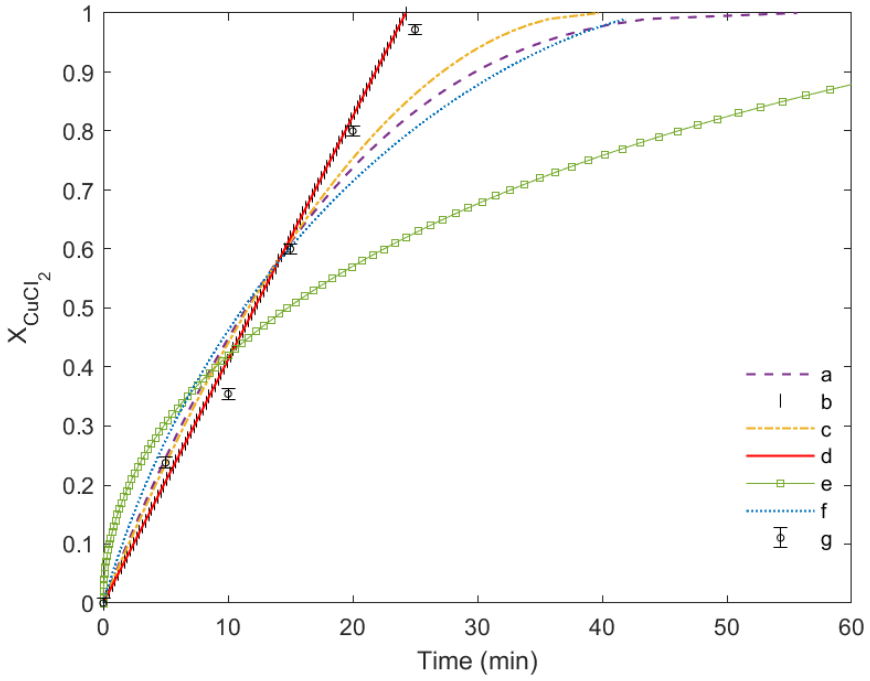

Figure 5-31: Crystallised $CuCl_2$ conversion with time for Experiment 3 at 390℃ and 230 µm particle size, (a) Reaction control-spherical, (b) Gas film diffusion-spherical, (c) Reaction control-cylindrical, (d) Gas film diffusion-cylindrical, (e) Product layer diffusion-cylindrical, (f) Combined control-cylindrical, and (g) Experimental data

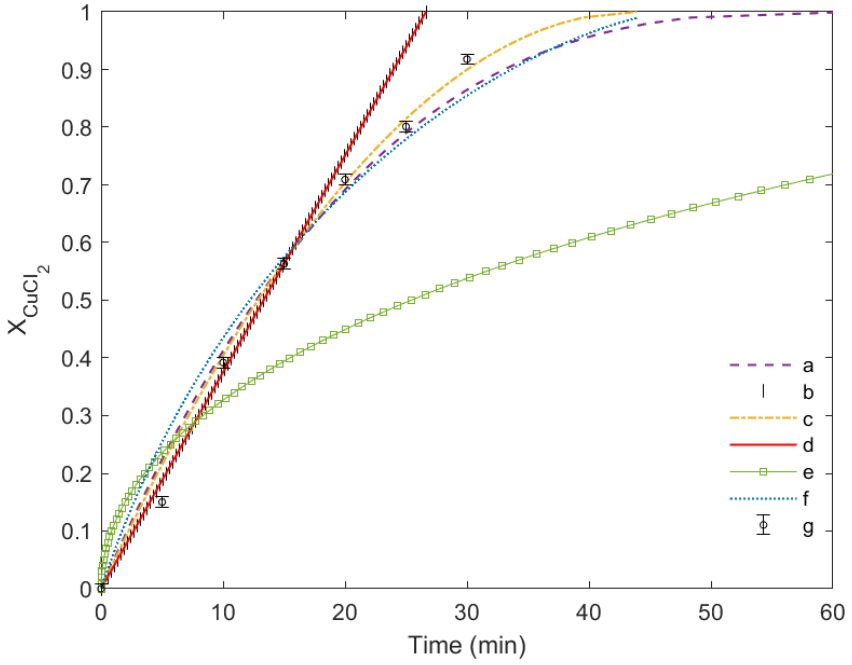

Figure 5-32: Crystallised $CuCl_2$ conversion with time for Experiment 4 at 390℃ and 615 µm particle size, (a) Reaction control-spherical, (b) Gas film diffusion-spherical, (c) Reaction control-cylindrical, (d) Gas film diffusion-cylindrical, (e) Product layer diffusion-cylindrical, (f) Combined control-cylindrical, and (g) Experimental data

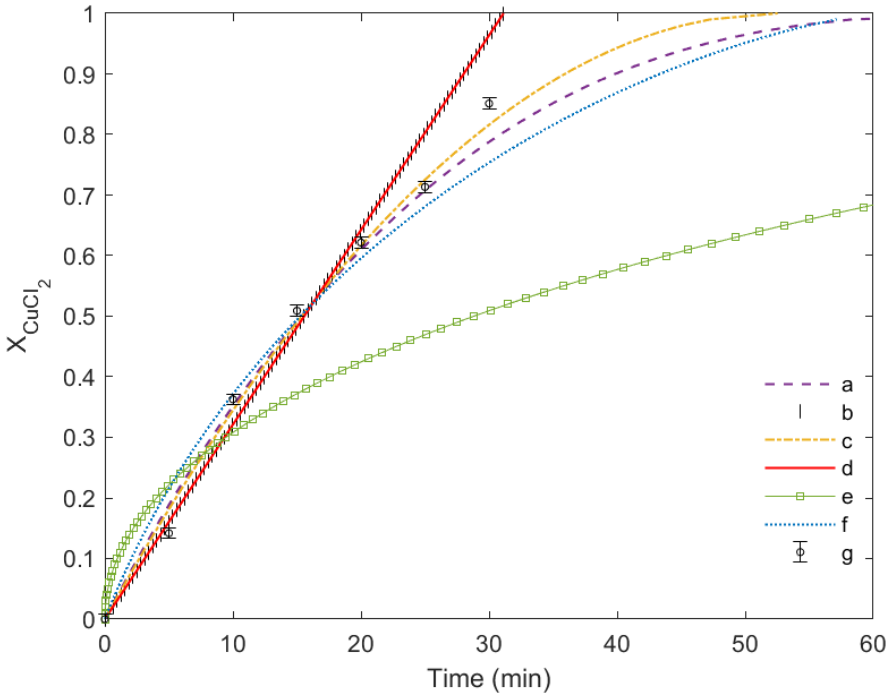

Figure 5-33: Crystallised $CuCl_2$ conversion with time for Experiment 5 at 390°C and 1100 µm particle size, (a) Reaction control-spherical, (b) Gas film diffusion-spherical, (c) Reaction control-cylindrical, (d) Gas film diffusion-cylindrical, (e) Product layer diffusion-cylindrical, (f) Combined control-cylindrical, and (g) Experimental data

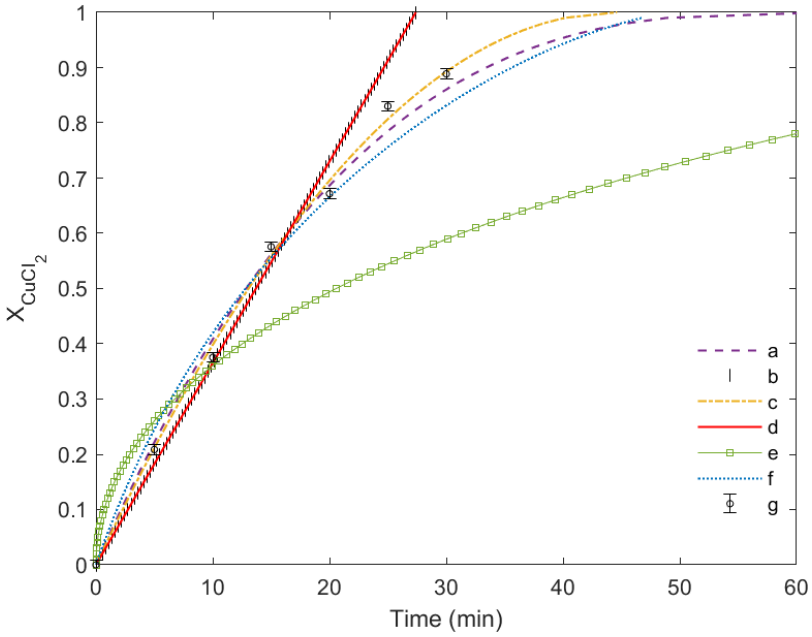

Figure 5-34: Dried $CuCl_2$ conversion with time for Experiment 6 at 400°C and 95 µm particle size, (a) Reaction control-spherical, (b) Gas film diffusion-spherical, (c) Reaction control-cylindrical, (d) Gas film diffusion-cylindrical, (e) Product layer diffusion-cylindrical, (f) Combined control-cylindrical, and (g) Experimental data

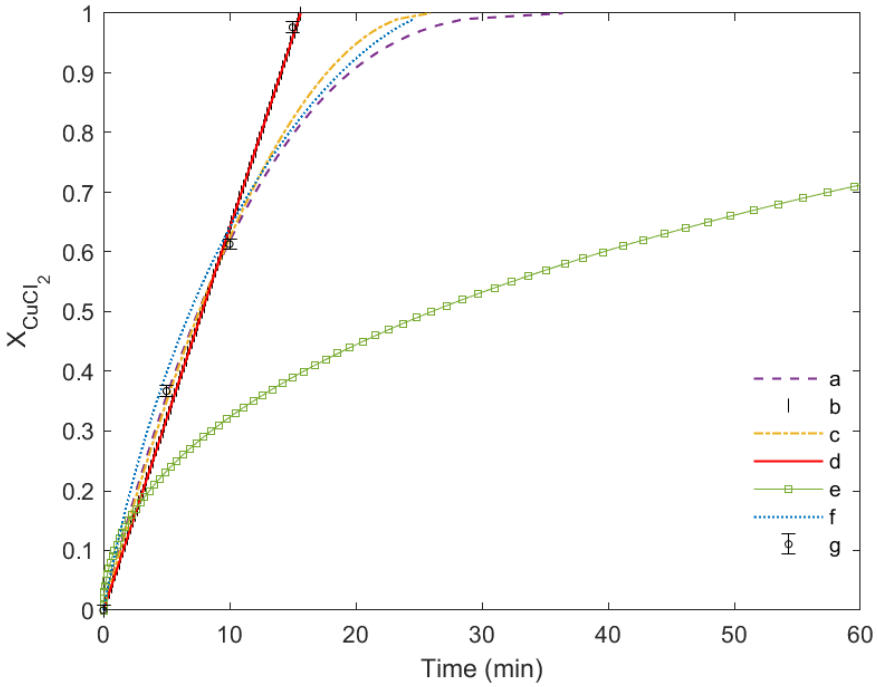

Figure 5-35: Crushed $CuCl_2$ conversion with time for Experiment 7 at 400°C and 27 µm particle size. (a) Reaction control-spherical, (b) Gas film diffusion-spherical, (c) Reaction control-cylindrical, (d) Gas film diffusion-cylindrical, (e) Product layer diffusion-cylindrical, (f) Combined control-cylindrical, and (g) Experimental data

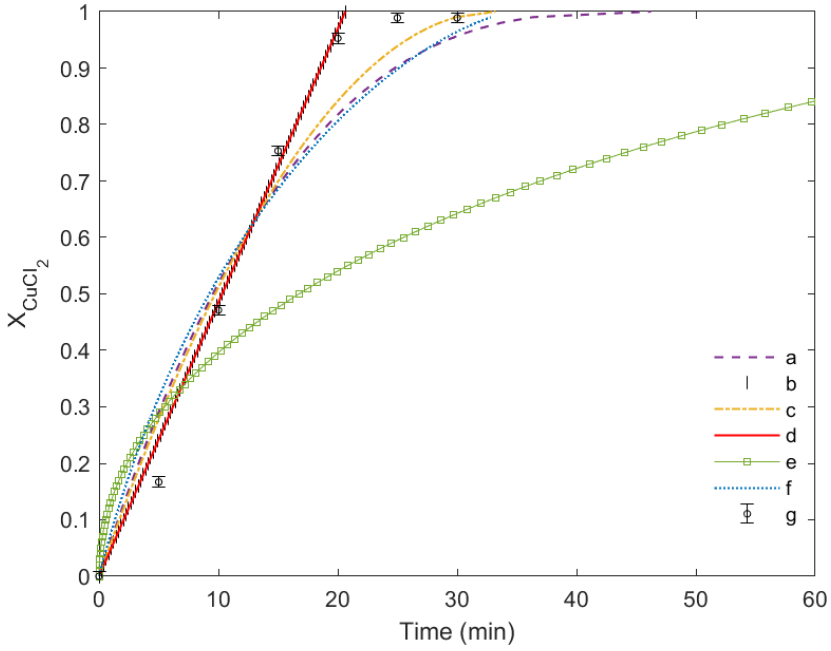

Figure 5-36: Crystallised $CuCl_2$ conversion with time for Experiment 8 at 400°C and 615 µm particle size, (a) Reaction control-spherical, (b) Gas film diffusion-spherical, (c) Reaction control-cylindrical, (d) Gas film diffusion-cylindrical, (e) Product layer diffusion-cylindrical, (f) Combined control-cylindrical, and (g) Experimental data

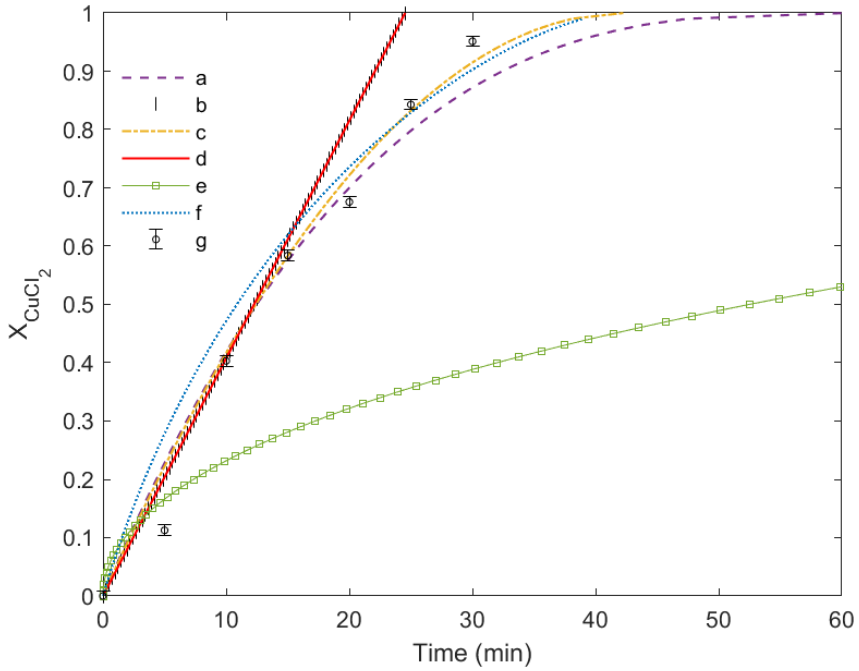

Figure 5-37: Crystallised $CuCl_2$ conversion with time for Experiment 9 at 400°C and 615 µm particle size, (a) Reaction control-spherical, (b) Gas film diffusion-spherical, (c) Reaction control-cylindrical, (d) Gas film diffusion-cylindrical, (e) Product layer diffusion-cylindrical, (f) Combined control-cylindrical, and (g) Experimental data

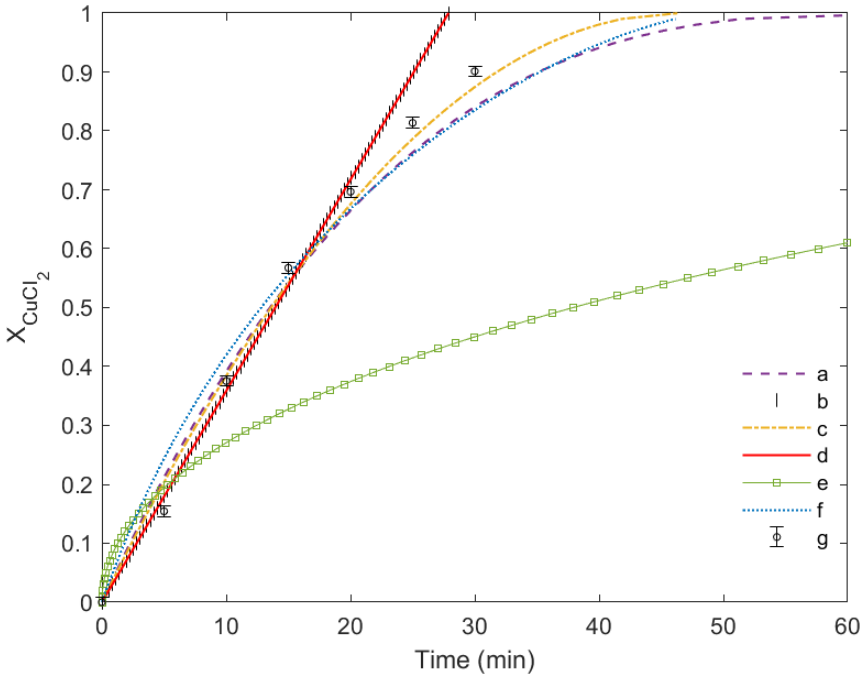

Figure 5-38: Crystallised $CuCl_2$ conversion with time for Experiment 10 at 400°C and 1100 µm particle size, (a) Reaction control-spherical, (b) Gas film diffusion-spherical, (c) Reaction control-cylindrical, (d) Gas film diffusion-cylindrical, (e) Product layer diffusion-cylindrical, (f) Combined control-cylindrical, and (g) Experimental data

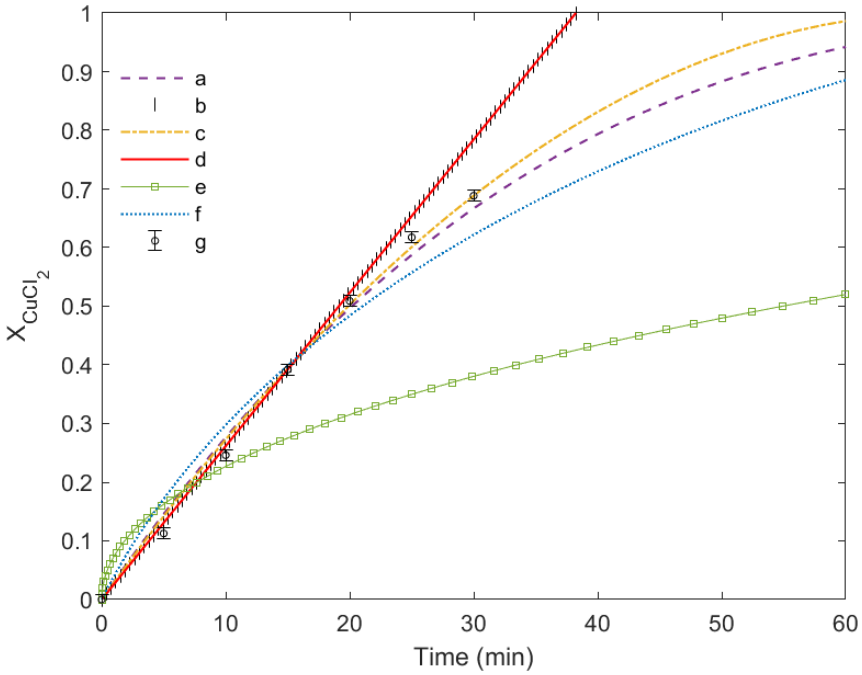

Figure 5-39: Dried $CuCl_2$ conversion with time for Experiment 11 at 370°C and 95 µm particle size, (a) Reaction control-spherical, (b) Gas film diffusion-spherical, (c) Reaction control-cylindrical, (d) Gas film diffusion-cylindrical, (e) Product layer diffusion-cylindrical, (f) Combined control-cylindrical, and (g) Experimental data

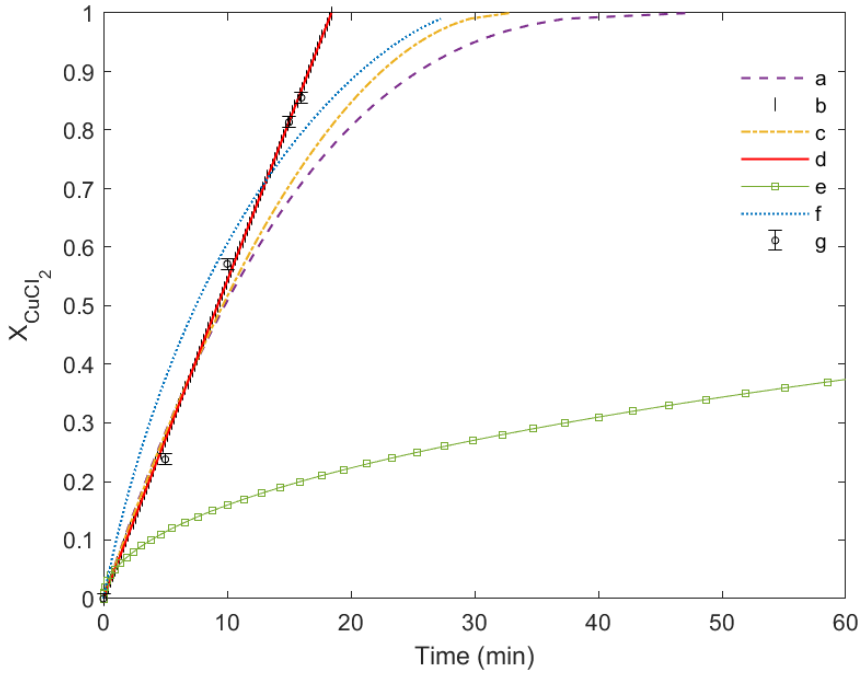

Figure 5-40: Crushed $CuCl_2$ conversion with time for Experiment 12 at 370°C and 27 µm particle size, (a) Reaction control-spherical, (b) Gas film diffusion-spherical, (c) Reaction control-cylindrical, (d) Gas film diffusion-cylindrical, (e) Product layer diffusion-cylindrical, (f) Combined control-cylindrical, and (g) Experimental data

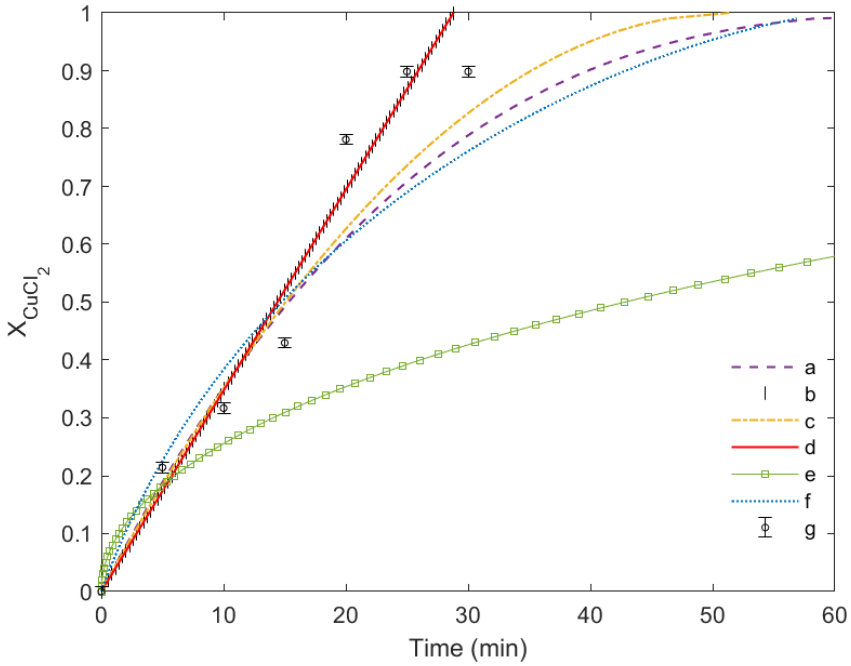

Figure 5-41: Crystallised $CuCl_2$ conversion with time for Experiment 13 at 370℃ and 615 µm particle size, (a) Reaction control-spherical, (b) Gas film diffusion-spherical, (c) Reaction control-cylindrical, (d) Gas film diffusion-cylindrical, (e) Product layer diffusion-cylindrical, (f) Combined control-cylindrical, and (g) Experimental data

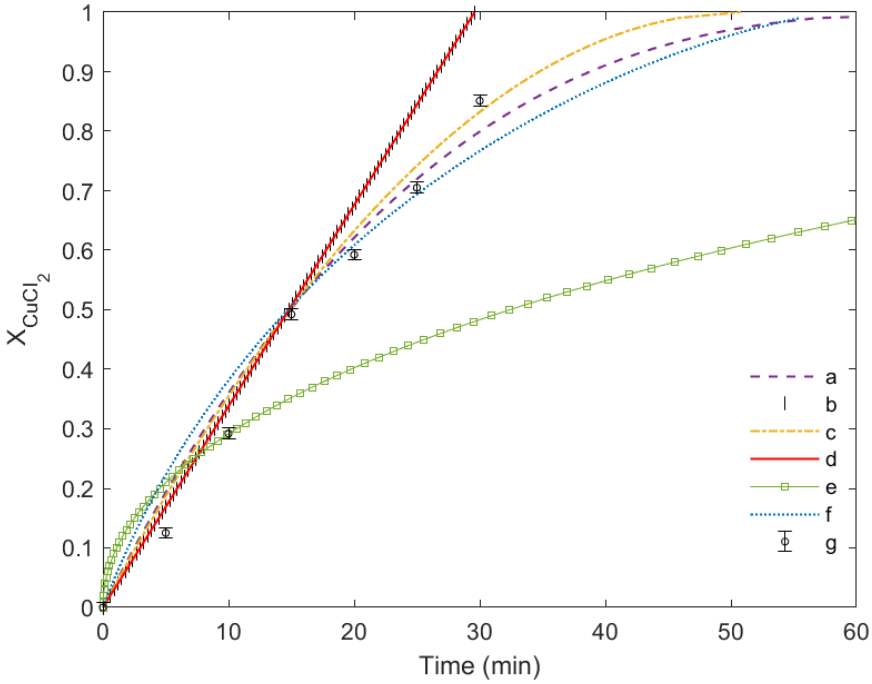

Figure 5-42: Crystallised $CuCl_2$ conversion with time for Experiment 14 at 370℃ and 615 µm particle size, (a) Reaction control-spherical, (b) Gas film diffusion-spherical, (c) Reaction control-cylindrical, (d) Gas film diffusion-cylindrical, (e) Product layer diffusion-cylindrical, (f) Combined control-cylindrical, and (g) Experimental data

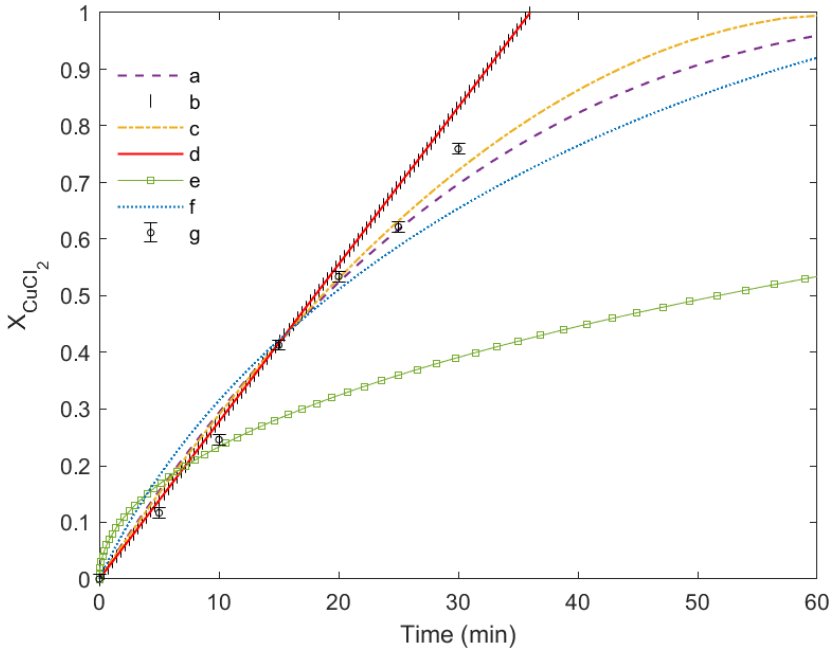

Figure 5-43: Crystallised $CuCl_2$ conversion with time for Experiment 15 at 370°C and 1100 µm particle size, (a) Reaction control-spherical, (b) Gas film diffusion-spherical, (c) Reaction control-cylindrical, (d) Gas film diffusion-cylindrical, (e) Product layer diffusion-cylindrical, (f) Combined control-cylindrical, and (g) Experimental data

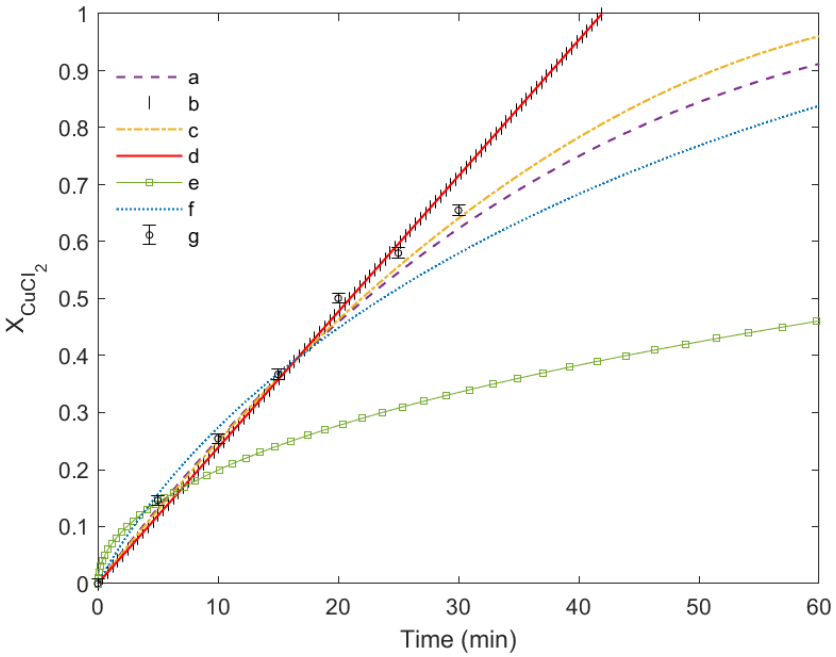

Figure 5-44: Dried $CuCl_2$ conversion with time for Experiment 16 at 350°C and 95 µm particle size. (a) Reaction control-spherical, (b) Gas film diffusion-spherical, (c) Reaction control-cylindrical, (d) Gas film diffusion-cylindrical, (e) Product layer diffusion-cylindrical, (f) Combined control-cylindrical, and (g) Experimental data

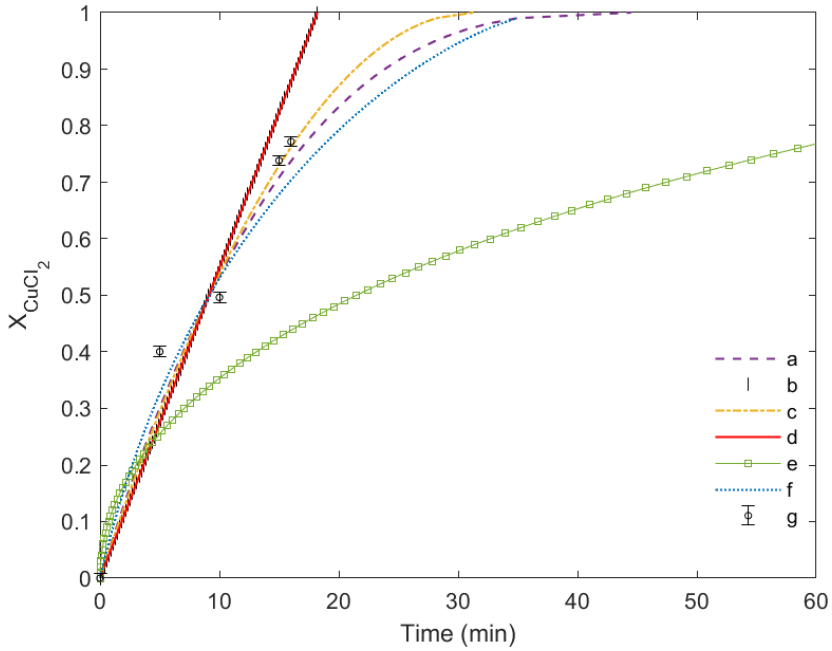

Figure 5-45: Crushed $CuCl_2$ conversion with time for Experiment 17 at 350°C and 27 µm particle size, (a) Reaction control-spherical, (b) Gas film diffusion-spherical, (c) Reaction control-cylindrical, (d) Gas film diffusion-cylindrical, (e) Product layer diffusion-cylindrical, (f) Combined control-cylindrical, and (g) Experimental data

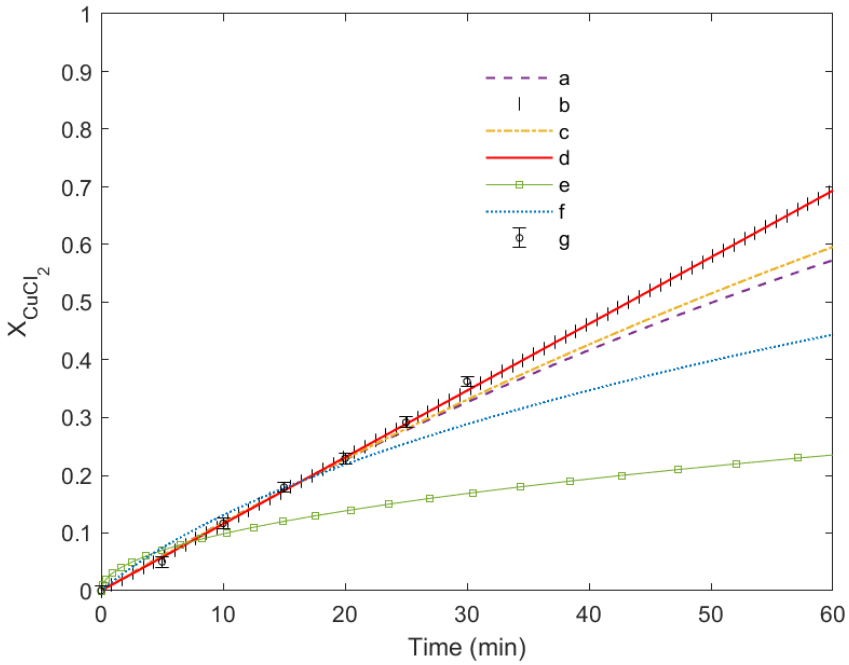

Figure 5-46: Dried $CuCl_2$ conversion with time for Experiment 18 at 390°C and 95 µm particle size, S/Cu= 5, (a) Reaction control-spherical, (b) Gas film diffusion-spherical, (c) Reaction control-cylindrical, (d) Gas film diffusion-cylindrical, (e) Product layer diffusion-cylindrical, (f) Combined control-cylindrical, and (g) Experimental data

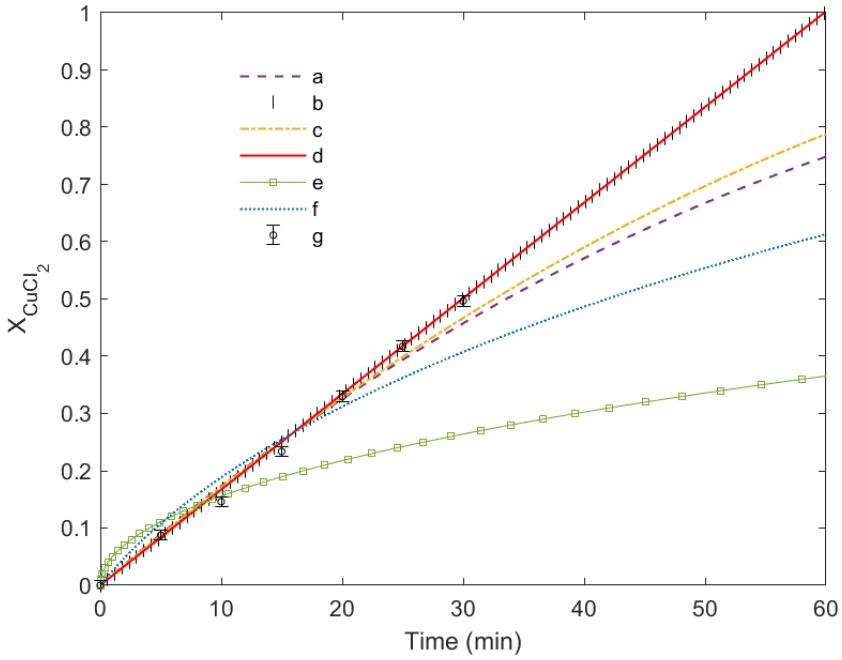

Figure 5-47: Crystallised $CuCl_2$ conversion with time for Experiment 19 at 390°C and 230 µm particle size, S/Cu= 5, (a) Reaction control-spherical, (b) Gas film diffusion-spherical, (c) Reaction control-cylindrical, (d) Gas film diffusion-cylindrical, (e) Product layer diffusion-cylindrical, (f) Combined control-cylindrical, and (g) Experimental data

5.3.2 SCM Particle Size Effect

Based on the findings of the previous section, the SCM with the cylindrical shape assumption was identified as the most accurate model. Consequently, it was employed to examine further the influence of particle size on the hydrolysis reaction. The product layer diffusion, reaction and gas film diffusion control models at 390°C are plotted in Figure 5-48 toFigure 5-50 for the crystallised materials with particle sizes of 230 µm, 615 µm, and 1100 µm to compare the models with the experimental data. All particle sizes of the crystallised material present a similarity between the gas film diffusion control and the reaction control up to 60% of the particle conversion. Beyond that time, the crystallised material with a particle size of 230 µm starts to follow the gas diffusion model while the 615 µm and 1100 µm follow reaction control model.

Data is compared to the different rate controlling models in Figure 5-51. The particle size of 230 µm and 615 µm showed a similar curve up to 60% conversion. However the time for full conversion was 27 min for the 230 um particle and 44 min for the 615 µm. As for the 1100 µm particle size has the lowest rate as the model predicted to achieve complete conversion after 52 min. The dominance of gas film control for the smallest particle size may be attributed to the higher reaction rate, resulting in gas film diffusion being the slowest step and consequently the controlling step. given the surface reaction controls between 230 - 615 µm, it appears that decreasing the particle size below 230 µm is not required and could be as high as 615 µm for crystallised particles. This could have implications in costs associated with pretreatment (e.g. size reduction).

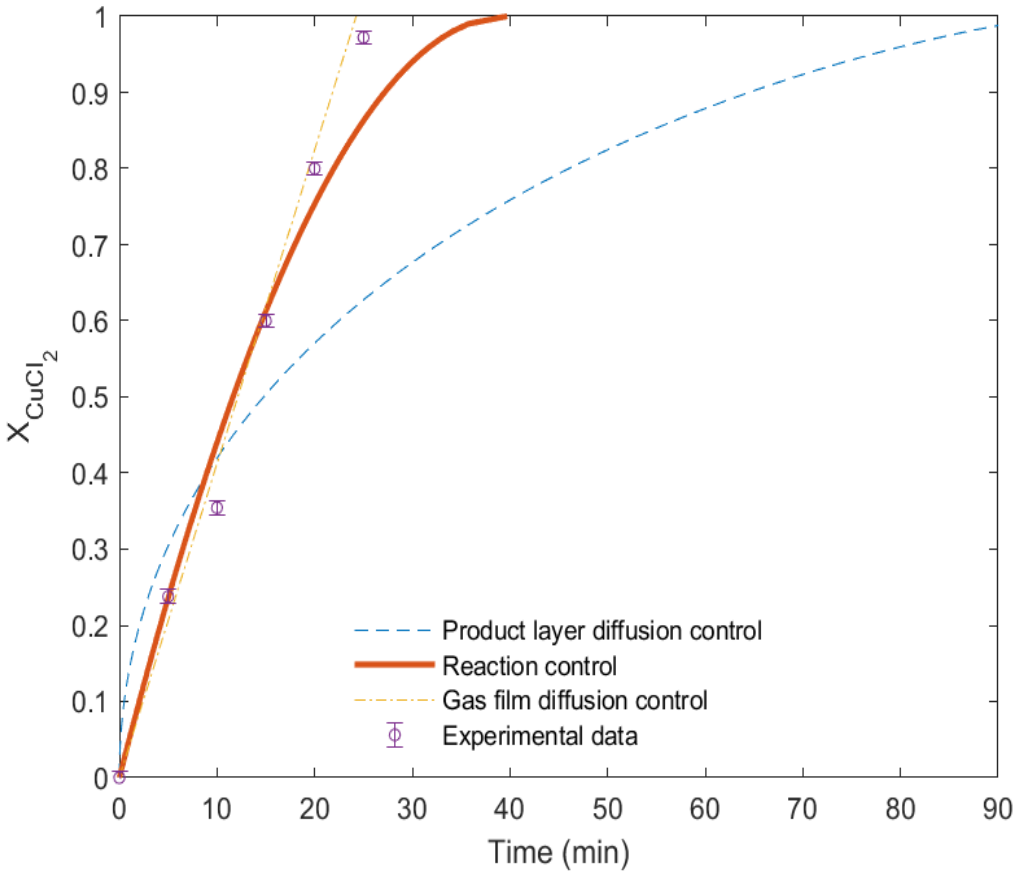

Figure 5-48: SCM for 230 µm crystallised $CuCl_2$ at 10 S/Cu ratio and 390°C

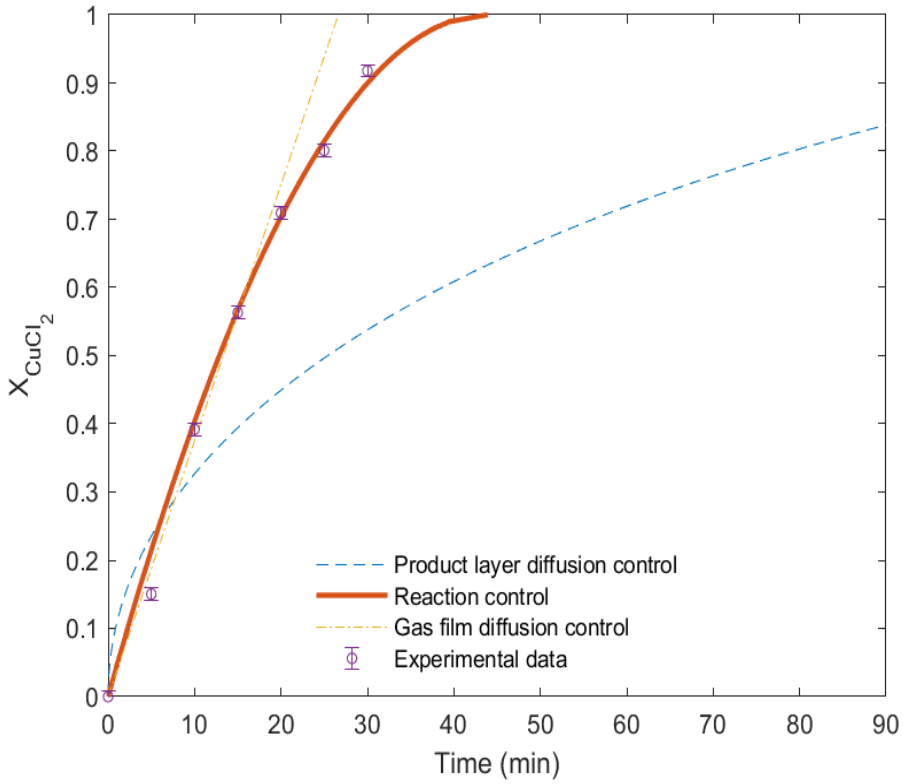

Figure 5-49: SCM for 615 µm crystallised $CuCl_2$ at 10 S/Cu ratio and 390°C

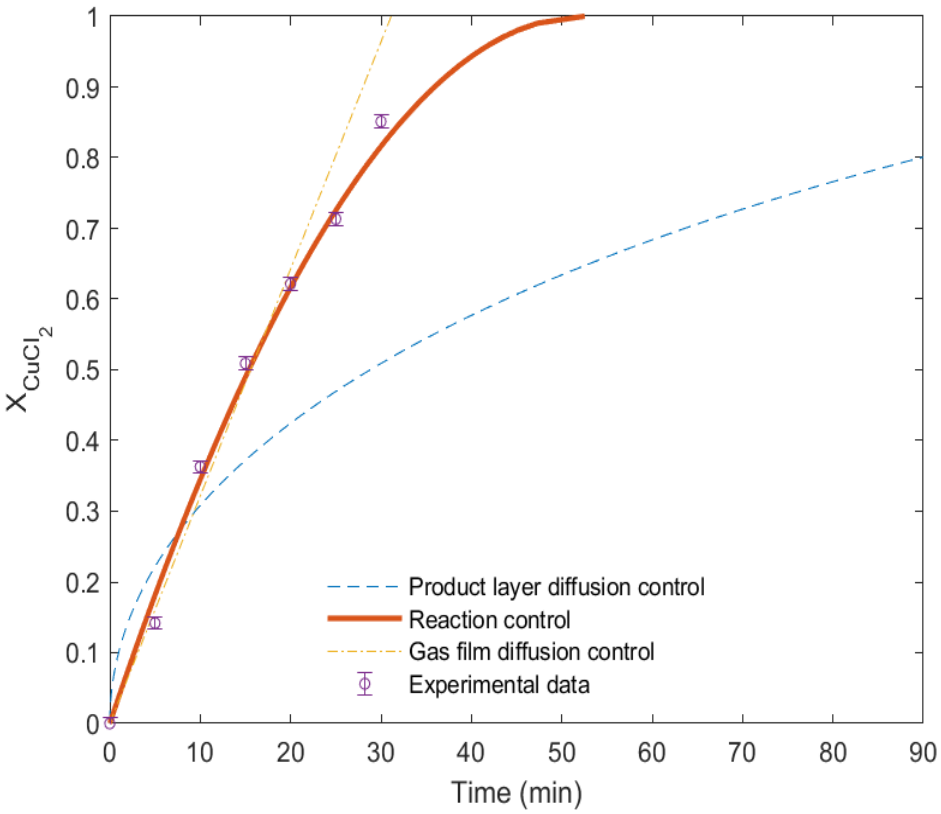

Figure 5-50: SCM for 1100 µm crystallised $CuCl_2$ at 10 S/Cu ratio and 390°C

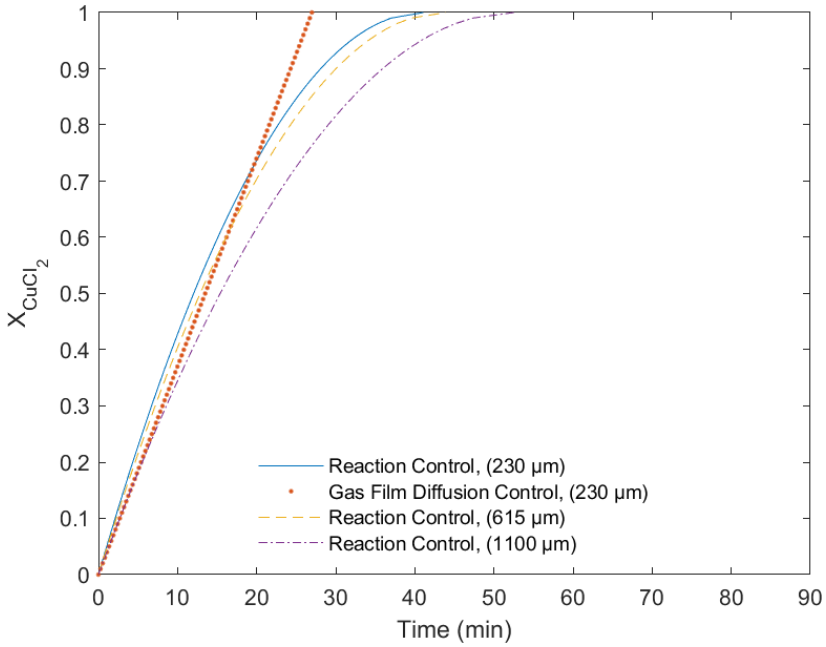

Figure 5-51: SCM for hydrolysis reaction with cylindrical assumption for crystallised samples with different particle sizes at 10 S/Cu ratio and 390°C.

5.3.3 SCM Steam to Copper Ratio Effect

In section 5.2.3, the impact of the S/Cu ratio on conversion rate was examined using experimental data for dried (95 µm) and crystallised (230 µm) materials at ratios of 10 and 5. This section explores the SCM to examine the impact of the S/Cu ratio on the controlling step and model prediction. It also investigates whether the controlling step will change when similar samples are reacted at different S/Cu ratios. The selected models in this section are based on the results from section 5.3.1, where the controlling step was determined for Experiments 1, 3, 18, and 19.

In Figure 5-52, two samples with a particle size of 95 µm were subjected to reactions at a temperature of 390°C, maintaining consistent operating parameters except for the S/Cu ratio. One sample underwent the reaction at an S/Cu ratio of 10, while the other reacted under an S/Cu ratio of 5. The results indicated that a higher ratio led to a reaction controlling step. Conversely, a lower ratio shifted the control to film diffusion controlling step, resulting in slower gas molecule diffusion to reach the particle reaction surface. Similarly, this investigation was extended to crystallised

samples with a particle size of 230 µm. At a S/Cu ratio of 10, the reaction was under gas film control, and this control persisted even after reducing the ratio to 5 . However, the notable difference between the two slopes indicates the impact of reducing the ratio and significantly decreasing the conversion rate. The figure suggests that the high conversion achieved at a higher S/Cu ratio could be attained at a lower ratio if the reaction time was extended. This possibility requires further investigation in future studies.

The models can provide a good estimation for the reaction rate under a lower S/Cu ratio, leading to a lower process cost. However, the results indicated a lower conversion rate at a lower ratio, suggesting the need to compromise the cost to achieve the required conversion. It also highlights the possibility of controlling step shifting during modelling with SCM. Assuming that the controlling step will remain the same under different S/Cu ratios might lead to inaccurate modelling for the reaction; this issue was not previously stated in the literature for the hydrolysis reaction in the Cu-Cl cycle.

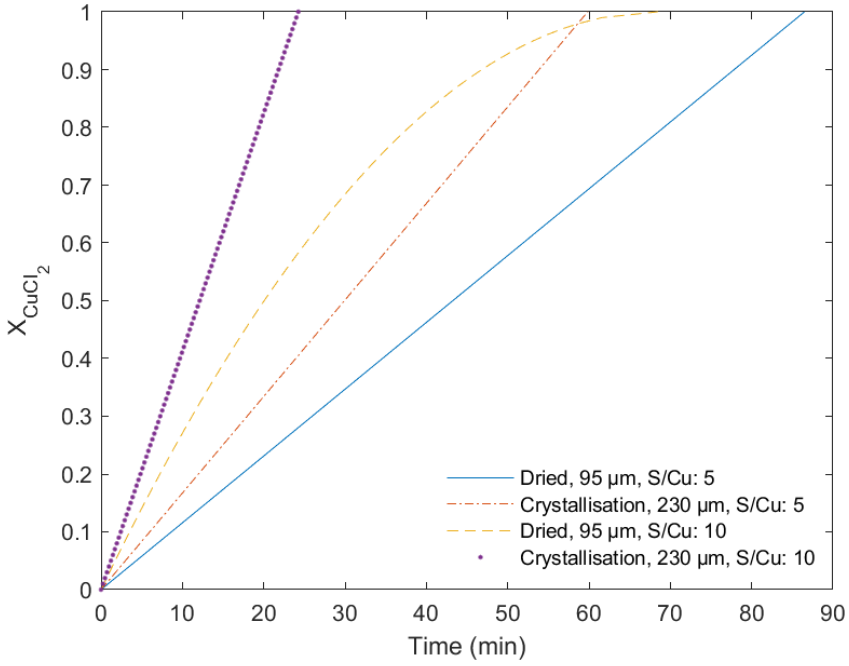

Figure 5-52: The effect of different S/Cu ratios at the SCM for hydrolysis reaction at 390°C

5.3.4 Activation Energy and Surface Area

After determining the controlling step and the best-fit model and obtaining the constants (surface reaction constant and gas film constant) corresponding to the best-fit model in previous sections, the constants of each particle size at three different temperatures were correlated to find the constants as a function of temperature and thereby determine the corresponding activation energy. The Arrhenius correlation was linearized to determine the activation energy for each particle size. The activation energy for the reaction constant is presented for the dried and crystallised samples with particle sizes of 615 μm and 1100 μm. Similarly, the activation energy for gas diffusion (diffusivity) was determined for the crushed and crystallised samples with particle sizes of 213 μm. The data for each particle size are fitted and presented in Figure 5-53. The fitting correlations are listed from Equations (5-1) to (5-5), along with the R-squared values (coefficient of determination). All correlations exhibited an acceptable regression factor, except for the dried sample with a particle size of 95 μm, which was attributed to the close values of the reaction constant at 390°C and 370°C.

The activation energy derived from the Arrhenius equation may clarify some of the changes in the reaction behaviour for the crystallised material. The activation energy of the reaction, as expressed in Equations (5-1), (5-4), and (5-5), indicates that the crystallised material has a lower activation energy, explaining the higher rate of reaction in most cases. Regarding the activation energy of gas film diffusion, as indicated in Equations (5-2) and (5-3), the values are close, not indicating a difference in the reaction rate between the crushed and crystallised material. The correlations can be used to estimate the constants at different operating temperatures, thereby leading to improved modelling and predictions of the processes. Extending these values to cover a broader range of different particle sizes is a useful contribution to the literature.

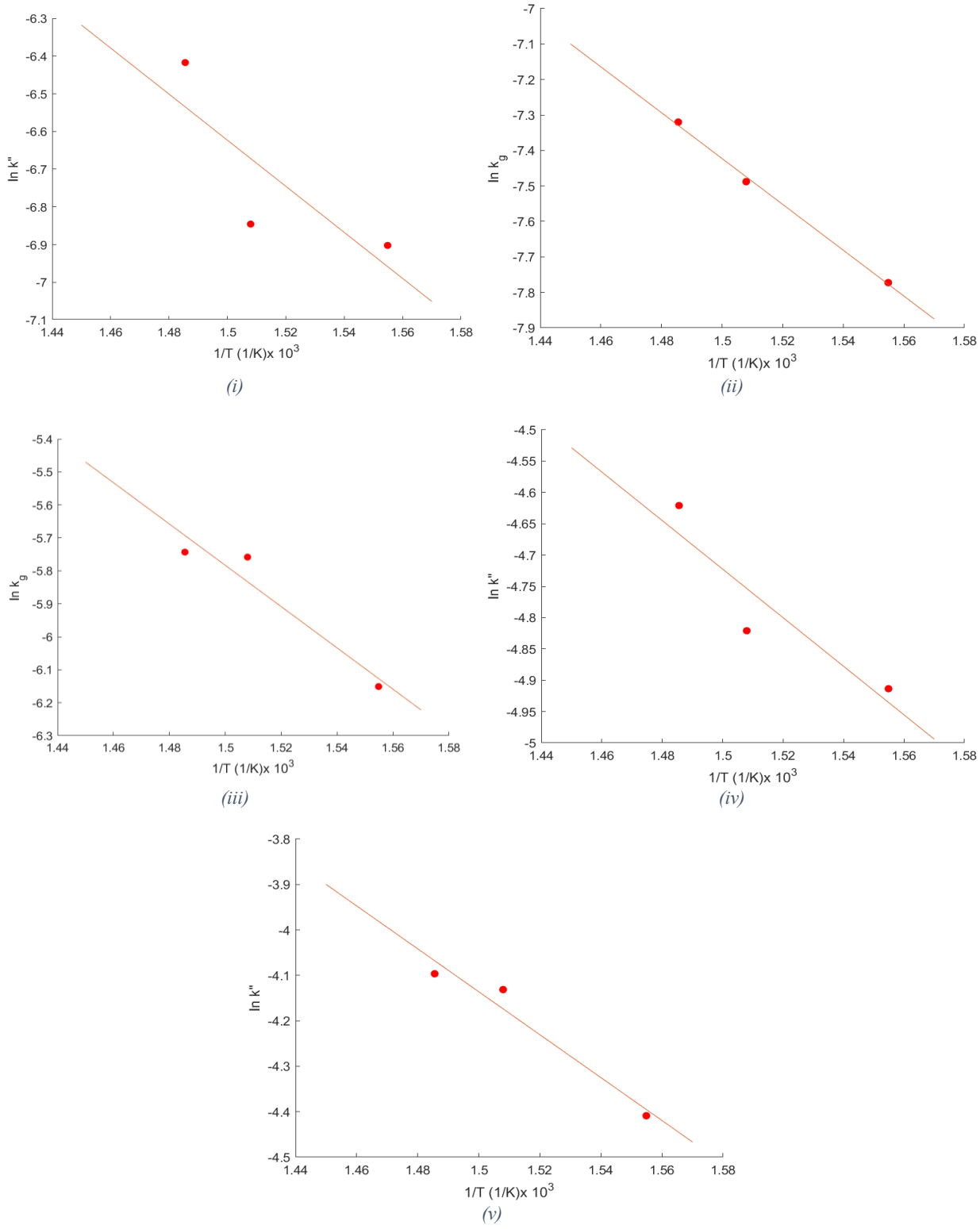

Figure 5-53: k'' and k_g as Function of Temperatures. Dried Reactant of 95 µm Particle Size. (i) Dried $CuCl_2$ (95 µm), (ii) Crushed $CuCl_2$ (27 µm), (iii) Crystallised $CuCl_2$ (230 µm), (iv) Crystallised $CuCl_2$ (615 µm), (v) Crystallised $CuCl_2$ (1100 µm)

$$k'' = 12.74 \exp\left(\frac{-51}{R''T}\right) \quad , R^2 = 0.66 \quad \{\text{for Dried } CuCl_2, 95\ \mu m\} \quad (5\text{-}1)$$

$$k_g = 9.66 \exp\left(\frac{-54}{R''T}\right) \quad , R^2 = 0.99 \quad \{\text{for Dried and Crushed } CuCl_2, 27\ \mu m\} \quad (5\text{-}2)$$

$$k_g = 37.16 \exp\left(\frac{-52}{R''T}\right) \quad , R^2 = 0.92 \quad \{\text{for Crystallised } CuCl_2, 230\ \mu m\} \quad (5\text{-}3)$$

$$k'' = 2.99 \exp\left(\frac{-32}{R''T}\right) \quad , R^2 = 0.84 \quad \{\text{for Crystallised } CuCl_2, 615\ \mu m\} \quad (5\text{-}4)$$

$$k'' = 19.13 \exp\left(\frac{-39}{R''T}\right) \quad , R^2 = 0.95 \quad \{\text{for Crystallised } CuCl_2, 1100\ \mu m\} \quad (5\text{-}5)$$

Consequently, additional factors not incorporated in the model and overlooked were examined for their potential to provide further insights. Specifically, the BET surface area and the BJH adsorption average pore width were explored as possible indicators of the porosity and surface characteristics of the material. The results in Table 5-5 revealed that the dried material exhibited the highest surface area, followed by the crushed material, while the crystallised material had the lowest surface area. Regarding pore size, the dried material demonstrated the highest pore volume and the smallest average pore width, suggesting smaller pores than the crushed and crystallised samples. In contrast, the crushed material displayed a moderate surface area and larger pore width, while the crystallised material had the lowest surface area and relatively larger pore width than the other samples.

A larger surface area provides more available surface for a reaction, facilitating increased interaction between reactants and the reaction surface, potentially accelerating the reaction rate. Conversely, smaller pores may restrict the accessibility of reactants to the reaction surface within the material, potentially slowing down the reaction rate due to reduced contact between the reactants and the reaction surface. Additionally, pore size can affect the diffusion rate of reactants and products within the material, with smaller pores potentially hindering the movement of

molecules, resulting in slower diffusion and potentially impacting the overall reaction rate. The specific nature of the reaction and the materials' characteristics will determine how these factors affect the reaction rate. This can account for the lower reaction rate of the dried material compared to the crushed and crystallised samples despite possessing the highest surface area.

When comparing the crushed and crystallised samples, the higher surface area and slightly smaller width of the crushed material compared to the crystallised one can explain the faster reaction of the crushed sample. It is essential to consider particle size in this comparison, even though it does not directly correlate with BET or BJH, as particle size refers to the physical dimensions of individual particles. At the same time, surface area and pore width are properties related to the material's internal structure. However, smaller particles may sometimes exhibit higher surface areas due to their increased surface-to-volume ratio. The crushed material has a higher surface area and significantly smaller volume than the crystallised material, leading to a considerably higher surface-to-volume ratio.

Table 5-5: $CuCl_2$ Surface Area and Pore Size

Sample	Dried	Dried and Crushed	Crystallised
Particle Size, μm	95	27	615
BET Surface Area, m^2/g	9.7506	6.6245	2.5017
Total Pore Volume of Pores, cm^3/g	0.001649	0.001085	0.000303
BJH Adsorption Average Pore Width (4V/A), Å	45.928	127.418	131.665

5.3.5 The Fractions of Crystallised Material

In large-scale industrial operations, various types of reactors are utilised, each with its own set of limitations, particularly in terms of reaction time and particle-gas contact time, especially in continuous operation units such as fluidized bed, falling particle reactor, or the recently proposed moving bed reactor by Broders et al. [78]. Given the available data on the distribution of crystallised material particles presented in section 5.1 and the associated conversion at different

time intervals for each particle size presented in section 5.2, the conversion utilised in the SCM can be adjusted using the particle fraction of each size. By expanding Equation (4-36) to derive Equation (5-6) and assuming a reaction time of 25 minutes, the conversion of each particle size at 25 minutes can be substituted into the equation for each temperature. This process can be repeated for each temperature, and the average conversion of the crystallised sample after 25 minutes can be summarized in Table 5-6. The decrease in conversion underscores the significance of this analysis.

Assuming that the material will convert based on the conversion of the particles with a size of 230 µm, as they constitute 75% of the particle size in the crystallised material (refer to Table 5-2), a complete conversion of 99% will be achieved at 400°C after 25 minutes. However, if the entire particle size distribution is considered, the final conversion of the crystallised sample under the same conditions will be 96%, representing a 3% difference. This difference increases with decreasing temperature, reaching 4% at 390°C and 5% at 370°C, which is deemed significant for the accuracy of conversion prediction.

$$1-\bar{X}_{\mathrm{B}}=[1-X_{\mathrm{B}}(230\mu\mathrm{m})]\frac{F(230\mu\mathrm{m})}{F}+[1-X_{\mathrm{B}}(615\mu\mathrm{m})]\frac{F(615\mu\mathrm{m})}{F}+[1-X_{\mathrm{B}}(1100\mu\mathrm{m})]\frac{F(1100\mu\mathrm{m})}{F} \tag{5-6}$$

Table 5-6: Average Particle Conversion for Crystallised $CuCl_2$

Reaction Temperature °C	$\bar{X}_{\mathrm{B}}$
370	85%
390	93%
400	96%

Finally, it is essential to consider how the preceding findings can be applied to enhance the cycle improvement. The low energy requirement for implementing crystallisation as a unit

operation in the cycle and the higher conversion achieved by the crystallised material provide an advantage when selecting the unit operations in the cycle. If crystallisation is not chosen, adding a size reduction unit would offer several benefits, such as reducing reaction time and increasing reaction rate. Regarding the SCM, adopting a cylindrical assumption improved the model's predictive capabilities. Furthermore, a better understanding of the controlling step can guide the direction of reaction improvement. For instance, when gas film diffusion is controlling, the interaction between the gas and solid reactant needs to be enhanced to achieve better reaction results, and the type of selected reactor can facilitate this interaction. For example, a fluidized bed will achieve a better gas film interface than a fixed bed. Meanwhile, improvement can be attained for materials controlled by the reaction step by altering parameters such as reaction temperature, particle size, and S/Cu ratio, or in this case, the pre-processing of the raw material, such as crystallisation and crushing.

Chapter 6 Conclusions and Recommendations

6.1 Conclusions

The investigation into the kinetics of the hydrolysis reaction has been instrumental for providing new insights on various methods of pre-processing of the solid reactant with different particle sizes. This study is essential for understanding the reaction rate and mechanism, as well as for optimizing the production process. The investigation demonstrated that the $CuCl_2$ crystal morphology typically displays a uniform size distribution in the form of elongated sticks resembling a cylindrical shape. The estimated cylindrical shape ranged from 200 to 650 μm in length and 70 to 200 μm in diameter. After crushing, subsequent imaging of the material revealed particles ranging from 30 to 150 μm in length and 20 to 70 μm in diameter. Smaller particles, less than 30 μm, exhibited a spherical shape, particularly those less than 10 μm. Following crystallisation, agglomerated particles forming irregular flakes with non-uniform sizes were observed. It was noted that crystallisation increased particle size compared to the original commercial samples, revealing that 75% of the sample had an average particle diameter of 230 μm. The XRD pattern was also examined for the dried and crystallised material, showing a similar pattern for $CuCl_2$, except for the absence of the plain 001 and 111 peaks after crystallisation.

Five samples of $CuCl_2$ were investigated, including dried and crushed samples and three different particle sizes for the crystallised sample. Each sample was reacted with steam at three different temperatures. All samples revealed that the conversion increases with an increase in temperature. The dried sample achieved the lowest rate of conversion, while the crushed sample achieved the highest rate of conversion. The crystallised materials achieved a rate of conversion higher than the dried material and lower than the crushed material. When comparing the three

different particle sizes of the crystallised material (crystallised 230 μm, crystallised 615 μm, and crystallised 1100 μm), the rate of conversion increased as the particle size decreased.

A model was developed based on spherical and cylindrical particle shape assumptions, with four equations for each shape, and the models were compared with experimental data using the coefficient of determination (R-squared). Experiments at 390°C with different particles showed that the reaction control model exhibited the best fit for dried, crystallised 615 μm and crystallised 1100 μm materials. The crushed material and crystallised 95 μm indicated that the gas film diffusion controlled the conversion. Experiments at 400°C and 370°C exhibited similar trends in controlling steps. Dried and crystallised 95 μm with a reduced S/Cu ratio showed that gas film diffusion was the controlling step. XRD was utilised to analyse the solid product post-reaction, revealing the presence of the desired product Cu_2OCl_2 at temperatures ranging from 370 - 400°C. Conversely, the reaction at 350°C yielded the side product CuCl only.

The activation energy for the reaction constant was determined to be 51 kJ/mol for the dried sample and 32 - 39 kJ/mol for the crystallised sample, with 615 μm and 1100 μm particle sizes. Similarly, the activation energy for gas diffusion (diffusivity) fell within the 52 - 54 kJ/mol range for the crushed and crystallised samples with a particle size of 213 μm. The lower activation energy for the crystallised material explains the higher conversion and faster reaction progress in most cases. Meanwhile, values are closely aligned regarding the activation energy of gas film diffusion, indicating no discernible difference. The study emphasised the alterations in surface area and porosity due to variations in solid processing and the impact of crystallised particle size distribution on the conversion. All experiments were conducted at an S/Cu ratio of 10, except two experiments performed at 390°C and an S/Cu ratio of 5, resulting in low conversion rates. Specifically, the dried material of 95 μm achieved only 36% conversion, while the crystallised material of 230 μm achieved 50% conversion within 30 minutes.

The outcomes of this research can be leveraged to enhance the Cu-Cl cycle and its industrial applications, particularly in relation to crystallisation as a unit operation. This process offers benefits such as low energy requirements and higher conversion rates. Moreover, this study has been useful to better understand the reaction rate and related thermochemical processes.

6.2 Recommendations

Further investigation can be conducted to explore the conversion rate with an extended reaction time, mainly focusing on a low steam-to-copper ratio and the investigation of more comprehensive ranges of steam-to-copper ratios. This exploration is particularly relevant if the objective is to reduce steam consumption for cost-effectiveness. Additionally, consideration should be given to designing a reactor with a reflux stream to redirect the unreacted steam back to the reactor, thereby optimizing steam consumption. In this study, crystallisation was carried out at room temperature. Subsequent research could investigate crystallisation at 0°C to fully comprehend the influence of temperature on crystallisation and crystal growth. This comprehensive analysis should encompass the crystallisation rate and particle size and the potential impact on the hydrolysis reaction rate and conversion. It is also recommended that the analysis methods be enhanced in future studies to accurately record the yield of the intended product and identify any side reactions. This will contribute to a more thorough understanding of the overall process and its outcomes. Another suggestion to enhance the SCM prediction is incorporating porosity into model equations. This consideration can provide a more comprehensive and accurate representation of the solid conversion. Other research can consider using statistical Design of Experiments (DOEs) to better understand how different factors, such as temperature, time, and steam-to-copper ratio, affect hydrolysis reaction conversion.

References

[1] G. F. Naterer, I. Dincer, and C. Zamfirescu, *Hydrogen Production from Nuclear Energy*. London: Springer London, 2013. doi: 10.1007/978-1-4471-4938-5.

[2] IEA (2023), *Global Hydrogen Review 2023*, IEA, Paris. Accessed: Jan. 21, 2024. [Online]. Available: https://www.iea.org/reports/global-hydrogen-review-2023, Licence: CC BY 4.0

[3] Z. Wang, G. Naterer, and K. Gabriel, "Multiphase reactor scale-up for Cu–Cl thermochemical hydrogen production," *Int. J. Hydrog. Energy*, vol. 33, no. 23, pp. 6934–6946, Dec. 2008, doi: 10.1016/j.ijhydene.2008.08.050.

[4] L. Zhang, C. (Charles) Xu, and P. Champagne, "Overview of recent advances in thermo-chemical conversion of biomass," *Energy Convers. Manag.*, vol. 51, no. 5, pp. 969–982, May 2010, doi: 10.1016/j.enconman.2009.11.038.

[5] O. Levenspiel, *Chemical Reaction Engineering*, vol. 38. American Chemical Society, 1999. Accessed: Feb. 13, 2022. [Online]. Available: https://doi.org/10.1021/ie990488g

[6] Z. Wang *et al.*, "Towards integration of hydrolysis, decomposition and electrolysis processes of the Cu–Cl thermochemical water splitting cycle," *Int. J. Hydrog. Energy*, vol. 37, no. 21, pp. 16557–16569, Nov. 2012, doi: 10.1016/j.ijhydene.2012.02.172.

[7] O. A. Jianu, M. Lescisin, Z. Wang, M. A. Rosen, and G. F. Naterer, "X-ray diffraction of crystallization of copper (II) chloride for improved energy utilization in hydrogen production," *Int. J. Hydrog. Energy*, vol. 41, no. 19, pp. 7848–7853, May 2016, doi: 10.1016/j.ijhydene.2015.12.213.

[8] Y. Shindo, N. Ito, K. Haraya, T. Hakuta, and H. Yoshitome, "Thermal efficiency of the magnesium-iodine cycle for thermochemical hydrogen production," *Int. J. Hydrog. Energy*, vol. 8, no. 7, pp. 509–513, 1983, doi: 10.1016/0360-3199(83)90003-4.

[9] S. Kubo *et al.*, "A pilot test plan of the thermochemical water-splitting iodine–sulfur process," *Nucl. Eng. Des.*, vol. 233, no. 1–3, pp. 355–362, Oct. 2004, doi: 10.1016/j.nucengdes.2004.08.018.

[10] K. Knoche and P. Schuster, "Thermochemical production of hydrogen by a vanadium/chlorine cycle. Part 1: An energy and exergy analysis of the process," *Int. J. Hydrog. Energy*, vol. 9, no. 6, pp. 457–472, 1984, doi: 10.1016/0360-3199(84)90098-3.

[11] F. Lemont, "Promising optimization of the CeO2/CeCl3 cycle by reductive dissolution of cerium(IV) oxide," *Int. J. Hydrog. Energy*, vol. 33, no. 24, pp. 7355–7360, Dec. 2008, doi: 10.1016/j.ijhydene.2008.09.030.

[12] F. Safari and I. Dincer, "A study on the Fe–Cl thermochemical water splitting cycle for hydrogen production," *Int. J. Hydrog. Energy*, vol. 45, no. 38, pp. 18867–18875, Jul. 2020, doi: 10.1016/j.ijhydene.2020.04.208.

[13] C. Sattler, M. Roeb, C. Agrafiotis, and D. Thomey, “Solar hydrogen production via sulphur based thermochemical water-splitting,” *Sol. Energy*, vol. 156, pp. 30–47, Nov. 2017, doi: 10.1016/j.solener.2017.05.060.

[14] L. C. Brown et al., “High efficiency generation of hydrogen fuels using nuclear power.,” 2003. [Online]. Available: https://fusion.gat.com/pubs-ext/AnnSemiannETC/A24285.pdf.

[15] B. W. Mcquillan *et al.*, “High efficiency generation of hydrogen fuels using solar thermal-chemical splitting of water (Solar thermo-chemical splitting for H2),” 2010.

[16] A. Farsi, “Development and modeling of a lab-scale integrated copper-chlorine cycle for hydrogen production.,” University of Ontario Institute of Technology, Oshawa, Ontario, 2020. Accessed: Oct. 27, 2023. [Online]. Available: http://central.bac-lac.gc.ca/.redirect?app=damspub&id=ac718aa2-67f8-42af-ad9a-6df285d3fb80

[17] A. Farsi, I. Dincer, and G. F. Naterer, “Review and evaluation of clean hydrogen production by the copper–chlorine thermochemical cycle,” *J. Clean. Prod.*, vol. 276, p. 123833, Dec. 2020, doi: 10.1016/j.jclepro.2020.123833.

[18] A. Ozbilen, I. Dincer, and M. A. Rosen, “A comparative life cycle analysis of hydrogen production via thermochemical water splitting using a Cu–Cl cycle,” *Int. J. Hydrog. Energy*, vol. 36, no. 17, pp. 11321–11327, Aug. 2011, doi: 10.1016/j.ijhydene.2010.12.035.

[19] G. F. Naterer, O. Jaber and I. Dincer, “Environmental Impact Comparison of Steam Methane,” in *18th World Hydrogen Energy Conf.*, Germany, 2010.

[20] Z. Wang, G. F. Naterer, and K. S. Gabriel, ‘Thermal integration of SCWR nuclear and thermochemical hydrogen plants’, in *2nd Canada-China joint workshop on supercritical-water-cooled reactors (CCSC-2010), (p. 747Megabytes)*, Canadian Nuclear Society, 2010.

[21] A. Hajimiragha, M. W. Fowler, and C. A. Cañizares, “Hydrogen economy transition in Ontario – Canada considering the electricity grid constraints,” *Int. J. Hydrog. Energy*, vol. 34, no. 13, pp. 5275–5293, Jul. 2009, doi: 10.1016/j.ijhydene.2009.04.063.

[22] G. Naterer, “Second Law viability of upgrading waste heat for thermochemical hydrogen production,” *Int. J. Hydrog. Energy*, vol. 33, no. 21, pp. 6037–6045, Nov. 2008, doi: 10.1016/j.ijhydene.2008.08.010.

[23] C. Zamfirescu, G. F. Naterer, and I. Dincer, “Upgrading of Waste Heat for Combined Power and Hydrogen Production with Nuclear Reactors,” *J. Eng. Gas Turbines Power*, vol. 132, no. 10, p. 102911, Jul. 2010, doi: 10.1115/1.4000803.

[24] M. Granovskii, I. Dincer, M. A. Rosen, and I. Pioro, “Thermodynamic Analysis of the Use a Chemical Heat Pump to Link a Supercritical Water-Cooled Nuclear Reactor and a Thermochemical Water-Splitting Cycle for Hydrogen Production,” *J. Power Energy Syst.*, vol. 2, no. 2, pp. 756–767, 2008, doi: 10.1299/jpes.2.756.

[25] C. Zamfirescu, I. Dincer, and G. Naterer, "Performance evaluation of organic and titanium based working fluids for high-temperature heat pumps," *Thermochim. Acta*, vol. 496, no. 1–2, pp. 18–25, Dec. 2009, doi: 10.1016/j.tca.2009.06.021.

[26] P. Bahadorani, G. F. Naterer, and K. Gabriel, "Particle formation from slurry spray drying in Cu-Cl thermochemical hydrogen production," in *Hydrog. and fuel cells 2009 int. conf. and exhib.*, Jul. 2009.

[27] S. Ghandehariun, G. F. Naterer, M. A. Rosen, and Z. Wang, "Options for heat recovery from molten salt in thermochemical hydrogen production," in *The CSME 2010 forum*, Victoria, BC (Canada), Jul. 2010.

[28] M. Naidin *et al.*, "Thermal-Design Options for Pressure-Channel SCWRS With Cogeneration of Hydrogen," *J. Eng. Gas Turbines Power*, vol. 131, no. 1, p. 012901, Jan. 2009, doi: 10.1115/1.2983016.

[29] M. F. Orhan, İ. Dinçer, and M. A. Rosen, "Efficiency comparison of various design schemes for copper–chlorine (Cu–Cl) hydrogen production processes using Aspen Plus software," *Energy Convers. Manag.*, vol. 63, pp. 70–86, Nov. 2012, doi: 10.1016/j.enconman.2012.01.029.

[30] M. S. Ferrandon *et al.*, "Hydrogen production by the Cu–Cl thermochemical cycle: Investigation of the key step of hydrolysing CuCl2 to Cu2OCl2 and HCl using a spray reactor" *Int. J. Hydrog. Energy*, vol. 35, no. 3, pp. 992–1000, Feb. 2010, doi: 10.1016/j.ijhydene.2009.09.086.

[31] A. Farsi, Ö. Kayhan, C. Zamfirescu, I. Dincer, and G. F. Naterer, "Kinetic and hydrodynamic analyses of chemically reacting gas-particle flow in cupric chloride hydrolysis for the Cu-Cl cycle," *Int. J. Hydrog. Energy*, vol. 44, no. 49, pp. 26783–26793, Oct. 2019, doi: 10.1016/j.ijhydene.2019.08.142.

[32] V. N. Daggupati, G. F. Naterer, K. S. Gabriel, R. J. Gravelsins, and Z. L. Wang, "Equilibrium conversion in Cu–Cl cycle multiphase processes of hydrogen production," *Thermochim. Acta*, vol. 496, no. 1–2, pp. 117–123, Dec. 2009, doi: 10.1016/j.tca.2009.07.009.

[33] A. Ozbilen, I. Dincer, and M. A. Rosen, "Environmental evaluation of hydrogen production via thermochemical water splitting using the Cu–Cl Cycle: A parametric study," *Int. J. Hydrog. Energy*, vol. 36, no. 16, pp. 9514–9528, Aug. 2011, doi: 10.1016/j.ijhydene.2011.05.067.

[34] A. Ozbilen, I. Dincer, and M. A. Rosen, "Life cycle assessment of hydrogen production via thermochemical water splitting using multi-step Cu–Cl cycles," *J. Clean. Prod.*, vol. 33, pp. 202–216, Sep. 2012, doi: 10.1016/j.jclepro.2012.03.035.

[35] R. V. Singh *et al.*, "Investigations on the hydrolysis step of copper-chlorine thermochemical cycle for hydrogen production," *Int. J. Energy Res.*, vol. 44, no. 4, pp. 2845–2863, 2020, doi: 10.1002/er.5101.

[36] K. Pope, Z. Wang, and G. F. Naterer, “Process integration of material flows of copper chlorides in the thermochemical Cu–Cl cycle,” *Chem. Eng. Res. Des.*, vol. 109, pp. 273–281, May 2016, doi: 10.1016/j.cherd.2015.12.024.

[37] M. S. Ferrandon, M. A. Lewis, F. Alvarez, and E. Shafirovich, “Hydrolysis of CuCl2 in the Cu–Cl thermochemical cycle for hydrogen production: Experimental studies using a spray reactor with an ultrasonic atomizer” *Int. J. Hydrog. Energy*, vol. 35, no. 5, pp. 1895–1904, Mar. 2010, doi: 10.1016/j.ijhydene.2009.12.034.

[38] M. Ferrandon, V. Daggupati, Z. Wang, G. Naterer, and L. Trevani, “Using XANES to obtain mechanistic information for the hydrolysis of CuCl2 and the decomposition of Cu2OCl2 in the thermochemical Cu–Cl cycle for H2 production,” *J. Therm. Anal. Calorim.*, vol. 119, no. 2, pp. 975–982, Feb. 2015, doi: 10.1007/s10973-014-4240-2.

[39] Z. Wang, G. Marin, G. F. Naterer, and K. S. Gabriel, “Thermodynamics and kinetics of the thermal decomposition of cupric chloride in its hydrolysis reaction,” *J. Therm. Anal. Calorim.*, vol. 119, no. 2, pp. 815–823, Feb. 2015, doi: 10.1007/s10973-014-3929-6.

[40] D. Thomas, N. A. Baveja, K. T. Shenoy, and J. B. Joshi, “Experimental Study on the Mechanism and Kinetics of CuCl2 Hydrolysis Reaction of the Cu–Cl Thermochemical Cycle in a Fluidized Bed Reactor,” *Ind. Eng. Chem. Res.*, vol. 59, no. 26, pp. 12028–12037, Jul. 2020, doi: 10.1021/acs.iecr.0c01807.

[41] T. Kekesi, K. Mimura, and M. Isshiki, “Copper Extraction from Chloride Solutions by Evaporation and Reduction with Hydrogen,” *Mater. Trans. JIM*, vol. 36, no. 5, pp. 649–658, 1995, doi: 10.2320/matertrans1989.36.649.

[42] G. D. Marin, Z. Wang, G. F. Naterer, and K. Gabriel, “Byproducts and reaction pathways for integration of the Cu–Cl cycle of hydrogen production,” *Int. J. Hydrog. Energy*, vol. 36, no. 21, pp. 13414–13424, Oct. 2011, doi: 10.1016/j.ijhydene.2011.07.103.

[43] M. A. Lewis, M. S. Ferrandon, D. F. Tatterson, and P. Mathias, “Evaluation of alternative thermochemical cycles – Part III further development of the Cu–Cl cycle,” *Int. J. Hydrog. Energy*, vol. 34, no. 9, pp. 4136–4145, May 2009, doi: 10.1016/j.ijhydene.2008.09.025.

[44] K. Pope, V. N. Daggupati, G. F. Naterer, and K. S. Gabriel, “Experimental study of gaseous effluent and solid conversion in a fluidized bed hydrolysis reactor for hydrogen production,” *Int. J. Hydrog. Energy*, vol. 37, no. 21, pp. 16397–16401, Nov. 2012, doi: 10.1016/j.ijhydene.2012.01.142.

[45] V. N. Daggupati, G. F. Naterer, and K. S. Gabriel, “Diffusion of gaseous products through a particle surface layer in a fluidized bed reactor,” *Int. J. Heat Mass Transf.*, vol. 53, no. 11–12, pp. 2449–2458, May 2010, doi: 10.1016/j.ijheatmasstransfer.2010.01.039.

[46] Y. Haseli, I. Dincer, and G. F. Naterer, “Hydrodynamic gas–solid model of cupric chloride particles reacting with superheated steam for thermochemical hydrogen production,” *Chem. Eng. Sci.*, vol. 63, no. 18, pp. 4596–4604, Sep. 2008, doi: 10.1016/j.ces.2008.07.003.

[47] M. Ferrandon, M. Lewis, and D. Tatterson, 'Further Development of the Hydrolysis Reactors in the Cu-Cl Cycle', in *The 2008 Annual Meeting*, 2008.

[48] S. M. Abdel Basir, "Recovery of cupric chloride from spent copper etchant solutions: a mechanistic study," *Hydrometallurgy*, vol. 69, no. 1–3, pp. 135–143, Apr. 2003, doi: 10.1016/S0304-386X(02)00209-8.

[49] A. Myerson, *Handbook of Industrial Crystallization*, 2nd ed. Butterworth-Heinemann, 2002.

[50] J. Nývlt, *The Kinetics of Industrial Crystallization*. Elsevier, 1985.

[51] D. W. Green and R. H. Perry, *Perry's Chemical Engineers' Handbook, Eighth Edition*. McGraw Hill Professional, 2007.

[52] G. F. Naterer *et al.*, "Canada's program on nuclear hydrogen production and the thermochemical Cu–Cl cycle," *Int. J. Hydrog. Energy*, vol. 35, no. 20, pp. 10905–10926, Oct. 2010, doi: 10.1016/j.ijhydene.2010.07.087.

[53] J. Shen and J. M. Smith, "Diffusional Effects in Gas-Solid Reactions," *Ind. Eng. Chem. Fundam.*, vol. 4, no. 3, pp. 293–301, Aug. 1965, doi: 10.1021/i160015a010.

[54] X. Li *et al.*, "A modified shrinking core model for the reaction between acid and hetero-granular rough mineral particles," *Hydrometallurgy*, vol. 153, pp. 114–120, Mar. 2015, doi: 10.1016/j.hydromet.2015.03.001.

[55] X. Liu, F. Song, and Z. Wen, "A novel dimensionless form of unreacted shrinking core model for solid conversion during chemical looping combustion," *Fuel*, vol. 129, pp. 231–237, Aug. 2014, doi: 10.1016/j.fuel.2014.04.006.

[56] C. Saha and S. Bhattacharya, "Determination and Comparison of CuO Reduction/Oxidation Kinetics in CLC Experiments with CO/Air by the Shrinking Core Model and Its Characterization," *Energy Fuels*, vol. 28, no. 5, pp. 3495–3510, May 2014, doi: 10.1021/ef500306e.

[57] R. O. Ajemba and O. D. Onukwuli, "Application of the shrinking core model to the analysis of alumina leaching from Ukpor clay using nitric acid," *Int. J. Eng.*, vol. 1, no. 3, pp. 1–13, 2012.

[58] A. Amiri, G. D. Ingram, A. V. Bekker, I. Livk, and N. E. Maynard, "A multi-stage, multi-reaction shrinking core model for self-inhibiting gas–solid reactions," *Adv. Powder Technol.*, vol. 24, no. 4, pp. 728–736, Jul. 2013, doi: 10.1016/j.apt.2013.01.016.

[59] S. Homma, S. Ogata, J. Koga, and S. Matsumoto, "Gas–solid reaction model for a shrinking spherical particle with unreacted shrinking core," *Chem. Eng. Sci.*, vol. 60, no. 18, pp. 4971–4980, Sep. 2005, doi: 10.1016/j.ces.2005.03.057.

[60] F. Zhang, X. Wang, B. Wang, X. Lou, and W. Lipiński, "Experimental and numerical analysis of CO2 and CH4 hydrate formation kinetics in microparticles: A comparative study based on

shrinking core model," *Chem. Eng. J.*, vol. 446, p. 137247, Oct. 2022, doi: 10.1016/j.cej.2022.137247.

[61] X. Wang, G. Li, and R. K. Eckhoff, "Kinetics study of hydration reaction between aluminum powder and water based on an improved multi-stage shrinking core model," *Int. J. Hydrog. Energy*, vol. 46, no. 67, pp. 33635–33655, Sep. 2021, doi: 10.1016/j.ijhydene.2021.07.191.

[62] G. Vilardi, "Mathematical modelling of simultaneous nitrate and dissolved oxygen reduction by Cu-nZVI using a bi-component shrinking core model," *Powder Technol.*, vol. 343, pp. 613–618, Feb. 2019, doi: 10.1016/j.powtec.2018.11.082.

[63] A. Mgaidi, F. Jendoubi, D. Oulahna, M. El Maaoui, and J. A. Dodds, "Kinetics of the dissolution of sand into alkaline solutions: application of a modified shrinking core model," *Hydrometallurgy*, vol. 71, no. 3–4, pp. 435–446, 2004.

[64] Y. Haseli, "Analysis of Hydrodynamic Transport Phenomena in a Fluidized Bed for Thermochemical Hydrogen Production," University of Ontario Institute of Technology, Oshawa, Ontario, 2008. Accessed: Oct. 20, 2023. [Online]. Available: https://hdl.handle.net/10155/7

[65] V. N. Daggupati, G. F. Naterer, K. S. Gabriel, R. J. Gravelsins, and Z. L. Wang, "Solid particle decomposition and hydrolysis reaction kinetics in Cu–Cl thermochemical hydrogen production," *Int. J. Hydrog. Energy*, vol. 35, no. 10, pp. 4877–4882, May 2010, doi: 10.1016/j.ijhydene.2009.08.082.

[66] K. Pope, Z. L. Wang, and G. F. Naterer, "Measured Steam Conversion and Chemical Kinetics in a Hydrolysis Packed Bed Reactor for Hydrogen Production," *Energy Procedia*, vol. 29, pp. 496–502, 2012, doi: 10.1016/j.egypro.2012.09.058.

[67] Š. Olejárová, J. Ružbarský, and T. Krenický, "Sieve Analysis," in *Vibrations in the Production System*, in SpringerBriefs in Applied Sciences and Technology, Cham: Springer International Publishing, 2019, pp. 15–28. doi: 10.1007/978-3-030-01737-8_3.

[68] N. Sivakugan, A. Arulrajah, and M. W. Bo, *Laboratory testing of soils, rocks, and aggregates*. J. Ross Publishing, 2011.

[69] S. Lowell, J. E. Shields, M. A. Thomas, and M. Thommes, *Characterization of Porous Solids and Powders: Surface Area, Pore Size and Density*, vol. 16. in Particle Technology Series, vol. 16. Dordrecht: Springer Netherlands, 2004. doi: 10.1007/978-1-4020-2303-3.

[70] S. Lowell and J. E. Shields, *Powder surface area and porosity*, vol. 2. Springer Science & Business Media, 2013.

[71] "Nelson-Jameson Chloride Analyzer; 120/220 VAC, 50/60 Hz from Cole-Parmer Canada." Accessed: Oct. 30, 2023. [Online]. Available: https://www.coleparmer.ca/i/nelson-jameson-chloride-analyzer-120-220-vac-50-60-hz/0265620

[72] E. Scholz, *Karl Fischer Titration*. in Chemical Laboratory Practice. Berlin, Heidelberg: Springer Berlin Heidelberg, 1984. doi: 10.1007/978-3-642-69989-4.

[73] The Engineering ToolBox (2004). "Moist Air - Water Vapor and Saturation Pressure." Accessed: Oct. 30, 2023. [Online]. Available: https://www.engineeringtoolbox.com/water-vapor-saturation-pressure-air-d_689.html

[74] G. F. Harrington and J. Santiso, "Back-to-Basics tutorial: X-ray diffraction of thin films," *J. Electroceramics*, vol. 47, no. 4, pp. 141–163, Dec. 2021, doi: 10.1007/s10832-021-00263-6.

[75] S. Zarei-Shokat, M. Forouzandeh-Malati, F. Ansari, and R. Dinmohammadi, "Identification and Analytical Approaches," in *Physicochemical Aspects of Metal-Organic Frameworks: A New Class of Coordinative Materials*, A. Maleki and R. Taheri-Ledari, Eds., in Engineering Materials. , Cham: Springer International Publishing, 2023, pp. 155–179. doi: 10.1007/978-3-031-18675-2_11.

[76] A. Kelly and K. M. Knowles, *Crystallography and crystal defects*. John Wiley & Sons, 2020.

[77] J. M. Broders, K. Pope, K. A. Hawboldt, and G. F. Naterer, 'Hydrolysis phase equilibrium in various reactor configurations of the thermochemical Cu--Cl cycle', *Int. J. Hydrog. Energy*, vol. 49, pp. 633–646, 2024.

[78] C. Zamfirescu, I. Dincer, and G. F. Naterer, "Thermophysical properties of copper compounds in copper–chlorine thermochemical water splitting cycles," *Int. J. Hydrog. Energy*, vol. 35, no. 10, pp. 4839–4852, May 2010, doi: 10.1016/j.ijhydene.2009.08.101.

Appendices

A.1 Measurement Errors and Experimental Uncertainties

This appendix explains the uncertainty and errors inherent in the experimental results. This comprehensive analysis entails evaluating factors such as device accuracy, bias, precision errors, and how uncertainties propagate through the experimental outcomes and calculations. The quantification of experimental uncertainty (U) entails the determination of bias (B) and precision errors (P) in Equation (A-1). Table A-1 lists all the measuring devices and their accuracy. The bias was determined using a reference value for each measurement and precision error was determined by doubling the standard deviation of 40 measurements. According to the results presented in this thesis, the computed value of the chemical reaction rate constant (k") was included in the uncertainty analysis as the reaction was considered to be reaction controlled with a cylindrical shape assumption. The k" constant was the constant that can be generated from the reaction rate expression presented in Equation (4-19). Accordingly, the propagation equation of Kline and McClintock was used to generate the mathematical expressions presented in Equations from (A-2) to (A-9), where the bias and precision error of computed variables are listed in Table A-2.

$$U_i = \sqrt{B_i^2 + P_i^2} \tag{A-1}$$

The Equations (A-2) and (A-3) provides the bias and precision error for the moles of inlet steam and the partial derivative for temperature, humidity and volumetric flow rate.

$$(B_{N_{\mathrm{H2O}}})^2 = \left(\frac{\partial N_{\mathrm{H2O}}}{\partial \mathrm{RH}} B_{\mathrm{RH}}\right)^2 + \left(\frac{\partial N_{\mathrm{H2O}}}{\partial \dot{V}} B_{\dot{V}}\right)^2 + \left(\frac{\partial N_{\mathrm{H2O}}}{\partial T_{\mathrm{h}}} B_{T_h}\right)^2 \tag{A-2}$$

$$(P_{N_{\mathrm{H2O}}})^2 = \left(\frac{\partial N_{\mathrm{H2O}}}{\partial \mathrm{RH}} P_{\mathrm{RH}}\right)^2 + \left(\frac{\partial N_{\mathrm{H2O}}}{\partial \dot{V}} P_{\dot{V}}\right)^2 + \left(\frac{\partial N_{\mathrm{H2O}}}{\partial T_{\mathrm{h}}} P_{T_h}\right)^2 \tag{A-3}$$

The Equations (A-4) and (A-5) provide the bias and precision error for the moles of the produced HCl, and Equations (A-6) and (A-7) present the conversion error. The calculated conversion uncertainty derived from these equations was determined to be ±6.6%.

$$(B_{N_{\mathrm{HCl}}})^2 = \left(\frac{\partial N_{\mathrm{HCl}}}{\partial C_{Cl}} B_{C_{Cl}}\right)^2 + \left(\frac{\partial N_{\mathrm{HCl}}}{\partial V_m} B_{V_m}\right)^2 \quad \text{(A-4)}$$

$$(P_{N_{\mathrm{HCl}}})^2 = \left(\frac{\partial N_{\mathrm{HCl}}}{\partial C_{Cl}} P_{C_{Cl}}\right)^2 + \left(\frac{\partial N_{\mathrm{HCl}}}{\partial V_m} P_{V_m}\right)^2 \quad \text{(A-5)}$$

$$(B_X)^2 = \left(\frac{\partial \mathrm{X}}{\partial N_{\mathrm{HCl}}} B_{N_{HCl}}\right)^2 + \left(\frac{\partial \mathrm{X}}{\partial m} B_{\mathrm{m}}\right)^2 \quad \text{(A-6)}$$

$$(P_X)^2 = \left(\frac{\partial \mathrm{X}}{\partial N_{\mathrm{HCl}}} P_{N_{HCl}}\right)^2 + \left(\frac{\partial \mathrm{X}}{\partial m} P_{\mathrm{m}}\right)^2 \quad \text{(A-7)}$$

Finally, the reaction constant bias and precision error are presented in Equations (A-8) and (A-9). where the propagation uncertainty was determined to be ±10%.

$$(B_{\mathrm{k''}})^2 = \left(\frac{\partial \mathrm{k''}}{\partial \mathrm{X}} B_{\mathrm{X}}\right)^2 + \left(\frac{\partial \mathrm{k''}}{\partial t} B_{\mathrm{t}}\right)^2 \quad \text{(A-8)}$$

$$(P_{\mathrm{k''}})^2 = \left(\frac{\partial \mathrm{k''}}{\partial \mathrm{X}} P_{\mathrm{X}}\right)^2 + \left(\frac{\partial \mathrm{k''}}{\partial t} P_{\mathrm{t}}\right)^2 \quad \text{(A-9)}$$

Table A-1: Measurement Devices Accuracy and Relative Error

Variable	Measurement Device	Device Range	Accuracy	Reference Value	Relative Bias Error	Relative Precision Error
t (min)	Stop Watch	-	±0.0005	1	0.0005	-
C_{Cl} (mg/l)	Sherwood Model 926 Chloride Analyser	11-999	±3	999	0.003	0.0051
$\dot{V}$ (SLPM)	Omega FMA-A2000 Gas Mass Flow Meters And Controllers	0-10	±0.01	3	0.003	0.0022
RH (%)	Omega HX200 Dew Point/Humidity Transmitters	0 to 95% RH	±1.0	95	0.01	0.0030
T_h (°C)		Max 200°C	±1	150	0.0067	0.0098
m_{CuCl2} (g)	Sartorius Balance	220 g	±0.01	5	0.002	-
P (bar)	Burkert 8311 Pressure Controller	0-2 bar	±0.015	0.5	0.030	0.0015

pH	Omega PHH-103B Portable pH/mV Temperature Meter	0 to 14	±0.02	14	0.0014	-
T_R (°C)	Omega Type K Thermocouple	-200 - 1250	±2.2	400	0.0055	0.00088
$V_{m\,(}$µl)	Research plus Pipette	500	±2	500	0.004	-
$V_{s\,(}$ml)	2 mL Glass Pipettes	0.002	±2	2	0.001	-

Table A-2: Propagation of Experimental Uncertainty

Variable	Equation Numbers	Bias Error	Precision Error	Uncertainty
N_{H2O}	(A-2) - (A-6)	0.032	0.023	0.039
N_{HCl}	(A-7) - (A-9)	0.049	0.035	0.060
X	(A-10) - (A-13)	0.051	0.042	0.066
k"	(A-14) - (A-17)	0.082	0.051	0.097

The source of bias error of the measurements during the crystallisation experiment can be related to the instruments and their precision, as listed in Table A-3.

Table A-3: Crystallisation Experiment Precision Limit.

Tools	Precision Limit
Graduated Cylinders (100 mL)	± 0.5 mL
Thermometers	± 0.5 °C
Pipet (10 mL)	± 0.06 mL
Balance	± 0.005 g

A.2 Time Factor and Repeatability

Figure A-1 depicts the results of three experiments. Experiment 1, previously conducted for dried material at 390°C, is represented, along with Experiment 1a, a repetition of Experiment 1 under the same conditions to ensure experimental repeatability. Additionally, Experiment 1b represents a repetition of the conditions of Experiment 1, but for 45 minutes instead of 30 minutes. The conversion rate remains relatively consistent for this sample, whether 30 or 45 minutes. This was observed during the chemical analysis of the sample, where the concentration after 30 minutes exhibited fluctuations ranging within ±3 mg/l, which is within the margin of error of the device.

Similar repeatability tests were conducted for the crushed sample in Experiment 2, which achieved a higher conversion rate in 15 minutes. The same outcome was observed in the repeatability test in Experiment 2a, and the same conversion rate was achieved in the experiment conducted for 30 minutes in Experiment 2b, as presented in Figure A-2. Furthermore, a repeatability test for Experiment 3 (Figure A-3) was conducted to verify the experiment's results for crystallised material with a particle size of 230 µm.

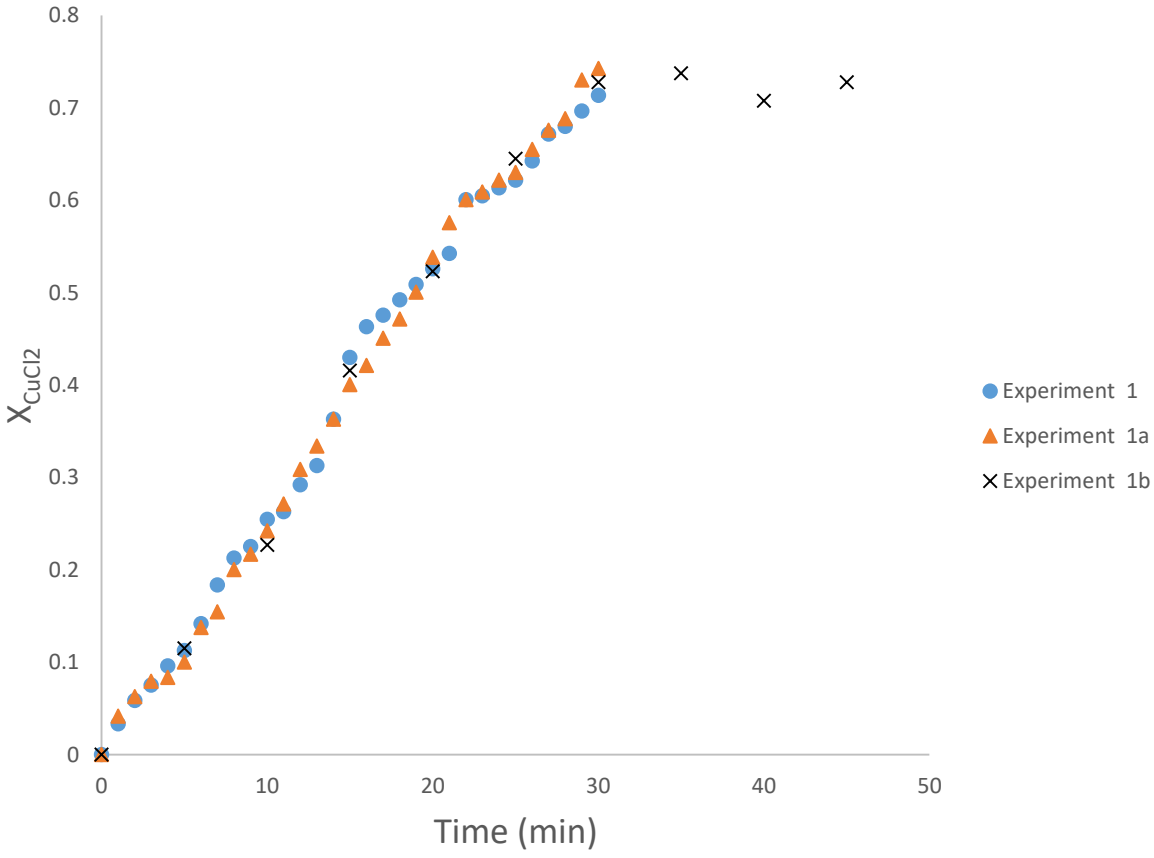

Figure A-1: Repeatability tests for dried $CuCl_2$ (Experiment 1) at 390°C and 95 µm particle size

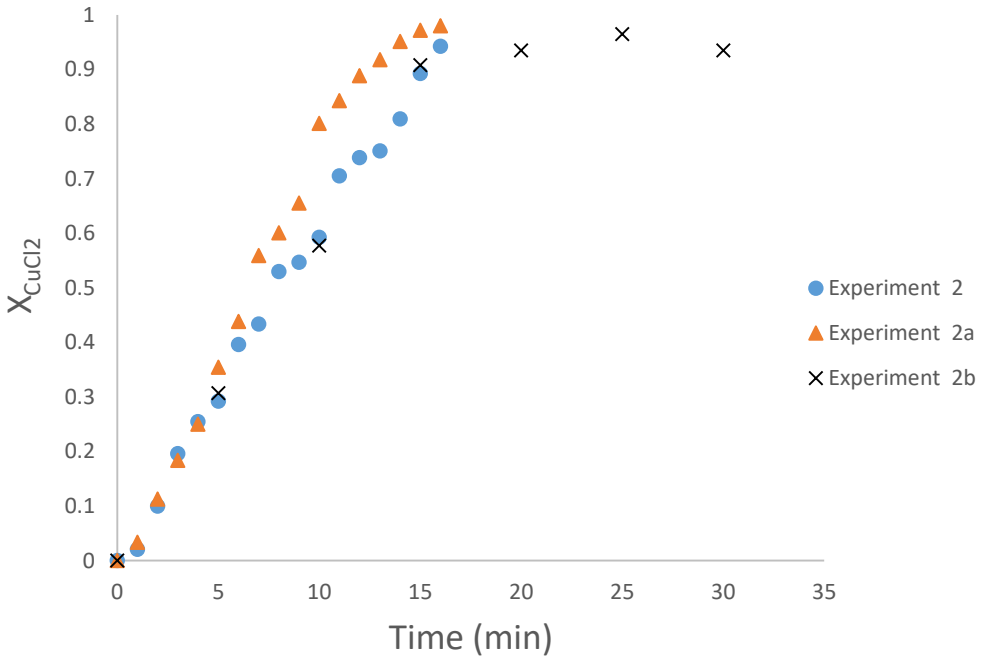

Figure A-2: Repeatability tests for crushed $CuCl_2$ (Experiment 2) at 390°C and 27 µm particle size

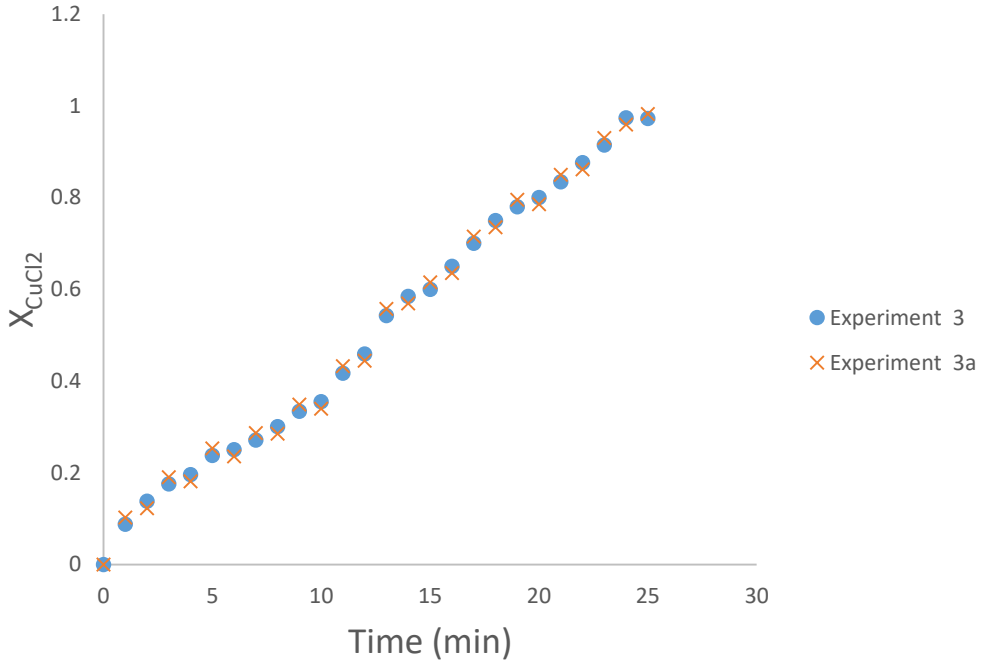

Figure A-3: Repeatability tests for crystallised $CuCl_2$ (Experiment 3) at 390°C and 230 µm particle size

A.3 Reactor Operating Parameters

Samples of the operational parameters acquired by the sensors are presented in Figure A-4.

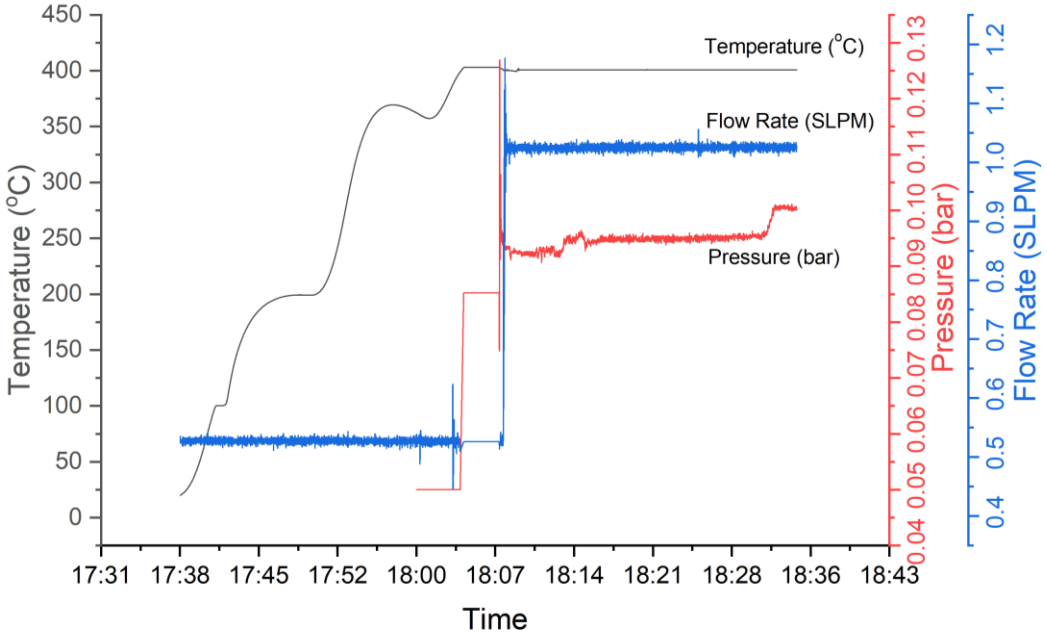

Figure A-4: Reactor Operating parameters

A.4 SCM Constants

All coefficients generated by the SCM for all experiments and model assumptions are recorded in Table A-4.

Table A-4: Gas Film Diffusion Constant, Product Layer Diffusion Coefficient And Reaction Constant

Exp. No.	Coefficients	Spherical Assumption		Cylindrical Assumption	
		Single resistance	Combined resistance	Single resistance	Combined resistance
1	k"	0.00074	0.00197	0.00106	0.00322
	De	1.173×10^{-09}	1.021×10^{-08}	2.570×10^{-09}	1.656×10^{-08}
	kg	0.00062	0.00173	0.00093	0.00283
2	k"	0.00046	0.00140	0.00065	0.00222
	De	8.757×10^{-11}	2.910×10^{-09}	1.946×10^{-10}	4.548×10^{-09}
	kg	0.00037	0.00113	0.00055	0.00181
3	k"	0.00275	0.00750	0.00385	0.01204
	De	2.161×10^{-08}	1.154×10^{-07}	4.571×10^{-08}	1.811×10^{-07}
	kg	0.00210	0.00626	0.00315	0.01011

Exp. No.	Coefficients	Spherical Assumption		Cylindrical Assumption	
		Single resistance	Combined resistance	Single resistance	Combined resistance
4	k"	0.00701	0.01905	0.00984	0.03039
	De	9.272×10^{-08}	8.848×10^{-07}	2.006×10^{-07}	1.386×10^{-06}
	kg	0.00541	0.01549	0.00811	0.02482
5	k"	0.01134	0.03033	0.01606	0.04898
	De	2.857×10^{-07}	2.174×10^{-06}	6.181×10^{-07}	3.463×10^{-06}
	kg	0.00903	0.02567	0.01355	0.04157
6	k"	0.00116	0.00307	0.00163	0.00491
	De	3.015×10^{-09}	2.118×10^{-08}	6.455×10^{-09}	3.332×10^{-08}
	kg	0.00088	0.00252	0.00133	0.00405
7	k"	0.00056	0.001625	0.00079	0.00257
	De	1.874×10^{-10}	3.446×10^{-09}	4.123×10^{-10}	5.334×10^{-09}
	kg	0.00044	0.00129	0.00066	0.00206
8	k"	0.00286	0.00776	0.00398	0.01222
	De	1.621×10^{-08}	1.431×10^{-07}	3.482×10^{-08}	2.195×10^{-07}
	kg	0.00213	0.00611	0.00321	0.00971
9	k"	0.00514	0.01546	0.00734	0.02449
	De	3.161×10^{-08}	7.394×10^{-07}	6.993×10^{-08}	1.144×10^{-06}
	kg	0.00422	0.01236	0.00634	0.01971
10	k"	0.01179	0.03234	0.01663	0.05159
	De	1.964×10^{-07}	2.711×10^{-06}	4.302×10^{-07}	4.256×10^{-06}
	kg	0.00923	0.02628	0.01385	0.04209
11	k"	0.00069	0.00187	0.00101	0.00306
	De	1.032×10^{-09}	9.397×10^{-09}	2.266×10^{-09}	1.518×10^{-08}
	kg	0.00059	0.00165	0.00089	0.00271
12	k"	0.00032	0.00112	0.00047	0.00179
	De	3.159×10^{-11}	2.179×10^{-09}	7.068×10^{-11}	3.449×10^{-09}
	kg	0.00028	0.00092	0.00042	0.00149
13	k"	0.00166	0.00462	0.00241	0.0075
	De	6.124×10^{-09}	6.088×10^{-08}	1.343×10^{-08}	9.709×10^{-08}
	kg	0.00142	0.00401	0.00213	0.00652
14	k"	0.00565	0.01534	0.00805	0.02478
	De	6.853×10^{-08}	6.033×10^{-07}	1.491×10^{-07}	9.594×10^{-07}
	kg	0.00461	0.01301	0.00691	0.02108
15	k"	0.00846	0.02274	0.01216	0.03704
	De	1.438×10^{-07}	1.394×10^{-06}	3.157×10^{-07}	2.243×10^{-06}
	kg	0.00715	0.01983	0.01073	0.03237
16	k"	0.00066	0.00179	0.00096	0.00293
	De	8.304×10^{-10}	8.568×10^{-09}	1.830×10^{-09}	1.390×10^{-08}
	kg	0.00057	0.00159	0.00086	0.00261

Exp. No.	Coefficients	Spherical Assumption		Cylindrical Assumption	
		Single resistance	Combined resistance	Single resistance	Combined resistance
17	k"	0.00046	0.00125	0.00066	0.0021
	De	2.289×10^{-10}	2.052×10^{-09}	4.995×10^{-10}	3.304×10^{-09}
	kg	0.00037	0.00108	0.00056	0.00176
18	k"	0.00029	0.00081	0.00044	0.00133
	De	1.953×10^{-10}	1.838×10^{-09}	4.351×10^{-10}	3.050×10^{-09}
	kg	0.00028	0.00076	0.00042	0.00126
19	k"	0.00107	0.00287	0.00157	0.00476
	De	2.920×10^{-09}	2.215×10^{-08}	6.456×10^{-09}	3.644×10^{-08}
	kg	0.00097	0.00267	0.00146	0.00442

A.5 SCM Models and Experimental Data

Figures A-5 to A-23 present a detailed comparison between the experimental data and the SCM models for both cylindrical and spherical assumptions for all the experiments.

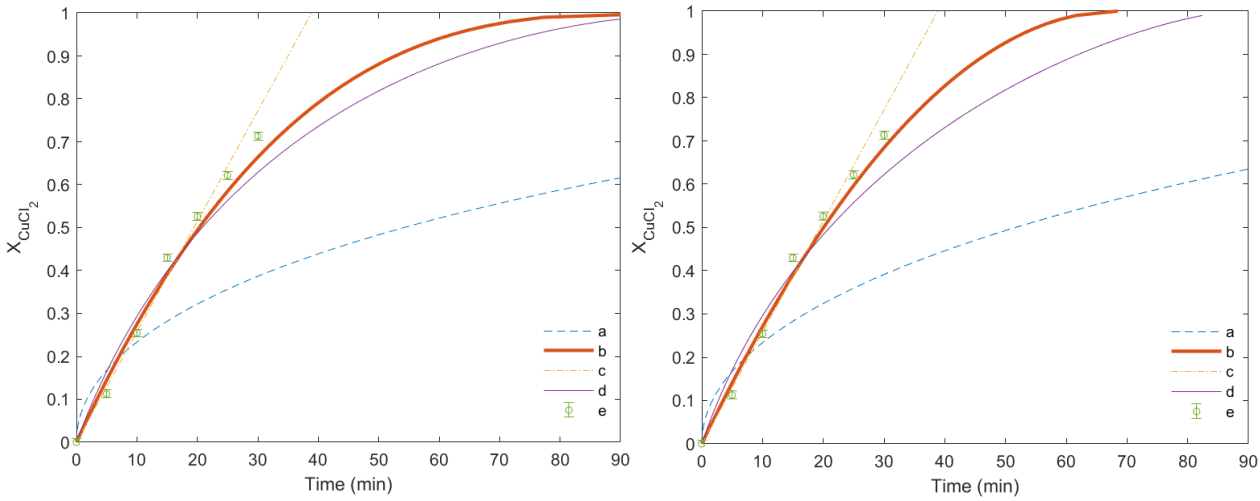

(i) (ii)

Figure A-5: Dried $CuCl_2$ conversion with time for Experiment 1 at 390°C and 95 µm particle size. (i) SCM with spherical particle shape assumption, (ii) SCM with cylindrical particle shape assumption. Controlling step comparison: (a) Product layer diffusion, (b) Reaction, (c) Gas film diffusion, (d) Combined control, and (e) Experimental data

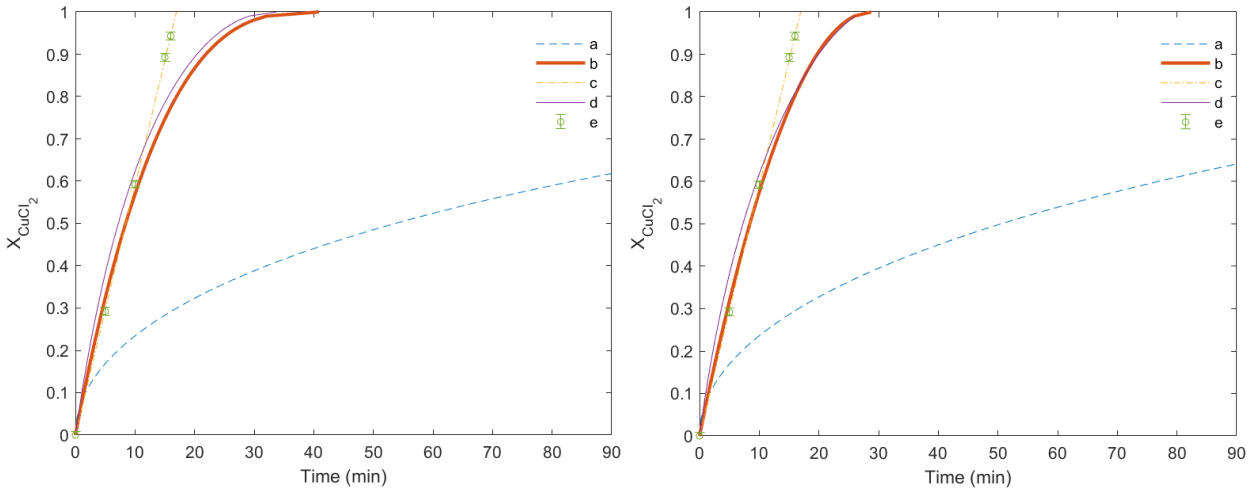

(i) (ii)

Figure A-6: Crushed $CuCl_2$ conversion with time for Experiment 2 at 390℃ and 27 µm particle size. (i) SCM with spherical particle shape assumption, (ii) SCM with cylindrical particle shape assumption. Controlling step comparison: (a) Product layer diffusion, (b) Reaction, (c) Gas film diffusion, (d) Combined control, and (e) Experimental data

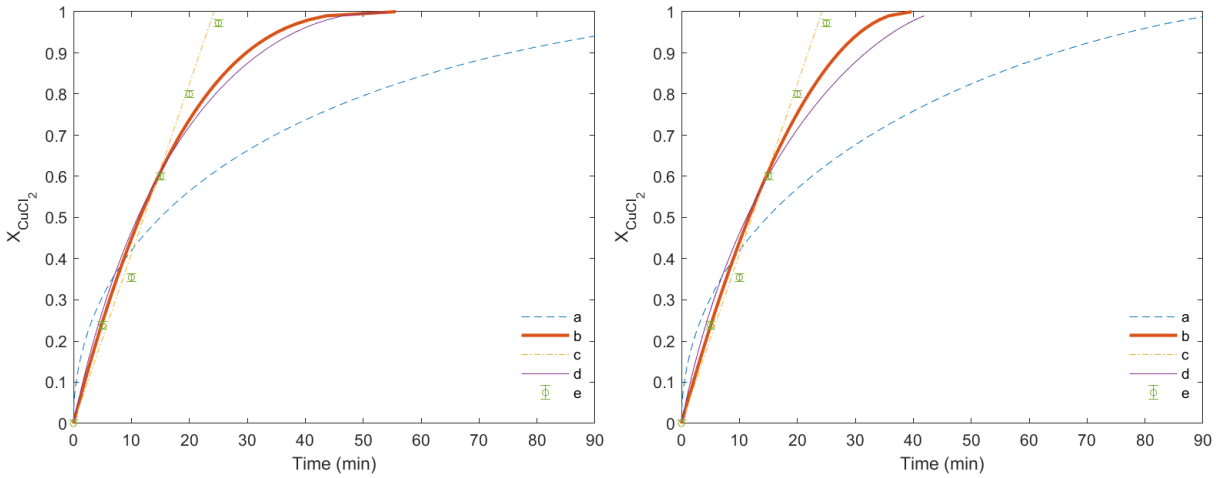

(i) (ii)

Figure A-7: Crystallised $CuCl_2$ conversion with time for Experiment 3 at 390℃ and 230 µm particle size. (i) SCM with spherical particle shape assumption, (ii) SCM with cylindrical particle shape assumption. Controlling step comparison: (a) Product layer diffusion, (b) Reaction, (c) Gas film diffusion, (d) Combined control, and (e) Experimental data

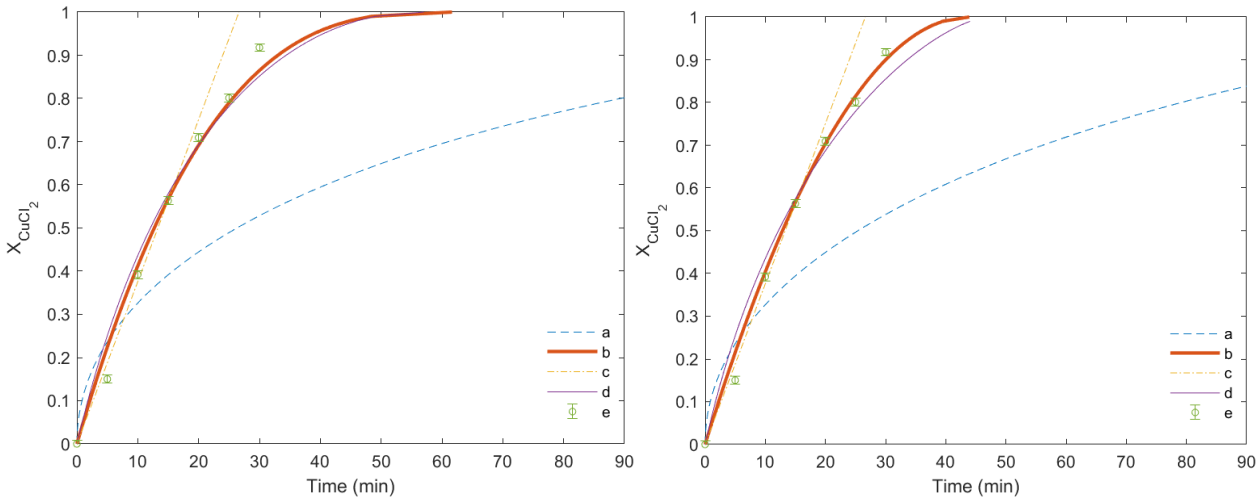

(i) (ii)

Figure A-8: Crystallised $CuCl_2$ conversion with time for Experiment 4 at 390°C and 615 µm particle size. (i) SCM with spherical particle shape assumption, (ii) SCM with cylindrical particle shape assumption. Controlling step comparison: (a) Product layer diffusion, (b) Reaction, (c) Gas film diffusion, (d) Combined control, and (e) Experimental data

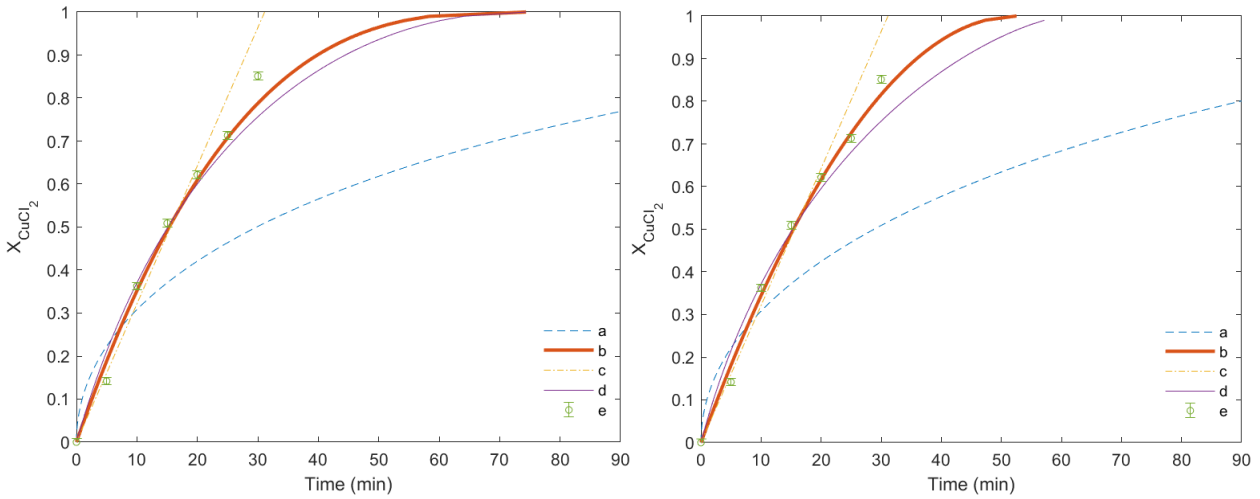

(i) (ii)

Figure A-9: Crystallised $CuCl_2$ conversion with time for Experiment 5 at 390°C and 1100 µm particle size, (i) SCM with spherical particle shape assumption, (ii) SCM with cylindrical particle shape assumption. Controlling step comparison: (a) Product layer diffusion, (b) Reaction, (c) Gas film diffusion, (d) Combined control, and (e) Experimental data

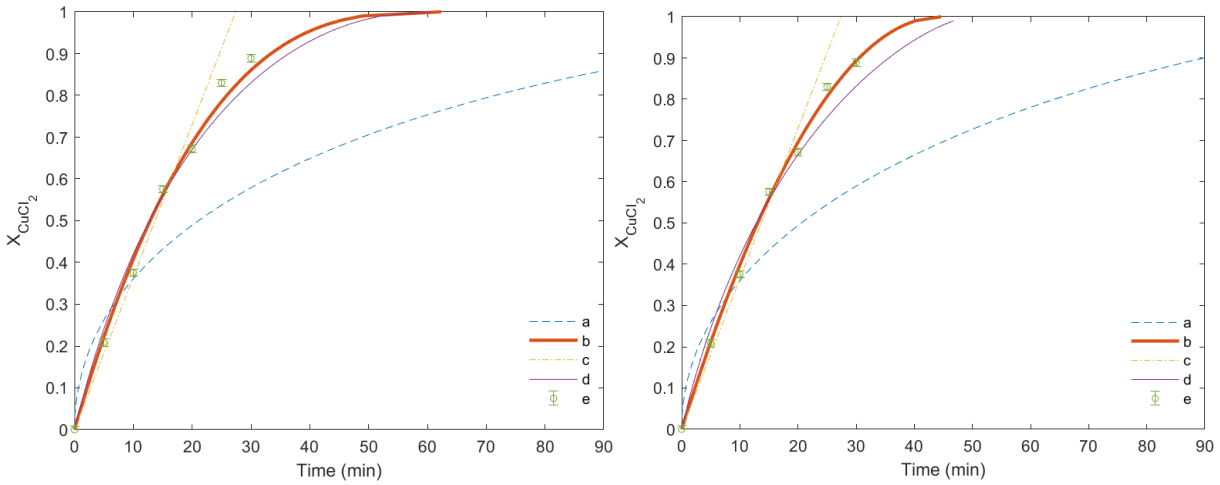

(i) (ii)

Figure A-10: Dried $CuCl_2$ conversion with time for Experiment 6 at 400°C and 95 µm particle size. (i) SCM with spherical particle shape assumption, (ii) SCM with cylindrical particle shape assumption. Controlling step comparison: (a) Product layer diffusion, (b) Reaction, (c) Gas film diffusion, (d) Combined control, and (e) Experimental data

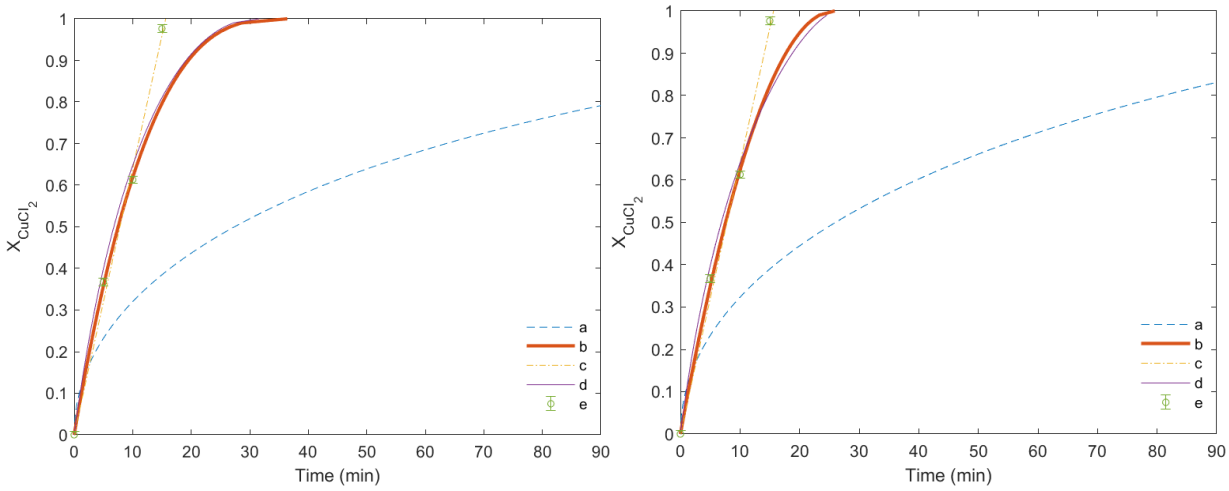

(i) (ii)

Figure A-11: Crushed $CuCl_2$ conversion with time for Experiment 7 at 400°C and 27 µm particle size, (i) SCM with spherical particle shape assumption, (ii) SCM with cylindrical particle shape assumption. Controlling step comparison: (a) Product layer diffusion, (b) Reaction, (c) Gas film diffusion, (d) Combined control, and (e) Experimental data

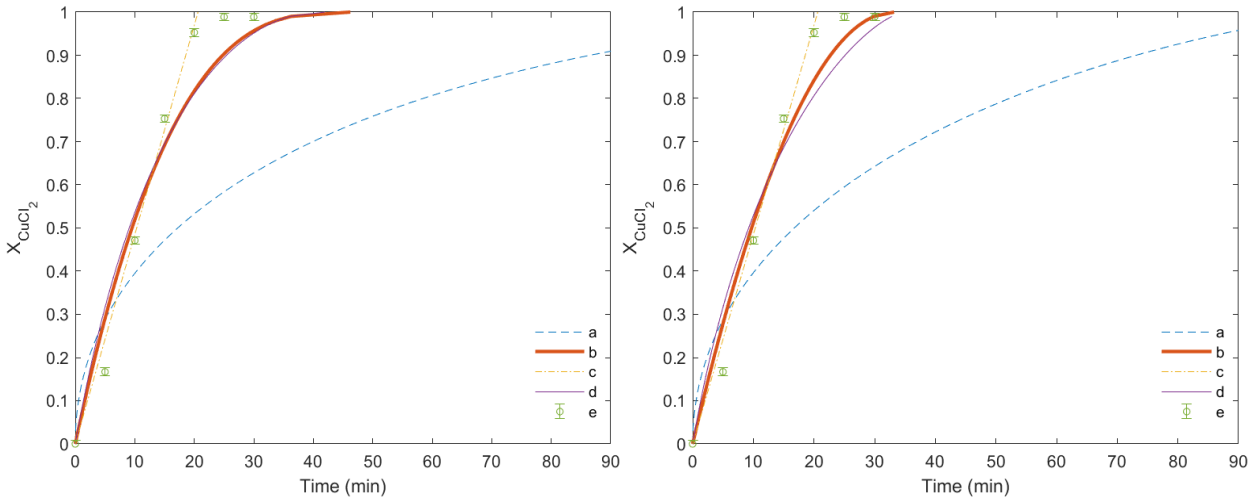

(i) (ii)

Figure A-12: Crystallised $CuCl_2$ conversion with time for Experiment 8 at 400℃ and 615 µm particle size. (i) SCM with spherical particle shape assumption, (ii) SCM with cylindrical particle shape assumption. Controlling step comparison: (a) Product layer diffusion, (b) Reaction, (c) Gas film diffusion, (d) Combined control, and (e) Experimental data

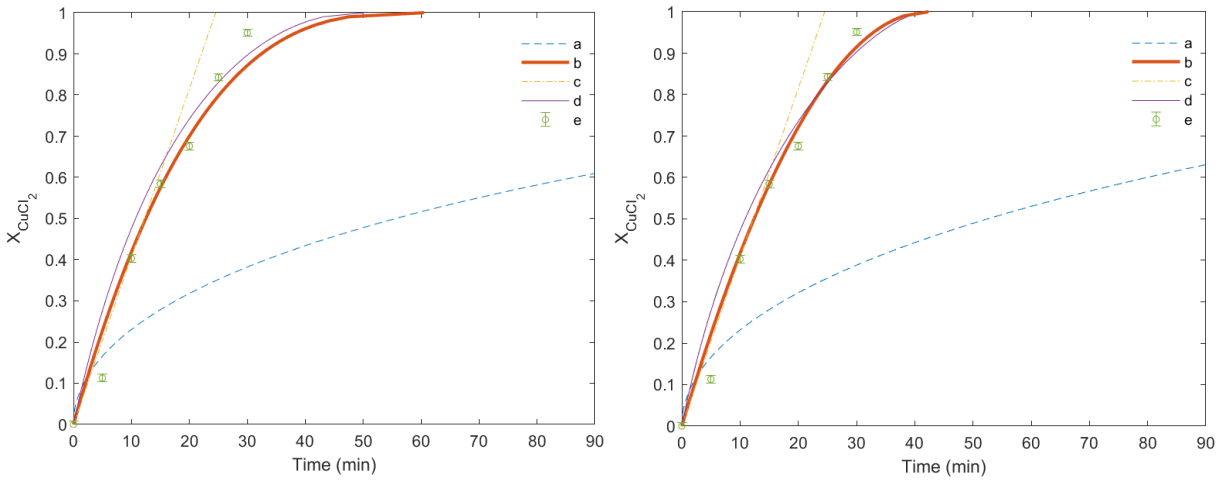

(i) (ii)

Figure A-13: Crystallised $CuCl_2$ conversion with time for Experiment 9 at 400℃ and 615 µm particle size, (i) SCM with spherical particle shape assumption, (ii) SCM with cylindrical particle shape assumption. Controlling step comparison: (a) Product layer diffusion, (b) Reaction, (c) Gas film diffusion, (d) Combined control, and (e) Experimental data

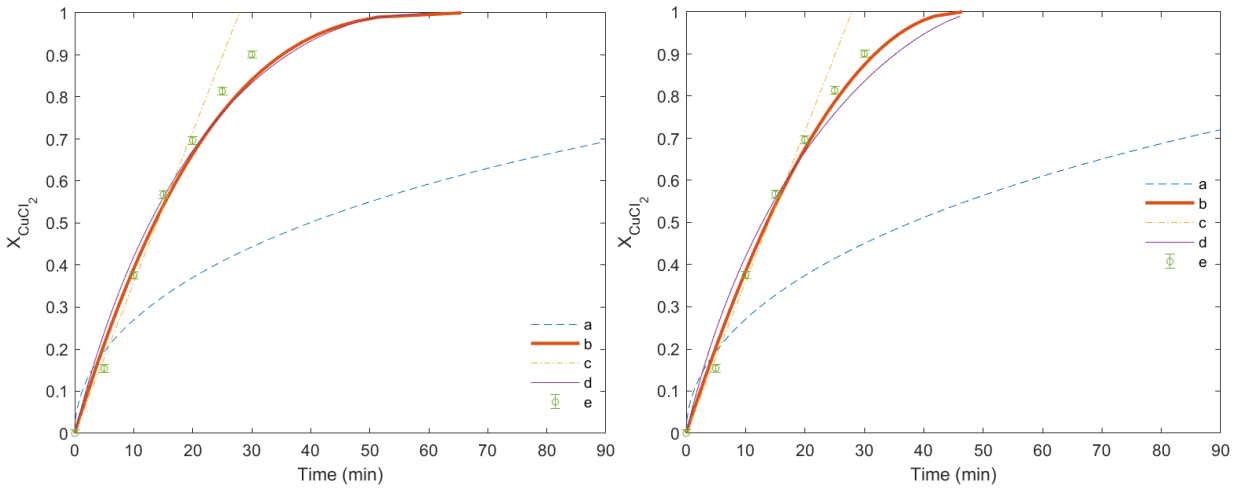

(i) (ii)

Figure A-14: Crystallised $CuCl_2$ conversion with time for Experiment 10 at 400°C and 1100 µm particle size, (i) SCM with spherical particle shape assumption, (ii) SCM with cylindrical particle shape assumption. Controlling step comparison: (a) Product layer diffusion, (b) Reaction, (c) Gas film diffusion, (d) Combined control, and (e) Experimental data

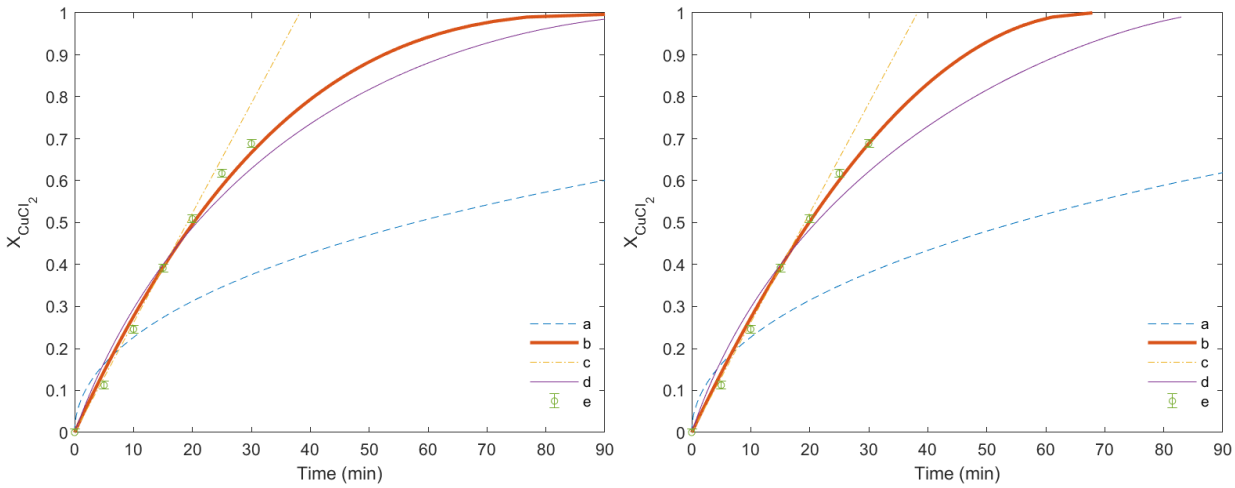

(i) (ii)

Figure A-15: Dried $CuCl_2$ conversion with time for Experiment 11 at 370°C and 95 µm particle size, (i) SCM with spherical particle shape assumption, (ii) SCM with cylindrical particle shape assumption. Controlling step comparison: (a) Product layer diffusion, (b) Reaction, (c) Gas film diffusion, (d) Combined control, and (e) Experimental data

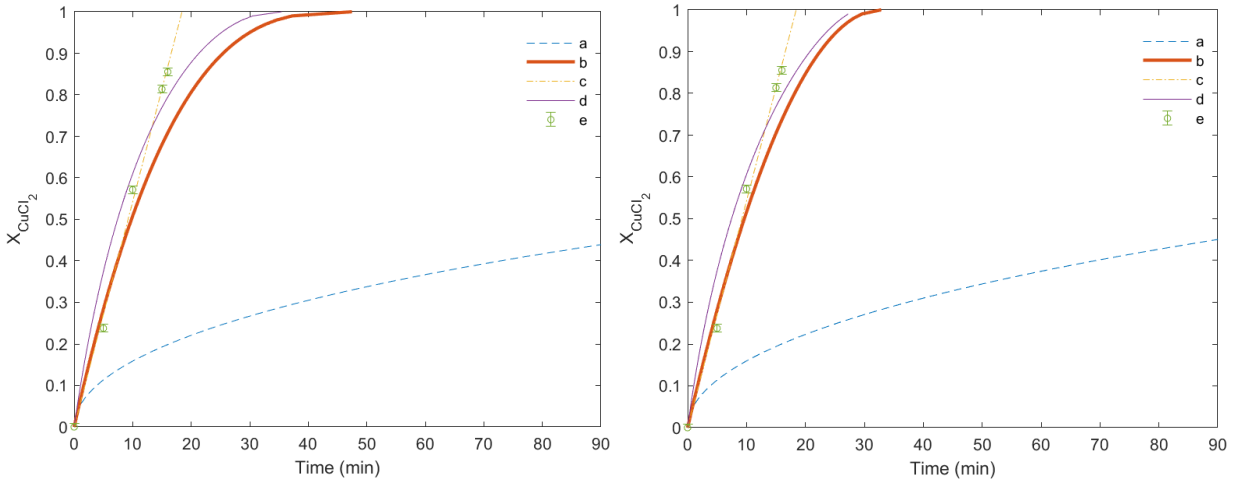

(i) (ii)

Figure A-16: Crushed $CuCl_2$ conversion with time for Experiment 12 at 370°C and 27 µm particle size, (i) SCM with spherical particle shape assumption, (ii) SCM with cylindrical particle shape assumption. Controlling step comparison: (a) Product layer diffusion, (b) Reaction, (c) Gas film diffusion, (d) Combined control, and (e) Experimental data

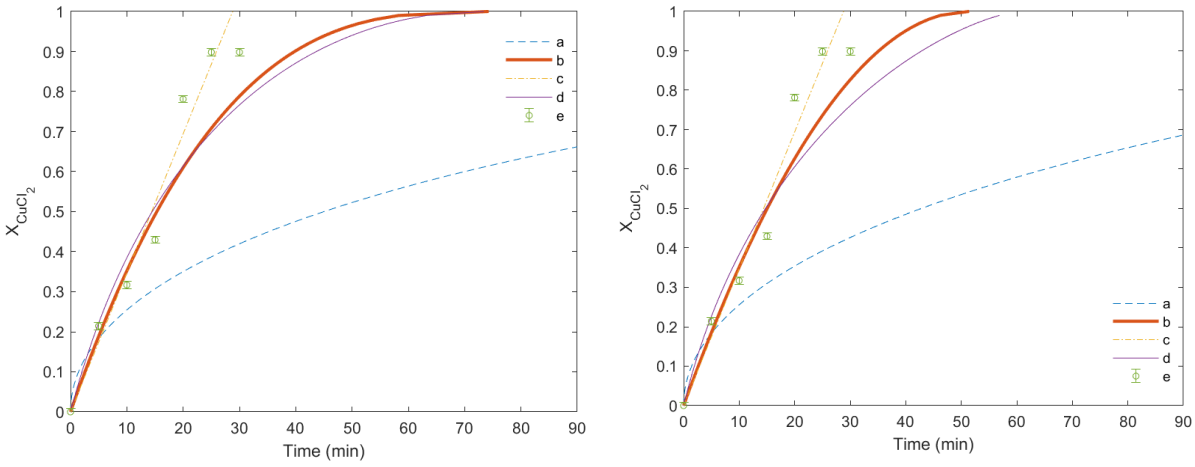

(i) (ii)

Figure A-17: Crystallised $CuCl_2$ conversion with time for Experiment 13 at 370°C and 615 µm particle size. (i) SCM with spherical particle shape assumption, (ii) SCM with cylindrical particle shape assumption. Controlling step comparison: (a) Product layer diffusion, (b) Reaction, (c) Gas film diffusion, (d) Combined control, and (e) Experimental data

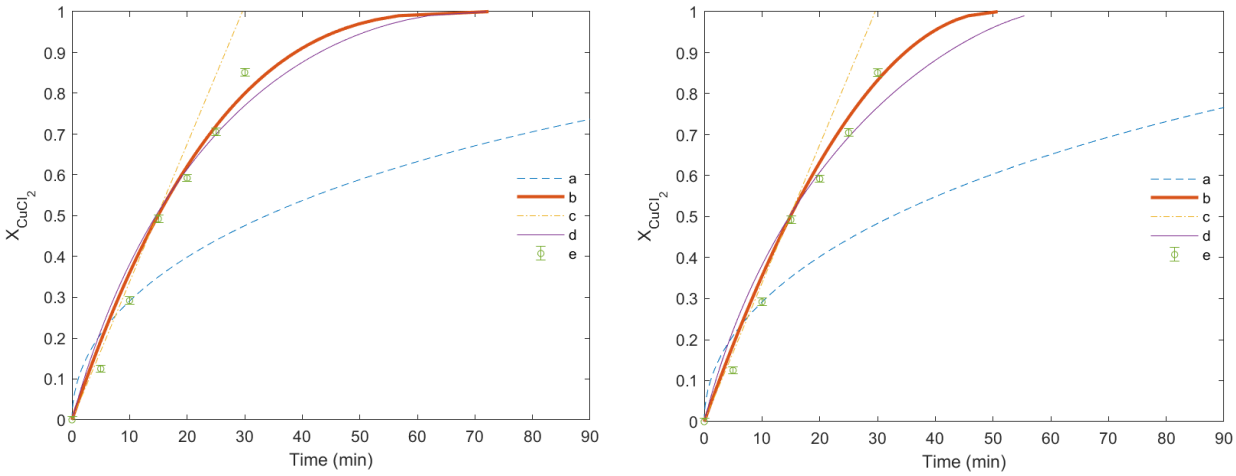

(i) (ii)

Figure A-18: Crystallised $CuCl_2$ conversion with time for Experiment 14 at 370°C and 615 µm particle size, (i) SCM with spherical particle shape assumption, (ii) SCM with cylindrical particle shape assumption. Controlling step comparison: (a) Product layer diffusion, (b) Reaction, (c) Gas film diffusion, (d) Combined control, and (e) Experimental data

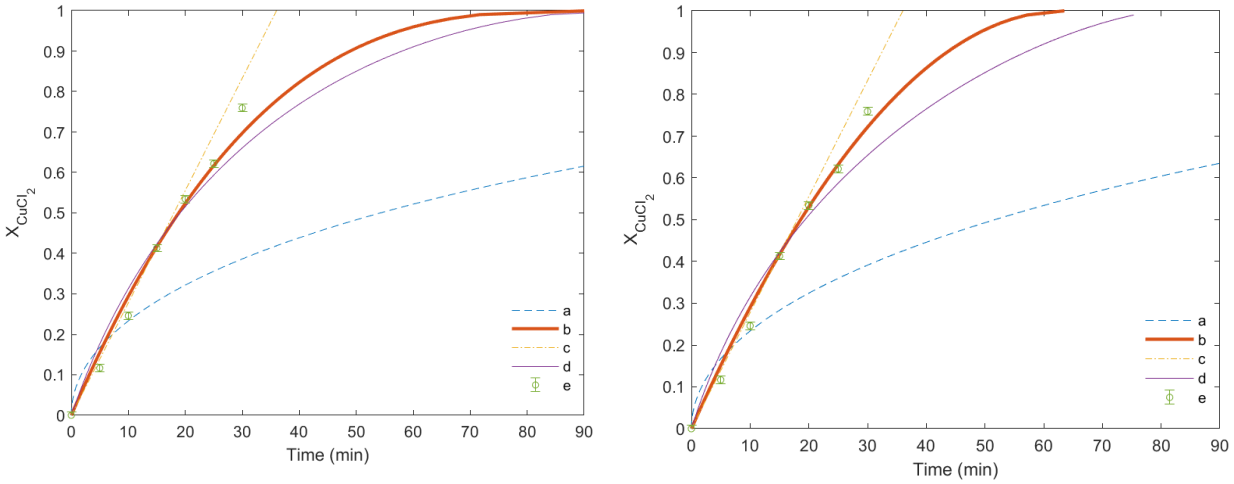

(i) (ii)

Figure A-19: Crystallised $CuCl_2$ conversion with time for Experiment 15 at 370°C and 1100 µm particle size. (i) SCM with spherical particle shape assumption, (ii) SCM with cylindrical particle shape assumption. Controlling step comparison: (a) Product layer diffusion, (b) Reaction, (c) Gas film diffusion, (d) Combined control, and (e) Experimental data

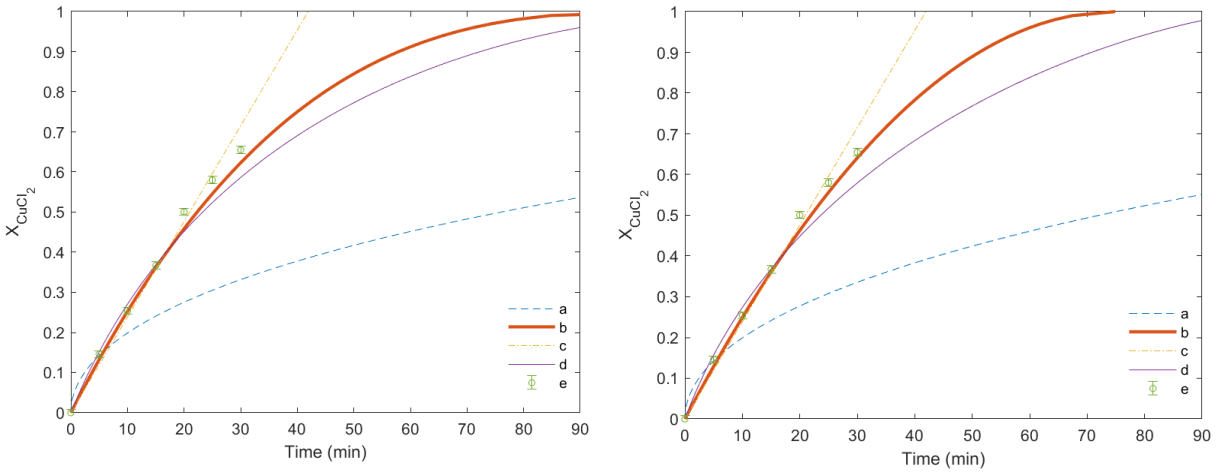

(i) (ii)

Figure A-20: Dried $CuCl_2$ conversion with time for Experiment 16 at 350°C and 95 µm particle size. (i) SCM with spherical particle shape assumption, (ii) SCM with cylindrical particle shape assumption. Controlling step comparison: (a) Product layer diffusion, (b) Reaction, (c) Gas film diffusion, (d) Combined control, and (e) Experimental data

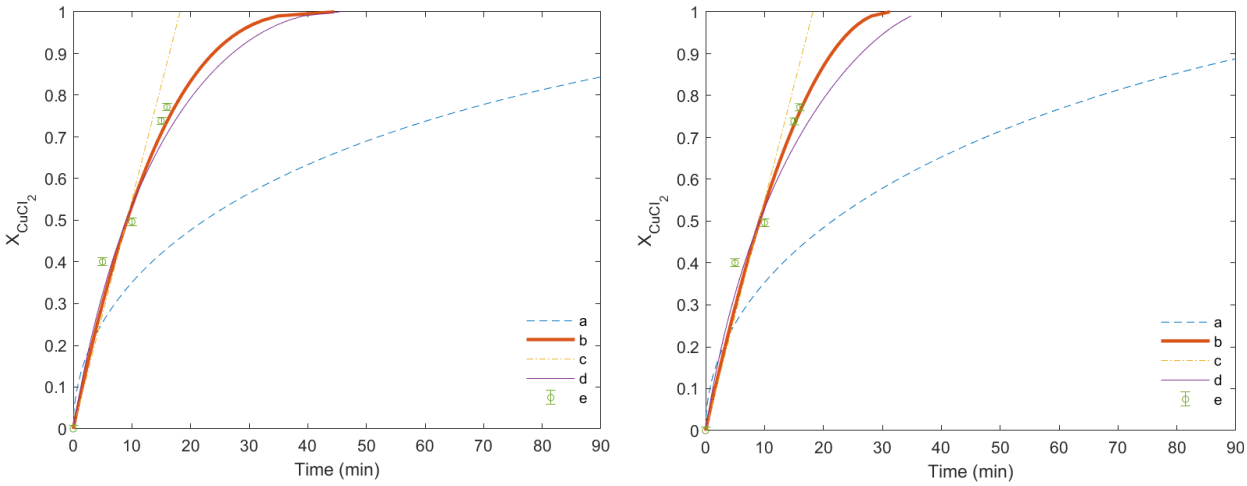

(i) (ii)

Figure A-21: Crushed $CuCl_2$ conversion with time for Experiment 17 at 350°C and 27 µm particle size. (i) SCM with spherical particle shape assumption, (ii) SCM with cylindrical particle shape assumption. Controlling step comparison: (a) Product layer diffusion, (b) Reaction, (c) Gas film diffusion, (d) Combined control, and (e) Experimental data

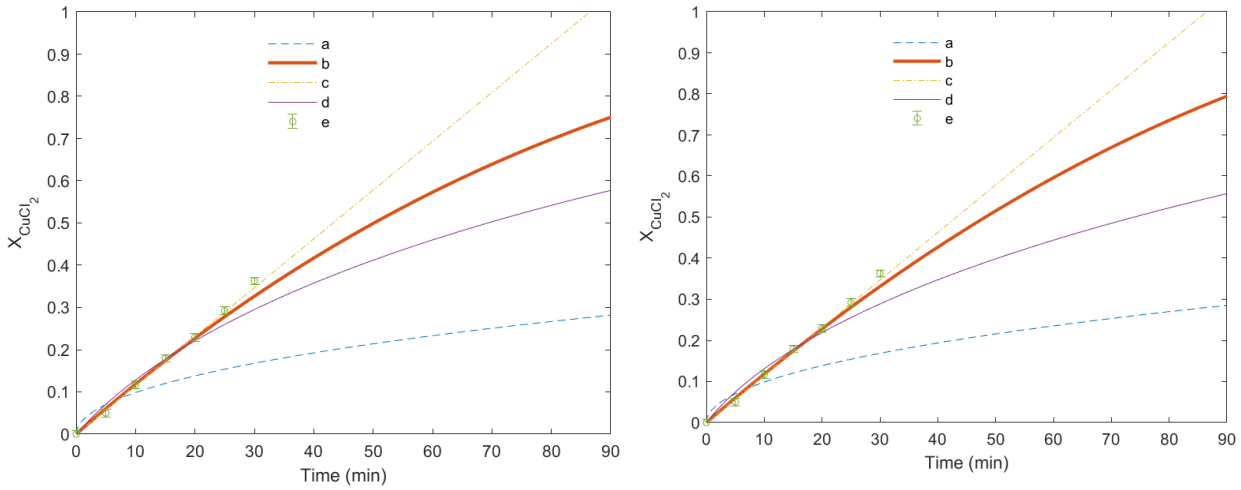

Figure A-22: Dried $CuCl_2$ conversion with time for Experiment 18 at 390°C and 95 µm particle size, S/Cu= 5, (i) SCM with spherical particle shape assumption, (ii) SCM with cylindrical particle shape assumption. Controlling step comparison: (a) Product layer diffusion, (b) Reaction, (c) Gas film diffusion, (d) Combined control, and (e) Experimental data

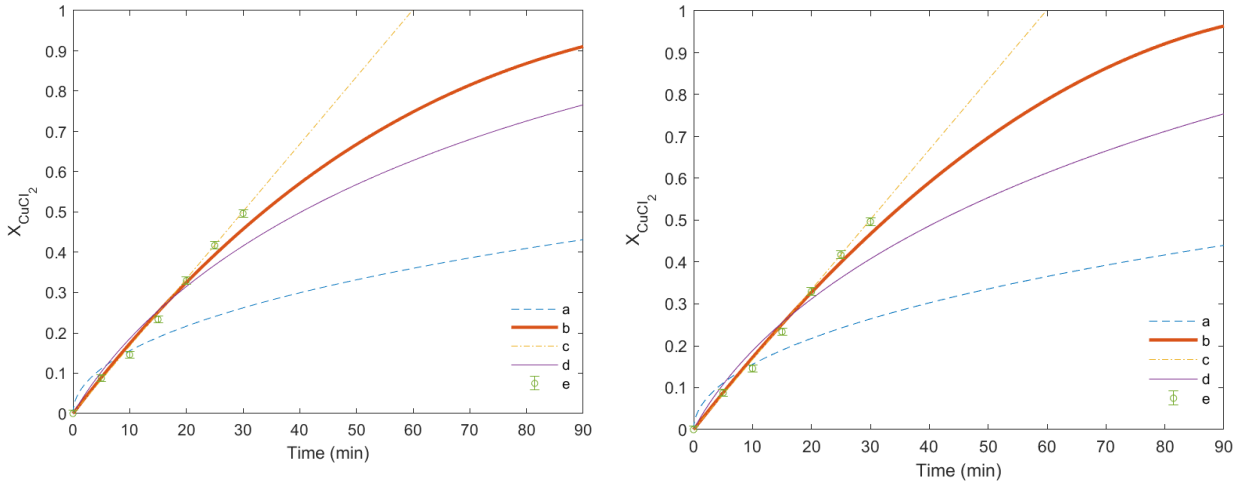

Figure A-23: Crystallised $CuCl_2$ conversion with time for Experiment 19 at 390°C and 230 µm particle size, S/Cu= 5, (i) SCM with spherical particle shape assumption, (ii) SCM with cylindrical particle shape assumption. Controlling step comparison: (a) Product layer diffusion, (b) Reaction, (c) Gas film diffusion, (d) Combined control, and (e) Experimental data

A.6 HSC Chemistry for Phase Equilibrium Simulations

The HSC Chemistry software, referenced in Section 5.2, was utilized to investigate the equilibrium of the hydrolysis reaction. Phase equilibrium simulations are instrumental in comprehending the behaviour of chemical systems. The Equilibrium Modules of HSC Chemistry employ the Gibbs energy minimization method, a fundamental thermodynamic principle, to predict phase compositions within a system. This method provides valuable insights into the equilibrium state of a system under varying conditions, enabling predictive analysis of phase equilibrium.

The Gibbs energy minimization method aims to minimize the Gibbs free energy to determine the equilibrium composition of phases in a system. Considering specified temperature and pressure conditions, this approach calculates the composition of various phases, such as solid, liquid, and gas, while ensuring material balance. Notably, the method operates under isothermal and isobaric conditions to simulate equilibrium. All reactants, potential products, and by-product components were selected from the HSC Chemistry database. However, the main component, Cu_2OCl_2, was entered as user-defined, utilizing thermophysical properties from Zamfirescu et al. [78] to define the component. A pressure of 0.1 bar was employed to match the experimental conditions, and the molar quantity of the reactant was specified to align with the experiment.

The equilibrium yields of the hydrolysis reaction for the reactant and potential products are presented in Figure 5-18. While the Gibbs energy minimization method is powerful for phase equilibrium predictions, it assumes a closed system with an infinite reaction time and does not encompass chemical reaction rates. Consequently, the predicted products may not align with the experimental results, which may require more time. However, in this study, the analysis information was utilized to aid in identifying the XRD peaks associated with the expected products or by-products.